Circuits and Systems
Mekelweg 4,
2628 CD Delft
The Netherlands
https://sps.ewi.tudelft.nl/

SPS-2026-00

M.Sc. Thesis

Underdetermined Gridless DoA Estimation for Uniform Circular AVS Arrays via Co-Array Manifold Transformation

Begum Bilir

Abstract

Direction-of-arrival (DoA) estimation is a fundamental problem in array signal processing. In this work, we consider a uniform circular acoustic vector sensor (AVS) array and investigate underdetermined gridless DoA estimation scenarios, where the number of sources exceeds the number of physical sensors. We first characterize the co-array structure induced by the second-order statistics of the measurements and show that it can be interpreted as a concentric multi-circular array with increased degrees of freedom, whose virtual elements exhibit both pressure-like and AVS characteristics. This expanded co-array enables the identification of more sources than the number of physical array elements. Next, we employ a co-array manifold transformation based on the Jacobi–Anger expansion to map the resulting concentric multi-circular structure onto a virtual uniform linear array (ULA). This transformation enables the application of high-resolution gridless subspace-based DoA estimation techniques, such as ESPRIT and Root-MUSIC. However, since the proposed framework operates in the correlation domain of stationary signals, only a single snapshot is available, which poses a challenge for conventional subspace methods that require multiple snapshots. To address this limitation, approaches including inverse modeling with spatial smoothing (IMSS), as well as gridless sparse recovery based on atomic norm minimization (ANM), are employed. The proposed framework is evaluated under three measurement configurations: pressure-only, particle velocity-only, and combined AVS observations.

Underdetermined Gridless DoA Estimation for Uniform Circular AVS Arrays via Co-Array Manifold Transformation

Thesis

submitted in partial fulfillment of the
requirements for the degree of

Master of Science

in

Electrical Engineering

by

Begum Bilir
born in Ankara, Turkey

This work was performed in:

Circuits and Systems Group
Department of Microelectronics
Faculty of Electrical Engineering, Mathematics and Computer Science
Delft University of Technology



Delft University of Technology

Copyright © 2026 Circuits and Systems Group
All rights reserved.

Delft University of Technology
Department of
Microelectronics

The undersigned hereby certify that they have read and recommend to the Faculty of Electrical Engineering, Mathematics and Computer Science for acceptance a thesis entitled **"Underdetermined Gridless DoA Estimation for Uniform Circular AVS Arrays via Co-Array Manifold Transformation"** by **Begum Bilir** in partial fulfillment of the requirements for the degree of **Master of Science**.

Dated: 28 May 2026

Chairman: _____

prof.dr.ir. Geert Leus

Advisor: _____

ir. David Pérez Cabo

Committee Member: _____

dr.ir. Yanki Aslan

Abstract

Direction-of-arrival (DoA) estimation is a fundamental problem in array signal processing. In this work, we consider a uniform circular acoustic vector sensor (AVS) array and investigate underdetermined gridless DoA estimation scenarios, where the number of sources exceeds the number of physical sensors. We first characterize the co-array structure induced by the second-order statistics of the measurements and show that it can be interpreted as a concentric multi-circular array with increased degrees of freedom, whose virtual elements exhibit both pressure-like and AVS characteristics. This expanded co-array enables the identification of more sources than the number of physical array elements. Next, we employ a co-array manifold transformation based on the Jacobi–Anger expansion to map the resulting concentric multi-circular structure onto a virtual uniform linear array (ULA). This transformation enables the application of high-resolution gridless subspace-based DoA estimation techniques, such as ESPRIT and Root-MUSIC. However, since the proposed framework operates in the correlation domain of stationary signals, only a single snapshot is available, which poses a challenge for conventional subspace methods that require multiple snapshots. To address this limitation, approaches including inverse modeling with spatial smoothing (IMSS), as well as gridless sparse recovery based on atomic norm minimization (ANM), are employed. The proposed framework is evaluated under three measurement configurations: pressure-only, particle velocity-only, and combined AVS observations.

Acknowledgments

In 2023, I was a bachelor's student in Turkey, searching for a summer research internship, sending emails to many professors across Europe. Geert Leus was one of them, and unlike many professors who did not reply, he responded within less than an hour. Although he kindly explained that it was not possible to take on summer students at that time, his quick and considerate response made a good impression on me. It showed me that while summer 2023 was not the right time, there would be a time when we would work together.

This turned out to be true two years later, when I started my thesis in the SPS group at Delft University of Technology at the end of 2025 under his supervision. I am deeply grateful for his guidance and for the countless meetings we had, often lasting more than an hour. His effort in explaining concepts on the board and the time he invested in thinking through problems together with me made me fully dedicate myself to this thesis project. So, a big thank you to Geert Leus.

Another big thank you goes to David, my company mentor. Without him, I would not have had the opportunity to work on such an interesting thesis topic, nor the motivation to spend days on a single simulation. His guidance during our meetings was always incredibly helpful.

I would also like to thank all my colleagues at Microflown AVISA for their valuable support throughout my thesis and for always being willing to provide feedback whenever I needed it.

Thomas Prins, a special thank you to you as well. You filled the void left by my parents not being in the Netherlands, and your kindness always cheered me up. I am very grateful that we met. To the Prins family, thank you for giving me joyful memories and for being "thuis" in the Netherlands.

Lastly, a huge thank you to my parents and my family in Turkey. Without them, I would not be writing these lines in Delft today. Their constant support, both emotional and financial, made me who I am and enabled me to complete my thesis at TU Delft. I could say so much more, but one sentence summarizes it all: I am so lucky to be your daughter.

My name is written on this thesis, but I did not do this alone. This achievement belongs to all of us.

Once again, thank you all.

Begum Bilir
Delft, The Netherlands
28 May 2026

Contents

Abstract **iv**

Acknowledgments **v**

1 Introduction **1**
1.1 Motivation . . . 1
1.2 Uniform Circular Arrays (UCAs) . . . 1
1.3 Manifold Transformation . . . 2
1.4 Co-Array Processing . . . 2
1.5 Characterization of Acoustic Sound Fields . . . 3
1.5.1 U-Probe . . . 3
1.5.2 PU-Probe . . . 5
1.6 Uniaxial AVS-Based Array Model . . . 6
1.6.1 Uniaxial U-Probe Array Model . . . 6
1.6.2 Uniaxial PU-Probe Array Model . . . 7
1.7 Outline . . . 8

2 Signal Model for UCA **10**
2.1 Geometry of the Uniform Circular Array . . . 10
2.2 Narrowband Signal Model . . . 11
2.3 Pressure Array Representation . . . 11
2.4 Uniaxial U-Probe Array . . . 13
2.5 Uniaxial PU-Probe Array . . . 14
2.6 Conclusion . . . 15

3 UCA Co-Array Structure **16**
3.1 Pressure Co-Array Structure . . . 16
3.1.1 Non-Redundant Co-Array Construction via Selection Matrix . . 17
3.1.2 Redundant Co-Array Construction for Averaging . . . 18
3.2 Uniaxial U-Probe Co-Array Structure . . . 18
3.2.1 Special Case: Co-Array Structure of Uniaxial U-probe with a Central Pressure Sensor . . . 23
3.3 Uniaxial PU-Probe Co-Array Structure . . . 25
3.4 Conclusion . . . 30

4 From the UCA Co-Array to a Virtual ULA **31**
4.1 Transformation of UCA Pressure Co-Array . . . 31
4.1.1 Transformation via Non-Redundant Co-Array Representation . 31
4.1.2 Transformation via Redundant Co-Array Representation . . . 33
4.2 Transformation of UCA Uniaxial U-Probe Co-Array . . . 34
4.2.1 Special Case: Transformation of UCA Uniaxial U-probe with a Central Pressure Sensor . . . 37

4.3 Transformation of UCA Uniaxial PU-Probe Co-Array 41
4.4 Conclusion 44

5 Exploiting the ULA Structure **46**
5.1 Inverse Modeling and Spatial Smoothing (IMSS) 46
5.2 Atomic Norm Minimization (ANM) 47
5.3 Gridless Subspace Methods 48
5.3.1 ESPRIT 49
5.3.2 Root-MUSIC 49
5.4 Conclusion 50

6 Simulation Results and Comparative Analysis **51**
6.1 Comparison for $K < M$ through MUSIC 52
6.1.1 MUSIC Spectrum Comparison 54
6.2 Single Realization Results 56
6.2.1 Pressure Sensor Setup 56
6.2.2 U-Probe Setup 57
6.2.3 PU-Probe Setup 58
6.3 RMSE Performance versus SNR 58
6.3.1 Pressure Co-Array Configuration 59
6.3.2 U-Probe Configuration 60
6.3.3 Special Case: U-Probe with a Central Pressure Sensor 62
6.3.4 PU-Probe Configuration 65
6.4 Conclusion 67

7 Conclusion **68**
7.1 Future Work 69

List of Figures

1.1 Microflown Regular Probes. 3
1.2 Configuration of a single U-probe and one sound source. 4

2.1 Measurement model of a UCA composed of pressure sensors (blue). The array consists of M sensors uniformly distributed on a circle of radius R. Multiple incident plane waves $k = 1, \cdots, K$ arrive from directions (φ_k, ϑ_k), producing pressure measurements at each sensor. 12
2.2 Measurement model of a UCA composed of U-probes (blue) that are arbitrarily oriented (red arrow). 13

3.1 Co-array sensor locations (blue) derived from physical UCA sensor positions (red), $M = 11$ and $R = 2.8\lambda$. 17
3.2 Co-array of virtual sensors (blue) with second-order directional pattern (black dashed line) derived from physical UCA sensor positions (red), $M = 11$ and $R = 2.8\lambda$ for tangential U-probe configuration. 21
3.3 Co-array of virtual sensors (blue) with second-order directional pattern (black dashed line) derived from physical UCA sensor positions (red), $M = 11$ and $R = 2.8\lambda$ for radial U-probe configuration. 21
3.4 Co-array of virtual sensors (blue) with second-order directional pattern (black dashed line) derived from physical UCA sensor positions (red), $M = 11$ and $R = 2.8\lambda$ for random U-probe configuration. 22
3.5 Co-array of virtual pressure sensors (blue), virtual sensors with second-order directional pattern (black dashed line) and virtual particle velocity sensors (red and yellow) derived from physical UCA with $M = 11$ and $R = 2.8\lambda$ for tangential U-probe configuration with a central pressure sensor. 24
3.6 Co-array of virtual pressure sensors (blue), virtual sensors with second-order directional pattern (black dashed line) and virtual particle velocity sensors (red and yellow) derived from physical UCA with $M = 11$ and $R = 2.8\lambda$ for radial U-probe configuration with a central pressure sensor. 25
3.7 Co-array of virtual pressure sensors (blue), virtual sensors with second-order directional pattern (black dashed line) and virtual particle velocity sensors (red and yellow) derived from physical UCA with $M = 11$ and $R = 2.8\lambda$ for random U-probe configuration with a central pressure sensor. 26
3.8 Co-array of virtual pressure sensors (blue), virtual sensors with second-order directional pattern (black dashed line) and virtual particle velocity sensors (cyan and green) derived from physical UCA sensor positions (red), $M = 11$ and $R = 2.8\lambda$ for tangential PU-probe configuration. . . 28
3.9 Co-array of virtual pressure sensors (blue), virtual sensors with second-order directional pattern (black dashed line) and virtual particle velocity sensors (cyan and green) derived from physical UCA sensor positions (red), $M = 11$ and $R = 2.8\lambda$ for radial PU-probe configuration. 29

3.10 Co-array of virtual pressure sensors (blue), virtual sensors with second-order directional pattern (black dashed line) and virtual particle velocity sensors (cyan and green) derived from physical UCA sensor positions (red), $M = 11$ and $R = 2.8\lambda$ for random PU-probe configuration. . . . 29

4.1 Magnitude of the $\mathbf{G}^{(\mathrm{p})}_{t,Q_\mathrm{p}}$, $t \in \{a, b\}$ coefficients as a function of harmonic order q for all unique sensor-pair differences in a UCA with $M = 11$ and $R = 2.8\lambda$. The absolute values depend only on ζ_{mn}, resulting in six distinct decay profiles. 33

4.2 Magnitude of the $\mathbf{G}^{(\mathrm{u})}_{Q_\mathrm{u}}$ coefficients as a function of harmonic order q for all unique tangential sensor-pair differences in a UCA with $M = 11$ and $R = 2.8\lambda$. The absolute values depend only on ζ_{mn}, resulting in six distinct decay profiles. 36

4.3 Magnitude of the $\mathbf{G}^{(\mathrm{u})}_{Q_\mathrm{u}}$ coefficients as a function of harmonic order q for all unique radial sensor-pair differences in a UCA with $M = 11$ and $R = 2.8\lambda$. The absolute values depend only on ζ_{mn}, resulting in six distinct decay profiles. 36

4.4 Magnitude of the $\mathbf{G}^{(\mathrm{u})}_{Q_\mathrm{u}}$ coefficients as a function of harmonic order q for all unique random sensor-pair differences in a UCA with $M = 11$ and $R = 2.8\lambda$. 37

4.5 Magnitude of the $\mathbf{G}^{(\mathrm{sp})}_{Q_\mathrm{u}}$ coefficients as a function of harmonic order q for all unique tangential sensor-pair differences in a UCA with $M = 11$ and $R = 2.8\lambda$, $Q_u^{(\mathrm{sp})} = 40$. The absolute values depend on ζ_{mn} and orders $q \pm 1$ and $q \pm 2$, resulting in eight distinct decay profiles. 40

4.6 Magnitude of the $\mathbf{G}^{(\mathrm{sp})}_{Q_\mathrm{u}}$ coefficients as a function of harmonic order q for all unique radial sensor-pair differences in a UCA with $M = 11$ and $R = 2.8\lambda$, $Q_u^{(\mathrm{sp})} = 40$. The absolute values depend on ζ_{mn} and orders $q \pm 1$ and $q \pm 2$, resulting in eight distinct decay profiles. 40

4.7 Magnitude of the $\mathbf{G}^{(\mathrm{sp})}_{Q_\mathrm{u}}$ coefficients as a function of harmonic order q for all unique random sensor-pair differences in a UCA with $M = 11$ and $R = 2.8\lambda$, $Q_u^{(\mathrm{sp})} = 40$. 41

4.8 Magnitude of the $\mathbf{G}^{(\mathrm{pu})}_{Q_\mathrm{pu}}$ coefficients as a function of harmonic order q for all unique tangential sensor-pair differences in a UCA with $M = 11$ and $R = 2.8\lambda$, $Q_\mathrm{pu} = 40$. The absolute values depend on ζ_{mn} and orders $q \pm 1$ and $q \pm 2$, resulting in 18 distinct decay profiles. 43

4.9 Magnitude of the $\mathbf{G}^{(\mathrm{pu})}_{Q_\mathrm{pu}}$ coefficients as a function of harmonic order q for all unique radial sensor-pair differences in a UCA with $M = 11$ and $R = 2.8\lambda$, $Q_\mathrm{pu} = 40$. The absolute values depend on ζ_{mn} and orders $q \pm 1$ and $q \pm 2$, resulting in 18 distinct decay profiles. 43

4.10 Magnitude of the $\mathbf{G}^{(\mathrm{pu})}_{Q_\mathrm{pu}}$ coefficients as a function of harmonic order q for all unique random sensor-pair differences in a UCA with $M = 11$ and $R = 2.8\lambda$, $Q_\mathrm{pu} = 40$. 44

6.1 RMSE comparison for the pressure case ($K = 3$), showing DoA estimation performance of MUSIC when applied after IMSS and ANM employed to the reconstructed virtual ULA with $Q_{\mathrm{p}} = 40$, and directly using the covariance matrix $\mathbf{R}_{xx}$ in a UCA 52
6.2 RMSE comparison for the U-probe case ($K = 3$), showing DoA estimation performance of MUSIC when applied after IMSS and ANM employed to the reconstructed virtual ULA with $Q_{\mathrm{u}} = 40$, and directly using the covariance matrix $\mathbf{R}_{xx}$ in a UCA. 53
6.3 RMSE comparison for the PU-probe case ($K = 3$ & $K = 6$), showing DoA estimation performance of MUSIC when applied after IMSS and ANM employed to the reconstructed virtual ULA with $Q_{\mathrm{pu}} = 40$, and directly using the covariance matrix $\mathbf{R}_{xx}$ in a UCA. 53
6.4 Comparison of MUSIC spectra using the covariance matrix $\mathbf{R}_{xx}$ (left) and the IMSS-based $\mathbf{R}_{\mathrm{ss}}$ (right) for $K = 3$, $Q_{\mathrm{p}} = 40$, SNR = 10 dB. . . 55
6.5 Comparison of MUSIC spectra using ANM-based $\mathbf{T}(\mathbf{u}^{(p)})$ (left) and $\hat{\mathbf{c}}_{Q_{\mathrm{p}}}$ (right) for $K = 3$, $Q_{\mathrm{p}} = 40$, SNR = 10 dB. 55
6.6 Comparison of true DoAs (dashed lines) and estimates obtained (crosses) via non-redundant pressure co-array using ESPRIT and Root-MUSIC methods for both IMSS and ANM approaches for $K = 16$ and 25, $Q_{\mathrm{p}} = 40$, SNR = 10 dB. 57
6.7 Comparison of true DoAs (dashed lines) and estimates obtained (crosses) via redundant pressure co-array using ESPRIT and Root-MUSIC methods for both IMSS and ANM approaches for $K = 16$ and 25, $Q_{\mathrm{p}} = 40$, SNR = 10 dB. 57
6.8 Comparison of true DoAs (dashed lines) and estimates obtained (crosses) on tangential U-probe configuration using ESPRIT and Root-MUSIC methods for both IMSS and ANM approaches for $K = 16$ and 25, $Q_{\mathrm{u}} = 40$, SNR = 10 dB. 58
6.9 Comparison of true DoAs (dashed lines) and estimates obtained (crosses) on tangential PU-probe configuration using ESPRIT and Root-MUSIC methods for both IMSS and ANM approaches for $K = 16$ and 25, $Q_{\mathrm{pu}} = 40$, SNR = 10 dB. 59
6.10 Comparison of non-redundant and redundant pressure co-array via RMSE versus SNR using ESPRIT and Root-MUSIC methods for both IMSS and ANM approaches for $K = 33$, $Q_{\mathrm{p}} = 40$, $\epsilon = 1$. 60
6.11 Comparison of U-probe orientations via RMSE versus SNR using ESPRIT and Root-MUSIC methods for both IMSS and ANM approaches for $K = 33$, $\epsilon = 1$. 60
6.12 Comparison of $Q_{\mathrm{u}} = 38$ and $Q_{\mathrm{u}} = 40$ via RMSE versus SNR using ESPRIT and Root-MUSIC methods for IMSS approach for $K = 33$. . . 61
6.13 Comparison of $\epsilon = 1$ and $\epsilon = 10$ via RMSE versus SNR using ESPRIT and Root-MUSIC methods for ANM approach for $K = 33$, $Q_{\mathrm{u}} = 40$. . . 62
6.14 Comparison of U-probe orientations with a central pressure sensor via RMSE versus SNR using ESPRIT and Root-MUSIC methods for both IMSS and ANM approaches for $K = 33$, $Q_{\mathrm{u}} = 40$, $\epsilon = 1$. 63

6.15 Comparison of ESPRIT and Root-MUSIC methods applied on U-probe orientations with a central pressure sensor via RMSE versus SNR for both IMSS and ANM approaches for $K = 33$, $Q_{\mathrm{u}} = 40$, $\epsilon = 1$. 63
6.16 RMSE versus SNR comparison using Root-MUSIC for both IMSS and ANM approaches for pressure-only (P), U-probe (U), and special U-probe (U(sp)) configurations with $K = 33$, $M = 11$, $L = 200$, $Q = 40$ and $R = 2.8\lambda$. 64
6.17 Comparison of PU-probe orientations via RMSE versus SNR using ESPRIT and Root-MUSIC methods for both IMSS and ANM approaches for $K = 33$, $\epsilon = 1$. 65
6.18 RMSE versus SNR comparison using Root-MUSIC for both IMSS and ANM approaches for pressure-only (P), U-probe (U), special U-probe (U(sp)), and PU-probe (PU) configurations with $K = 33$, $Q = 40$. . . . 66

List of Tables

6.1 RMSE performance comparison for pressure co-array constructions with ESPRIT and Root-MUSIC for IMSS and ANM for $K = 16$ and $K = 25$. 56
6.2 RMSE performance comparison for U-probe configurations using ESPRIT and Root-MUSIC with IMSS and ANM for $K = 16$ and $K = 25$. 58
6.3 RMSE performance comparison for PU-probe configurations using ESPRIT and Root-MUSIC with IMSS and ANM for $K = 16$ and $K = 25$. 59

1 Introduction

Microphone arrays are widely used in acoustic signal processing to analyze and interpret sound fields. By spatially distributing multiple sensors, these systems enable advanced processing techniques such as beamforming, source localization, and noise suppression. Compared to single microphones, arrays provide spatial diversity, allowing information about the direction and distribution of sound sources to be extracted [1].

1.1 Motivation

In many practical applications, acoustic sensing systems must operate under strict physical constraints. Devices such as hearing aids, wearable audio systems, mobile robots, and portable acoustic monitoring platforms require sensing solutions that are compact and lightweight [2, 3]. Similar requirements also arise in certain military and surveillance applications, where embedded sensing systems must be integrated into small platforms with limited space and power resources [4, 5].

These constraints limit both the physical size of the array and the number of sensors that can be deployed. While larger numbers of microphones can improve spatial resolution and lead to more accurate DoA estimation, they also increase system cost, complexity, and power consumption. As a result, practical systems often rely on arrays with a small aperture and a limited number of sensing elements.

This project addresses this challenge by exploiting the second-order statistics of array measurements to construct co-array representations that effectively enhance the array aperture and increase the number of virtual elements. Additionally, we consider acoustic vector sensors (AVSs) which provide particle velocity measurements, either alone or combined with pressure, allowing DoA estimation with fewer sensing elements and relaxed array aperture and spatial sampling requirements compared to microphone arrays [6, 7].

Building on this idea, an underdetermined gridless DoA estimation framework is developed for uniform circular arrays (UCAs) using AVSs. The key concepts underlying this approach, including UCAs, manifold transformation, co-array processing, and acoustic vector sensing, are introduced in the following sections.

1.2 Uniform Circular Arrays (UCAs)

The geometry of a microphone array plays a fundamental role in determining its spatial sensing capabilities. One commonly used configuration is the UCA, in which microphones are placed at equally spaced positions along the circumference of a circle. This arrangement provides a symmetric spatial distribution of sensors around a central point.

Compared to linear arrays, UCAs offer more uniform sensitivity to signals from all azimuth directions, whereas linear arrays are mainly sensitive along one axis [8, 9]. Their rotational symmetry eliminates the need for a preferred orientation. This property is particularly advantageous in autonomous systems where the direction of interest is generally unknown *a priori*. The circular layout also reduces directional ambiguities and improves the robustness of DoA estimation by enabling more balanced spatial sampling [10].

1.3 Manifold Transformation

Despite the advantages of UCAs, such as their rotational symmetry and uniform 360° spatial coverage, a key challenge in applying high-resolution DoA estimation techniques lies in the lack of shift invariance in their array manifold. Unlike uniform linear arrays (ULAs), whose steering vectors exhibit a Vandermonde structure that enables the direct use of gridless subspace methods, UCAs require additional processing to achieve a similar representation.

To address this, manifold transformation techniques have been developed, where the UCA steering vectors are mapped onto a virtual ULA domain [11, 12, 13, 14, 15, 16, 17, 18]. This transformation approximates a Vandermonde structure, enabling the application of well-established algorithms such as ESPRIT and Root-MUSIC.

Nevertheless, even with manifold transformation, practical UCAs remain limited by size and sensor count, which affect spatial resolution. Fewer sensors reduce the available spatial information, while a smaller aperture limits the ability to distinguish closely spaced sources. This results in broader beam patterns and lower DoA accuracy.

To address these challenges, a co-array sensing approach has been explored that provides increased spatial degrees of freedom while maintaining compact hardware configurations.

1.4 Co-Array Processing

Co-array theory enables the synthesis of a virtual sensor array from the second-order statistics of the received signals. By exploiting all pairwise sensor separations, the resulting difference co-array can substantially enlarge the effective aperture and increase the available degrees of freedom beyond those imposed by the physical geometry. This leads to improved angular resolution, enhanced source separability, even when the physical array is compact [19, 20, 21, 22, 23, 24, 25, 26, 27, 28]. While existing co-array frameworks primarily address linear and planar arrays with shift-invariance structures, a rigorous methodology for UCAs remains largely undeveloped, with only preliminary contributions to date [29, 30, 31, 32, 33].

This project further integrates co-array processing with AVSs, which measures the particle velocity of the sound field. By capturing the vector quantity of the acoustic field, these sensors can provide directional information thereby fundamentally enriching the measurement space and relaxing aperture and spatial sampling requirements [34].



(a) U-probe. (b) PU-probe.

Figure 1.1: Microflown Regular Probes.

1.5 Characterization of Acoustic Sound Fields

Acoustic sound fields describe how sound energy propagates through a medium such as air. The field is mainly described by acoustic pressure and particle velocity. Acoustic pressure is a scalar representing local pressure fluctuations, while particle velocity is a vector describing the motion of air particles [35].

Sound is typically measured with microphones, which convert pressure variations into electrical signals via a moving diaphragm. However, particle motion requires dedicated sensors, often based on thermal principles similar to hot-wire anemometers [36].

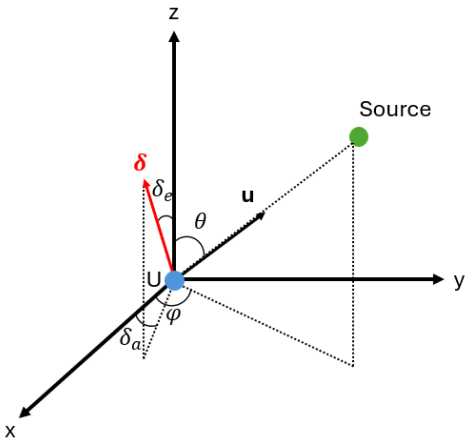
Using orthogonal sensing elements allows full measurement of the particle velocity vector. Combined with pressure, this enables a more complete sound field characterization and supports analyses such as sound intensity and source localization.

1.5.1 U-Probe

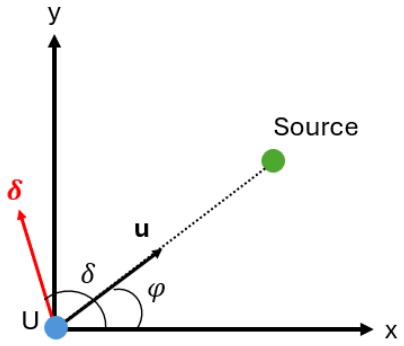
Although a full AVS measures acoustic pressure and multiple particle velocity components, a single particle velocity measurement can already provide useful spatial information [34]. Unlike microphones, which measure only scalar pressure, particle velocity sensors also capture directional information, offering additional insight into sound propagation.

The U Regular probe by Microflown integrates a single Microflown particle velocity sensor in a $\frac{1}{2}$-inch housing [37]. This sensor directly measures acoustic particle velocity through a physical mechanism, rather than estimating it from pressure, providing a complementary perspective to conventional sensors. Direct measurement of particle velocity allows sound intensity and related quantities to be derived without numerical approximations, improving accuracy and reliability. The probe is shown in Figure 1.1(a).

When a plane acoustic wave reaches the U-probe, the configuration can be represented using a 3D spherical coordinate system. In this system, the direction of the wave is described by the azimuth angle $\varphi \in [0, 2\pi)$ and the elevation angle $\vartheta \in [0, \pi]$, as depicted in Figure 1.2(a). Similarly, Figure 1.2(b) clearly defines the orientation of the U-probe and the direction of the incoming wave in 2D space. Here, uniaxial U-probe is considered, meaning that the probe is oriented arbitrarily.



(a) Configuration of a single U-probe and one sound source in $\mathbb{R}^3$.



(b) Configuration of a single U-probe and one sound source in $\mathbb{R}^2$.

Figure 1.2: Configuration of a single U-probe and one sound source.

The propagation direction of the acoustic source is described by the unit vector $\mathbf{u}$, written in spherical coordinates as

$$\mathbf{u} = \begin{bmatrix} \sin(\vartheta)\cos(\varphi) \\ \sin(\vartheta)\sin(\varphi) \\ \cos(\vartheta) \end{bmatrix}. \tag{1.1}$$

The orientation of the U-probe is represented by the unit vector $\boldsymbol{\delta}$,

$$\boldsymbol{\delta} = \begin{bmatrix} \sin(\delta_e)\cos(\delta_a) \\ \sin(\delta_e)\sin(\delta_a) \\ \cos(\delta_e) \end{bmatrix}.$$

which describes the direction in which the probe is aligned. The probe orientation is assumed to be freely adjustable, meaning the U-probe can be oriented in any direction depending on the measurement setup.

For obtaining the element–space measurement data, it is necessary to compute the projection of the source direction onto the U-probe. This projection is determined by the dot product between the source unit vector $\mathbf{u}$ and the probe orientation vector $\boldsymbol{\delta}$, which captures how much of the source signal aligns with the probe axis. It is given by

$$\begin{aligned} \boldsymbol{\delta}^T \cdot \mathbf{u} &= \sin(\delta_e)\cos(\delta_a)\sin(\vartheta)\cos(\varphi) + \sin(\delta_e)\sin(\delta_a)\sin(\vartheta)\sin(\varphi) + \cos(\delta_e)\cos(\vartheta) \\ &= \sin(\delta_e)\sin(\vartheta)\cos(\delta_a - \varphi) + \cos(\delta_e)\cos(\vartheta). \end{aligned}$$

Assuming a far-field, narrowband acoustic source, the Euler equation of motion establishes a linear relationship between the acoustic particle velocity $\mathbf{v}(\mathbf{r}, t)$ and the sound pressure $P(\mathbf{r}, t)$ at position $\mathbf{r}$ and time t [38]. In this case, the particle velocity is proportional to the pressure and can be expressed as

$$\mathbf{v}(\mathbf{r}, t) = -\frac{\mathbf{u}}{\rho c} P(\mathbf{r}, t),$$

where ρ denotes the density of the propagation medium and c is the speed of sound in that medium. The product ρc corresponds to the characteristic acoustic impedance of the medium and determines the proportionality between pressure and particle velocity.

The phase of the received wave at the sensor depends on the propagation delay relative to a chosen reference position. For a plane wave arriving from direction $\mathbf{u}$, this delay is represented by the exponential term $e^{j\kappa(\mathbf{r}\cdot\mathbf{u})}$, where $\mathbf{r}$ denotes the position vector of the sensor. The parameter $\kappa = \frac{2\pi}{\lambda}$ is the spatial frequency of the acoustic wave, commonly referred to as the wave number, with λ representing the wavelength.

As discussed earlier, the particle velocity and sound pressure differ only by a scaling factor determined by the characteristic acoustic impedance ρc. After compensating for this scaling factor, the element-space measurement of the U-probe at time instant t can be expressed as

$$y(t) = e^{j\kappa(\mathbf{r}\cdot\mathbf{u})} \left(\sin(\delta_e)\sin(\vartheta)\cos(\delta_a - \varphi) + \cos(\delta_e)\cos(\vartheta)\right) s(t) + n(t), \tag{1.2}$$

where $s(t)$ denotes the emitted source signal and $n(t)$ represents the measurement noise present at the sensor.

For the two–dimensional configuration, the elevation angles are set to $\pi/2$. Under this condition, both the source direction and the probe orientation lie in the horizontal plane, meaning the acoustic wavefront is confined to that plane. Consequently, the elevation angle no longer influences the geometry of the problem, and the system can be fully described using only the azimuth angles. Then (1.2) becomes

$$y(t) = e^{j\kappa(\mathbf{r}\cdot\mathbf{u})} \cos(\delta_a - \varphi) s(t) + n(t). \tag{1.3}$$

1.5.2 PU-Probe

While the U-probe provides directional information from a single particle velocity component, additional insight can be gained by also measuring acoustic pressure. Combining both enables characterization of the sound magnitude and energy propagation direction, motivating the use of a PU-probe.

A PU-probe combines a pressure microphone (P) with a Microflown particle velocity sensor (U) [39]. By measuring pressure and particle velocity at the same location, it provides more complete information about the acoustic field. This allows direct estimation of acoustic intensity, describing both energy flow and propagation direction, making PU-probes suitable for sound intensity measurements and source localization.

Because both quantities are measured at the same point, the PU-probe determines sound intensity without requiring spatially separated microphones or pressure gradient approximations. This co-located approach improves accuracy and reduces measurement errors. The probe is shown in Figure 1.1(b).

In the three–dimensional case, the PU-probe measurement vector can be written as

$$\mathbf{y}(t) = e^{j\kappa(\mathbf{r}\cdot\mathbf{u})} \begin{bmatrix} 1 \\ \sin(\delta_e)\sin(\vartheta)\cos(\delta_a - \varphi) + \cos(\delta_e)\cos(\vartheta) \end{bmatrix} s(t) + \mathbf{n}(t),$$

where the first element corresponds to the pressure measurement and the second element corresponds to the particle velocity component measured by the U-probe.

For the two–dimensional configuration, the elevation angles are fixed to $\pi/2$, which confines the propagation to the horizontal plane. Under this assumption, the expression simplifies and the PU-probe measurement vector becomes [40, 41]

$$\mathbf{y}(t) = e^{j\kappa(\mathbf{r}\cdot\mathbf{u})} \begin{bmatrix} 1 \\ \cos(\delta_a - \varphi) \end{bmatrix} s(t) + \mathbf{n}(t).$$

Here, $s(t)$ denotes the source signal and $\mathbf{n}(t)$ represents the measurement noise affecting the two sensor channels.

1.6 Uniaxial AVS-Based Array Model

We assume that all sensors are located on the same plane. Without loss of generality, we consider the sensors to lie on the xy-plane. We also assume that the elevation of the particle velocity orientation satisfies $\delta_e = \pi/2$, meaning that the particle velocity components are confined to the horizontal plane.

We consider a uniaxial AVS based array composed of M sensors located at arbitrary positions, described by the position vectors $\mathbf{r}_1, \mathbf{r}_2, \ldots, \mathbf{r}_M$. Assume that K far-field sound sources impinge on the array from directions specified by the unit vectors $\mathbf{u}_1, \mathbf{u}_2, \ldots, \mathbf{u}_K$ as shown in (1.1).

Each AVS sensor is either a U-probe consisting of a single particle velocity sensor or a PU-probe consisting of a pressure sensor and a single particle velocity sensor. The orientation of the particle velocity component of the m-th sensor is arbitrary and described by the azimuth angle δ_m. Collecting all sensor orientations yields the vector $\boldsymbol{\delta} = [\delta_1, \delta_2, \ldots, \delta_M]^T$.

1.6.1 Uniaxial U-Probe Array Model

The measurement vector of the U-probe array can be modeled as

$$\mathbf{y}(t) = \begin{bmatrix} \mathbf{a}_{\mathrm{u}}(\varphi_1, \vartheta_1) & \mathbf{a}_{\mathrm{u}}(\varphi_2, \vartheta_2) & \ldots & \mathbf{a}_{\mathrm{u}}(\varphi_K, \vartheta_K) \end{bmatrix} \mathbf{s}(t) + \mathbf{n}(t),$$

where $\mathbf{y}(t) \in \mathbb{C}^{M\times 1}$, $\mathbf{s}(t) \in \mathbb{C}^{K\times 1}$ denotes the vector of source signals, and $\mathbf{n}(t)$ represents additive measurement noise.

The vector $\mathbf{a}_{\mathrm{u}}(\varphi_i, \vartheta_i)$ denotes the U-probe array response vector corresponding to the i-th source and is given by

$$\mathbf{a}_{\mathrm{u}}(\varphi_i, \vartheta_i) = \begin{bmatrix} \sin(\vartheta_i)\cos(\delta_1 - \varphi_i) e^{j\kappa\mathbf{r}_1\cdot\mathbf{u}_i} \\ \sin(\vartheta_i)\cos(\delta_2 - \varphi_i) e^{j\kappa\mathbf{r}_2\cdot\mathbf{u}_i} \\ \vdots \\ \sin(\vartheta_i)\cos(\delta_M - \varphi_i) e^{j\kappa\mathbf{r}_M\cdot\mathbf{u}_i} \end{bmatrix}.$$

This expression explicitly shows the particle velocity responses for each AVS element with arbitrary orientation of U-probes through $\boldsymbol{\delta}$.

For convenience, the array response vector can also be expressed using the pressure-only steering vector. To see this, recall that this steering vector is given by

$$\mathbf{a}_{\mathrm{p}}(\varphi_i, \vartheta_i) = \begin{bmatrix} e^{j\kappa\mathbf{r}_1\cdot\mathbf{u}_i} & e^{j\kappa\mathbf{r}_2\cdot\mathbf{u}_i} & \ldots & e^{j\kappa\mathbf{r}_M\cdot\mathbf{u}_i} \end{bmatrix}^T. \tag{1.4}$$

Further, we can define the gain vector of the U-probe for the i-th source as

$$\mathbf{p}_i = \begin{bmatrix} \sin(\vartheta_i)\cos(\delta_1 - \varphi_i) \\ \sin(\vartheta_i)\cos(\delta_2 - \varphi_i) \\ \vdots \\ \sin(\vartheta_i)\cos(\delta_M - \varphi_i) \end{bmatrix}.$$

Using these definitions, the U-probe array response vector can also be written as

$$\mathbf{a}_{\mathrm{u}}(\varphi_i, \vartheta_i) = \mathbf{a}_{\mathrm{p}}(\varphi_i, \vartheta_i) \circ \mathbf{p}_i,$$

where $\circ$ denotes the Hadamard (element-wise) product. Specifically, the measurement model becomes

$$\mathbf{y}(t) = \begin{bmatrix} \mathbf{a}_{\mathrm{p}}(\varphi_1, \vartheta_1) \circ \mathbf{p}_1 & \mathbf{a}_{\mathrm{p}}(\varphi_2, \vartheta_2) \circ \mathbf{p}_2 & \dots & \mathbf{a}_{\mathrm{p}}(\varphi_K, \vartheta_K) \circ \mathbf{p}_K \end{bmatrix} \mathbf{s}(t) + \mathbf{n}(t).$$

1.6.2 Uniaxial PU-Probe Array Model

The measurement vector of the PU-probe array can be modeled as

$$\mathbf{y}(t) = \begin{bmatrix} \mathbf{a}_{\mathrm{pu}}(\varphi_1, \vartheta_1) & \mathbf{a}_{\mathrm{pu}}(\varphi_2, \vartheta_2) & \dots & \mathbf{a}_{\mathrm{pu}}(\varphi_K, \vartheta_K) \end{bmatrix} \mathbf{s}(t) + \mathbf{n}(t),$$

where $\mathbf{y}(t) \in \mathbb{C}^{2M \times 1}$, $\mathbf{s}(t) \in \mathbb{C}^{K \times 1}$ denotes the vector of source signals, and $\mathbf{n}(t)$ represents additive measurement noise.

The vector $\mathbf{a}_{\mathrm{pu}}(\varphi_i, \vartheta_i)$ denotes the PU-probe array response vector corresponding to the i-th source and is given by

$$\mathbf{a}_{\mathrm{pu}}(\varphi_i, \vartheta_i) = \begin{bmatrix} e^{j\kappa \mathbf{r}_1 \cdot \mathbf{u}_i} \\ \sin(\vartheta_i)\cos(\delta_1 - \varphi_i) e^{j\kappa \mathbf{r}_1 \cdot \mathbf{u}_i} \\ \vdots \\ e^{j\kappa \mathbf{r}_M \cdot \mathbf{u}_i} \\ \sin(\vartheta_i)\cos(\delta_M - \varphi_i) e^{j\kappa \mathbf{r}_M \cdot \mathbf{u}_i} \end{bmatrix}.$$

This expression explicitly shows the pressure and particle velocity responses for each AVS element with arbitrary orientation of the PU-probes through $\boldsymbol{\delta}$.

Using the definition in (1.4), an extended response corresponding to an APS array can be written as

$$\mathbf{a}_{\mathrm{pe},i} = \mathbf{a}_{\mathrm{p}}(\varphi_i, \vartheta_i) \otimes \begin{bmatrix} 1 \\ 1 \end{bmatrix},$$

where $\otimes$ denotes the Kronecker product.

The PU-probe based AVS response can then be expressed as a Hadamard product between this extended APS response and an orientation-dependent gain vector. Specifically, the PU-probe measurement model becomes

$$\mathbf{y}(t) = \begin{bmatrix} \mathbf{a}_{\mathrm{pe},1} \circ \mathbf{p}_{\mathrm{e},1} & \mathbf{a}_{\mathrm{pe},2} \circ \mathbf{p}_{\mathrm{e},2} & \dots & \mathbf{a}_{\mathrm{pe},K} \circ \mathbf{p}_{\mathrm{e},K} \end{bmatrix} \mathbf{s}(t) + \mathbf{n}(t),$$

and the gain vector of the PU-probe for the i-th source is defined as

$$\mathbf{p}_{\mathrm{e},i} = \begin{bmatrix} 1 \\ \sin(\vartheta_i)\cos(\delta_1 - \varphi_i) \\ \vdots \\ 1 \\ \sin(\vartheta_i)\cos(\delta_M - \varphi_i) \end{bmatrix}.$$

This formulation clearly separates the spatial phase response of the array from the directional sensitivity introduced by the arbitrary orientation of the particle velocity sensors in the AVS array.

1.7 Outline

This thesis studies DoA estimation in underdetermined cases using a circular AVS array. It builds an augmented co-array to increase degrees of freedom, maps it to a virtual ULA via the Jacobi–Anger expansion, and applies ESPRIT and Root-MUSIC. To handle single-snapshot limits, inverse modeling with spatial smoothing (IMSS) and atomic norm minimization (ANM) are used, with performance evaluated across AVS configurations. The structure of the thesis is as follows.

Chapter 2: This chapter develops the signal model for a UCA by specializing the general uniaxial AVS formulation. It presents three sensing configurations namely pressure sensors, uniaxial U-probes, and uniaxial PU-probes. The corresponding array response models are established, forming the basis for subsequent co-array and DoA estimation methods.

Chapter 3: The co-array principle is introduced to construct a virtual array with increased aperture and degrees of freedom by exploiting second-order statistics. It formulates the co-array for UCAs with assuming only uncorrelated sources, and develops representations for pressure sensor, U-probe, and PU-probe configurations.

Chapter 4: This chapter transforms the UCA co-array into an equivalent virtual ULA representation to obtain the shift-invariance Vandermonde structure required by high-resolution gridless subspace-based DoA estimation methods. Using the Jacobi–Anger expansion, harmonic representations are developed for the pressure-only, uniaxial U-probe, and uniaxial PU-probe co-array structures.

Chapter 5: In this chapter, the virtual ULA representation is exploited to apply high-resolution gridless DoA estimation methods such as ESPRIT and Root-MUSIC. Here the single-snapshot limitation inherent to correlation-based processing is addressed by introducing techniques such as IMSS and ANM.

Chapter 6: This chapter evaluates the proposed framework through three stages. First, a baseline comparison using MUSIC is performed in an overdetermined setting

($K < M$), including an analysis of the resulting spectra. Next, single-realization results illustrate the performance in underdetermined scenarios ($K > M$). Finally, a Monte Carlo study evaluates the RMSE of DoA estimation as a function of SNR, providing a statistical assessment across different sensing configurations.

Chapter 7: This chapter concludes the thesis by summarizing the proposed co-array–based DoA estimation framework for underdetermined scenarios using circular AVS measurements. It highlights the effectiveness of virtual array formation, the role of IMSS and ANM in overcoming single-snapshot limitations, and the performance gains achieved with different sensing configurations, while also discussing trade-offs in complexity and outlining directions for future work.

2 Signal Model for UCA

DoA estimation relies on an accurate mathematical description of both the array geometry and the received signals. Previously, the general measurement model for a uniaxial AVS-based array was introduced including U-probe consisting of a particle velocity sensor and PU-probe, where each sensor consists of a pressure component and a particle velocity component with arbitrary orientation. In particular, the measurement model and the corresponding array response vector were described in Section 1.6.

In this chapter, we specialize that general formulation to the case of a UCA. Three sensing configurations are considered. The first corresponds to a conventional array composed only of acoustic pressure sensors. The second corresponds to an array that uses only the uniaxial U-probe measurements. The third configuration corresponds to a UCA employing both the pressure and the particle velocity components of the uniaxial PU-probes. These models will later serve as the foundation for the underdetermined gridless DoA estimation framework developed in this work.

2.1 Geometry of the Uniform Circular Array

A UCA consists of M sensors equally spaced along a circle of radius R. Without loss of generality, the array is assumed to lie on the xy-plane with its center located at the origin. This assumption is consistent with the planar configuration adopted in Section 1.6, where all sensors are assumed to lie on a common plane.

The angular position of the m-th sensor on the circle is defined as

$$\phi_m = \frac{2\pi(m-1)}{M}, \quad m = 1, 2, \ldots, M.$$

The corresponding Cartesian coordinates of the m-th sensor location are therefore

$$\mathbf{r}_m = \begin{bmatrix} R\cos(\phi_m) \\ R\sin(\phi_m) \\ 0 \end{bmatrix}.$$

Consider K far-field narrowband acoustic sources impinging on the array from distinct spatial directions. The direction of the k-th source is described using spherical coordinates, where ϑ_k denotes the elevation angle and φ_k denotes the azimuth angle. As introduced in (1.1), the propagation direction can be represented by the unit vector

$$\mathbf{u}(\varphi_k, \vartheta_k) = \begin{bmatrix} \sin(\vartheta_k)\cos(\varphi_k) \\ \sin(\vartheta_k)\sin(\varphi_k) \\ \cos(\vartheta_k) \end{bmatrix}.$$

2.2 Narrowband Signal Model

Under the far-field assumption, the acoustic wavefronts arriving at the array can be approximated as plane waves. The propagation delay experienced by the signal at the m-th sensor relative to the array center depends on the projection of the sensor position vector onto the propagation direction. For the m-th sensor and the k-th source, the propagation delay relative to the array center is given by

$$\tau_{m,k} = \frac{1}{c}\mathbf{r}_m \cdot \mathbf{u}(\varphi_k, \vartheta_k),$$

where c denotes the speed of sound.

Let $s_k[l]$ denote the narrowband signal emitted by the k-th source. Under the narrowband assumption, propagation delays mainly affect the phase of the received signal. Consequently, the l-th snapshot of the noiseless received signal at the m-th pressure sensor can be written as

$$x_{\mathrm{p},m}[l] = \sum_{k=1}^{K} s_k[l] e^{j\kappa \mathbf{r}_m \cdot \mathbf{u}(\varphi_k, \vartheta_k)}.$$

Substituting the expression for the sensor position vector yields

$$\mathbf{r}_m \cdot \mathbf{u}(\varphi_k, \vartheta_k) = R\sin(\vartheta_k)\left(\cos(\phi_m)\cos(\varphi_k) + \sin(\phi_m)\sin(\varphi_k)\right).$$

Using the trigonometric identity for the cosine of angle differences, the expression simplifies to

$$\mathbf{r}_m \cdot \mathbf{u}(\varphi_k, \vartheta_k) = R\sin(\vartheta_k)\cos(\phi_m - \varphi_k).$$

Therefore, the received signal at the m-th sensor becomes

$$x_{\mathrm{p},m}[l] = \sum_{k=1}^{K} s_k[l] e^{j\kappa R \sin(\vartheta_k)\cos(\phi_m - \varphi_k)}.$$

2.3 Pressure Array Representation

To express the array model compactly, the outputs of all sensors are stacked into the observation vector

$$\mathbf{x}_{\mathrm{p}}[l] = \begin{bmatrix} x_{\mathrm{p},1}[l] \\ x_{\mathrm{p},2}[l] \\ \vdots \\ x_{\mathrm{p},M}[l] \end{bmatrix}.$$

As illustrated in Figure 2.1, the array receives K far-field plane waves arriving from directions (φ_k, ϑ_k), where φ_k and ϑ_k denote the azimuth and elevation angles of the k-th source, respectively. Each incident wave produces a pressure signal at each sensor with a phase shift determined by the propagation delay between the source direction and the sensor location.

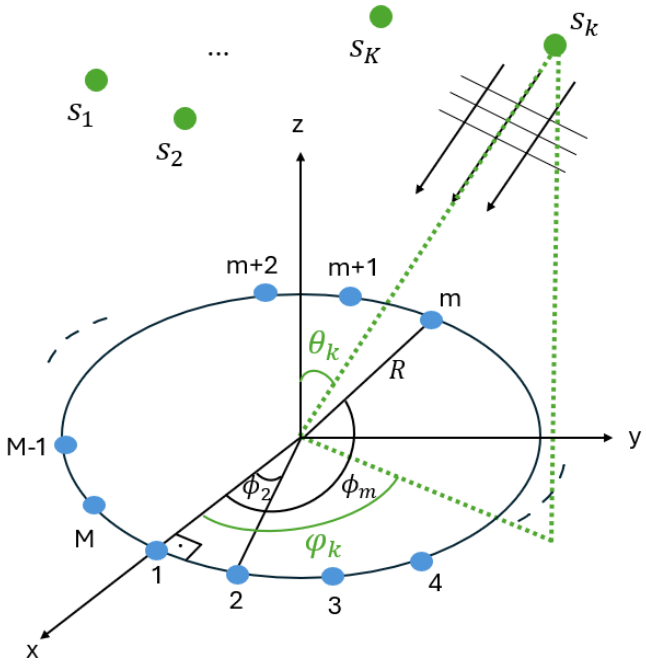


Figure 2.1: Measurement model of a UCA composed of pressure sensors (blue). The array consists of M sensors uniformly distributed on a circle of radius R. Multiple incident plane waves $k = 1, \cdots, K$ arrive from directions (φ_k, ϑ_k), producing pressure measurements at each sensor.

For a source arriving from direction (φ_k, ϑ_k), the corresponding steering vector of the pressure array is defined as

$$\mathbf{a}_{\mathrm{p}}(\varphi_k, \vartheta_k) = \begin{bmatrix} e^{j\kappa R \sin(\vartheta_k)\cos(\phi_1 - \varphi_k)} \\ e^{j\kappa R \sin(\vartheta_k)\cos(\phi_2 - \varphi_k)} \\ \vdots \\ e^{j\kappa R \sin(\vartheta_k)\cos(\phi_M - \varphi_k)} \end{bmatrix}.$$

This steering vector corresponds to the pressure response $\mathbf{a}_{\mathrm{p}}(\varphi_k, \vartheta_k)$ defined in (1.4). Stacking the steering vectors associated with all K sources forms the pressure array manifold matrix

$$\mathbf{A}_{\mathrm{p}}(\boldsymbol{\varphi}, \boldsymbol{\vartheta}) = \begin{bmatrix} \mathbf{a}_{\mathrm{p}}(\varphi_1, \vartheta_1) & \mathbf{a}_{\mathrm{p}}(\varphi_2, \vartheta_2) & \cdots & \mathbf{a}_{\mathrm{p}}(\varphi_K, \vartheta_K) \end{bmatrix},$$

where $\boldsymbol{\varphi} = [\varphi_1, \varphi_2, \ldots, \varphi_M]^T$ and $\boldsymbol{\vartheta} = [\vartheta_1, \vartheta_2, \ldots, \vartheta_M]^T$ are all K sources' azimuth and elevation angles, respectively.

Defining the source signal vector $\mathbf{s}[l] = \begin{bmatrix} s_1[l], s_2[l], \ldots, s_K[l] \end{bmatrix}^\top$, the array observation model can be written compactly as

$$\mathbf{x}_{\mathrm{p}}[l] = \mathbf{A}_{\mathrm{p}}(\boldsymbol{\varphi}, \boldsymbol{\vartheta})\mathbf{s}[l]. \tag{2.1}$$

This model describes the response of a pressure-based UCA to multiple far-field sources in a noiseless scenario.

2.4 Uniaxial U-Probe Array

We now consider the case where each sensor measures only a single component of the particle velocity, i.e., a uniaxial U-probe. The outputs of all U-probes are stacked into the observation vector

$$\mathbf{x}_{\mathrm{u}}[l] = \begin{bmatrix} x_{\mathrm{u},1}[l] \\ x_{\mathrm{u},2}[l] \\ \vdots \\ x_{\mathrm{u},M}[l] \end{bmatrix}.$$

As illustrated in Figure 2.2, the array receives K far-field plane waves arriving from directions (φ_k, ϑ_k), where φ_k and ϑ_k denote the azimuth and elevation angles of the k-th source, respectively. Let δ_m denote the orientation of the U-probe at the m-th array location. The response of the m-th uniaxial U-probe to a source arriving from direction (φ_k, ϑ_k) is proportional to the directional factor $\sin(\vartheta_k)\cos(\delta_m - \varphi_k)$. As described in Subsection 1.6.1, the particle velocity response depends on both the DoA and the orientation of the U-probe.

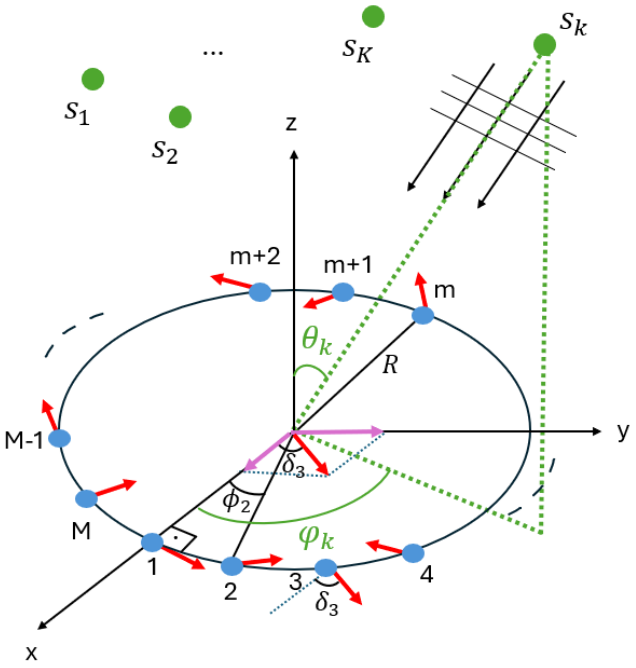


Figure 2.2: Measurement model of a UCA composed of U-probes (blue) that are arbitrarily oriented (red arrow).

Therefore, the steering vector corresponding to the uniaxial U-probe UCA becomes

$$\mathbf{a}_{\mathrm{u}}(\varphi_k, \vartheta_k) = \begin{bmatrix} \sin(\vartheta_k)\cos(\delta_1 - \varphi_k) e^{j\kappa R \sin(\vartheta_k)\cos(\phi_1 - \varphi_k)} \\ \sin(\vartheta_k)\cos(\delta_2 - \varphi_k) e^{j\kappa R \sin(\vartheta_k)\cos(\phi_2 - \varphi_k)} \\ \vdots \\ \sin(\vartheta_k)\cos(\delta_M - \varphi_k) e^{j\kappa R \sin(\vartheta_k)\cos(\phi_M - \varphi_k)} \end{bmatrix}.$$

Stacking the steering vectors corresponding to the K sources gives the U-probe array manifold matrix

$$\mathbf{A}_{\mathrm{u}}(\boldsymbol{\varphi}, \boldsymbol{\vartheta}) = \begin{bmatrix} \mathbf{a}_{\mathrm{u}}(\varphi_1, \vartheta_1) & \mathbf{a}_{\mathrm{u}}(\varphi_2, \vartheta_2) & \cdots & \mathbf{a}_{\mathrm{u}}(\varphi_K, \vartheta_K) \end{bmatrix}.$$

The observation model can therefore be written as

$$\mathbf{x}_{\mathrm{u}}[l] = \mathbf{A}_{\mathrm{u}}(\boldsymbol{\varphi}, \boldsymbol{\vartheta})\mathbf{s}[l]. \tag{2.2}$$

This model captures the response of a U-probe-based UCA to multiple far-field sources.

2.5 Uniaxial PU-Probe Array

Finally, we consider the configuration where each array element is a PU-probe measuring both acoustic pressure and a uniaxial particle velocity component. This corresponds to the AVS configuration introduced in Subsection 1.6.2. The observation vector therefore becomes

$$\mathbf{x}_{\mathrm{pu}}[l] = \begin{bmatrix} x_{\mathrm{p},1}[l] \\ x_{\mathrm{u},1}[l] \\ \vdots \\ x_{\mathrm{p},M}[l] \\ x_{\mathrm{u},M}[l] \end{bmatrix} \in \mathbb{C}^{2M\times 1}.$$

For a source arriving from direction (φ_k, ϑ_k), the steering vector of the PU-probe based UCA can be written as

$$\mathbf{a}_{\mathrm{pu}}(\varphi_k, \vartheta_k) = \begin{bmatrix} e^{j\kappa R\sin(\vartheta_k)\cos(\phi_1-\varphi_k)} \\ \sin(\vartheta_k)\cos(\delta_1-\varphi_k)e^{j\kappa R\sin(\vartheta_k)\cos(\phi_1-\varphi_k)} \\ \vdots \\ e^{j\kappa R\sin(\vartheta_k)\cos(\phi_M-\varphi_k)} \\ \sin(\vartheta_k)\cos(\delta_M-\varphi_k)e^{j\kappa R\sin(\vartheta_k)\cos(\phi_M-\varphi_k)} \end{bmatrix}.$$

Stacking the steering vectors associated with all sources forms the PU array manifold matrix

$$\mathbf{A}_{\mathrm{pu}}(\boldsymbol{\varphi}, \boldsymbol{\vartheta}) = \begin{bmatrix} \mathbf{a}_{\mathrm{pu}}(\varphi_1, \vartheta_1) & \mathbf{a}_{\mathrm{pu}}(\varphi_2, \vartheta_2) & \cdots & \mathbf{a}_{\mathrm{pu}}(\varphi_K, \vartheta_K) \end{bmatrix}.$$

The noiseless observation model for the PU-probe based UCA can therefore be written as

$$\mathbf{x}_{\mathrm{pu}}[l] = \mathbf{A}_{\mathrm{pu}}(\boldsymbol{\varphi}, \boldsymbol{\vartheta})\mathbf{s}[l]. \tag{2.3}$$

This formulation incorporates both the pressure and directional particle velocity measurements, providing additional spatial information that can improve DoA estimation performance.

2.6 Conclusion

In this chapter, signal models for UCAs employing pressure sensors, uniaxial U-probes, and uniaxial PU-probes were derived under the narrowband far-field assumption. The corresponding steering vectors and array manifold matrices were formulated. These physical array models in (2.1), (2.2) and (2.3) can be directly used for DoA estimation, potentially after transformation to a virtual ULA as will be discussed in Section 4. However, it remains limited in the number of sources it can resolve. To overcome this limitation, the co-array concept is introduced in the following chapter, as it effectively increases the degrees of freedom and enables the identifiability of a larger number of sources. The structure of the array manifold matrices $\mathbf{A}_{\mathrm{p}}(\boldsymbol{\varphi}, \boldsymbol{\vartheta})$, $\mathbf{A}_{\mathrm{u}}(\boldsymbol{\varphi}, \boldsymbol{\vartheta})$ and $\mathbf{A}_{\mathrm{pu}}(\boldsymbol{\varphi}, \boldsymbol{\vartheta})$ will be further exploited in the following chapter when introducing co-array representations.

3 UCA Co-Array Structure

The co-array principle enables the construction of a virtual array with enhanced aperture and degrees of freedom from a physical array. This is achieved by exploiting the second-order statistics of the received signals, whereby the covariance matrix is vectorized to form an equivalent virtual array with increased effective elements. This virtual representation provides additional spatial information that can be leveraged for improved DoA estimation when we have more sources than physical sensors.

The application of the co-array concept to UCAs has been previously investigated in [31], where the formulation relies on the assumption of quasi-stationary sources. In contrast, the approach adopted in this work does not require statistical quasi-stationarity. Instead, we only assume that the sources are mutually uncorrelated, which is a standard and widely accepted assumption in array signal processing. Under this condition, the signal covariance matrix admits a structured representation that can be vectorized to reveal the underlying virtual array geometry.

In the following, we detail the co-array structure for three considered sensing modalities: pressure-only sensors, uniaxial U-probes, and uniaxial PU-probes.

3.1 Pressure Co-Array Structure

Assuming K narrowband, far-field, and mutually uncorrelated sources, the covariance matrix of a UCA with M pressure sensors is given by

$$\mathbf{R}_{\mathrm{p}} = \mathbb{E}\{\mathbf{x}_{\mathrm{p}}[l]\mathbf{x}_{\mathrm{p}}[l]^{\mathsf{H}}\} = \mathbf{A}_{\mathrm{p}}(\boldsymbol{\varphi},\boldsymbol{\vartheta})\mathrm{diag}(\boldsymbol{\gamma})\mathbf{A}_{\mathrm{p}}(\boldsymbol{\varphi},\boldsymbol{\vartheta})^{\mathsf{H}},$$

where $\boldsymbol{\gamma} = [\gamma_1,\dots,\gamma_K]^\top$ contains the source powers, with $\gamma_k = \mathbb{E}\{|s_k[l]|^2\}$.

Vectorizing the covariance matrix yields

$$\tilde{\mathbf{r}}_{\mathrm{p}} = \mathrm{vec}(\mathbf{R}_{\mathrm{p}}) = \left(\mathbf{A}_{\mathrm{p}}(\boldsymbol{\varphi},\boldsymbol{\vartheta})^* \odot \mathbf{A}_{\mathrm{p}}(\boldsymbol{\varphi},\boldsymbol{\vartheta})\right)\boldsymbol{\gamma} = \mathbf{A}_{\mathrm{p,co}}(\boldsymbol{\varphi},\boldsymbol{\vartheta})\boldsymbol{\gamma}, \tag{3.1}$$

where $\odot$ denotes the Khatri–Rao product and $\mathbf{A}_{\mathrm{p,co}}(\boldsymbol{\varphi},\boldsymbol{\vartheta}) \in \mathbb{C}^{M^2\times K}$ is the co-array manifold matrix.

Each column of $\mathbf{A}_{\mathrm{p,co}}(\boldsymbol{\varphi},\boldsymbol{\vartheta})$ is given by

$$\mathbf{a}_{\mathrm{p,co}}(\varphi,\vartheta) = \mathbf{a}_{\mathrm{p}}^*(\varphi,\vartheta) \otimes \mathbf{a}_{\mathrm{p}}(\varphi,\vartheta) = \mathrm{vec}\left(\mathbf{a}_{\mathrm{p}}(\varphi,\vartheta)\mathbf{a}_{\mathrm{p}}(\varphi,\vartheta)^{\mathsf{H}}\right).$$

If we assign to every index i of $\mathbf{a}_{\mathrm{p,co}}(\varphi,\vartheta)$ a pair (m,n) according to $i = (m-1)M+n$, then the i-th entry of $\mathbf{a}_{\mathrm{p,co}}(\varphi,\vartheta)$ can be written as

$$\begin{aligned}[\mathbf{a}_{\mathrm{p,co}}(\varphi,\vartheta)]_i &= a_{\mathrm{p},m}^*(\varphi,\vartheta)a_{\mathrm{p},n}(\varphi,\vartheta) \\ &= \exp\big(j\kappa R\sin(\vartheta)\big(\cos(\phi_n-\varphi)-\cos(\phi_m-\varphi)\big)\big).\end{aligned} \tag{3.2}$$

We can further simplify this expression by introducing $d_i = \cos(\phi_n - \varphi) - \cos(\phi_m - \varphi) = -2\sin(\frac{\phi_n - \phi_m}{2})\sin(\frac{\phi_n + \phi_m}{2} - \varphi)$. To relate a location to this expression, we can introduce $\zeta_{mn} = 2|\sin(\frac{\phi_n - \phi_m}{2})|$ and $\psi_{mn} = \frac{\phi_n + \phi_m}{2} + \frac{\pi}{2} - I(\sin(\frac{\phi_n - \phi_m}{2}) < 0)\pi$, where $I(\cdot)$ represents the indicator function. We can then rewrite (3.2) as

$$[\mathbf{a}_{\mathrm{p,co}}(\varphi, \vartheta)]_i = \exp(j\kappa R\zeta_{mn}\sin(\vartheta)\cos(\psi_{mn} - \varphi))\,. \tag{3.3}$$

This expression reveals that the co-array consists of multiple concentric circles with radii $R\zeta_{mn}$. For each radius, multiple angular positions ψ_{mn} are obtained. For odd (even) M, this results in $\frac{M-1}{2}$ ($\frac{M}{2}$) distinct radii, each containing $2M$ (M) angular samples, excluding the origin. An example of a UCA co-array is illustrated in Figure 3.1.

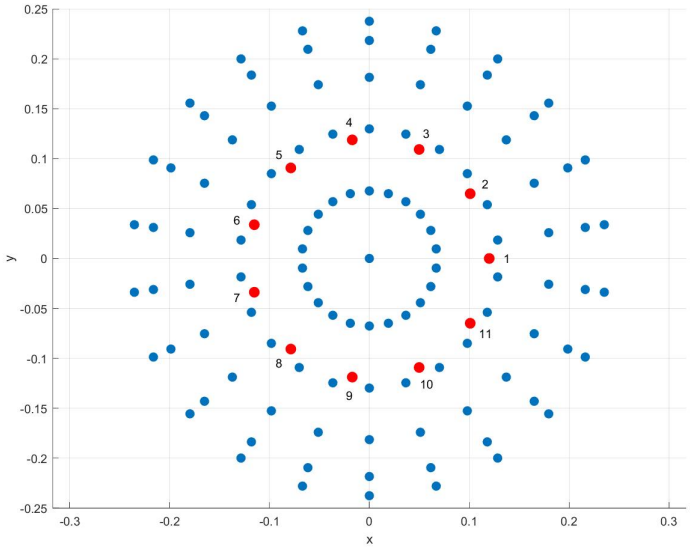


Figure 3.1: Co-array sensor locations (blue) derived from physical UCA sensor positions (red), $M = 11$ and $R = 2.8\lambda$.

3.1.1 Non-Redundant Co-Array Construction via Selection Matrix

Note that some entries in the co-array response vector $\mathbf{a}_{\mathrm{p,co}}(\varphi, \vartheta)$ can be repeated, because different (m, n) pairs can yield the same difference $d_i = \cos(\phi_n - \varphi) - \cos(\phi_m - \varphi)$. Let $\mathbf{b}_{\mathrm{p}}(\varphi, \vartheta)$ be the non-redundant co-array response vector where we assume that $f(i)$ is the row index of $\mathbf{b}(\varphi, \vartheta)$ that corresponds to the i-th row of $\mathbf{a}_{\mathrm{p,co}}(\varphi, \vartheta)$, i.e., $[\mathbf{b}_{\mathrm{p}}(\varphi, \vartheta)]_{f(i)} = [\mathbf{a}_{\mathrm{p,co}}(\varphi, \vartheta)]_i$. Similarly, we can define a selection matrix $\mathbf{J}$ such that $\mathbf{b}_{\mathrm{p}}(\varphi, \vartheta) = \mathbf{J}\mathbf{a}_{\mathrm{p,co}}(\varphi, \vartheta)$. The size of $\mathbf{b}_{\mathrm{p}}(\varphi, \vartheta)$ represents the number of distinct differences d_i (degrees of freedom of the co-array). It can be denoted as $M_{b,\mathrm{co}}^{(\mathrm{p})}$ and equals the product of the number of radii of the co-array times the number of angles per radius (plus one for the center element):

$$M_{b,\mathrm{co}}^{(\mathrm{p})} = \begin{cases} \frac{M^2}{2} + 1, & \text{if } M \text{ is even,} \\ M^2 - M + 1, & \text{if } M \text{ is odd.} \end{cases}$$

A rigorous proof is provided in [31]. The vector of non-redundant correlations can finally be derived from (3.1) as

$$\mathbf{r}_{\mathrm{p}} = \mathbf{J}\tilde{\mathbf{r}}_{\mathrm{p}} = \mathbf{J}\mathbf{A}_{\mathrm{p,co}}(\boldsymbol{\varphi}, \boldsymbol{\vartheta})\boldsymbol{\gamma} = \mathbf{B}_{\mathrm{p}}(\boldsymbol{\varphi}, \boldsymbol{\vartheta})\boldsymbol{\gamma}, \tag{3.4}$$

where $\mathbf{B}_{\mathrm{p}}(\varphi, \vartheta) = \mathbf{J}\mathbf{A}_{\mathrm{p,co}}(\varphi, \vartheta) \in \mathbb{C}^{M_{b,\mathrm{co}}^{(\mathrm{p})} \times K}$ is the non-redundant co-array manifold matrix. Note that we can also write $\mathbf{B}_{\mathrm{p}}(\boldsymbol{\varphi}, \boldsymbol{\vartheta}) = [\mathbf{b}_{\mathrm{p}}(\varphi_1, \vartheta_1), \mathbf{b}_{\mathrm{p}}(\varphi_2, \vartheta_2), \ldots, \mathbf{b}_{\mathrm{p}}(\varphi_K, \vartheta_K)]$.

3.1.2 Redundant Co-Array Construction for Averaging

In contrast to the non-redundant formulation, one may retain all entries of the co-array response vector $\mathbf{a}_{\mathrm{p,co}}(\varphi, \vartheta)$, including repeated elements corresponding to identical differences d_i. This leads to a redundant co-array representation, where multiple (m, n) pairs contribute to the same spatial lag.

Accordingly, we directly work with the vector of correlations $\tilde{\mathbf{r}}_{\mathrm{p}}$ defined in (3.1), i.e., $\tilde{\mathbf{r}}_{\mathrm{p}} = \mathbf{A}_{\mathrm{p,co}}(\boldsymbol{\varphi}, \boldsymbol{\vartheta})\boldsymbol{\gamma}$. In this representation, redundant entries corresponding to identical co-array lags are preserved rather than eliminated. While this does not increase the number of degrees of freedom, it provides multiple observations of the same spatial lag, which can be beneficial in practical scenarios with finite snapshots.

In particular, when the number of samples is limited or the signal-to-noise ratio (SNR) is low, these repeated entries enable averaging over identical lags. This improves the robustness of the covariance estimates by reducing variance. Such an advantage is especially pronounced when combined with spatial smoothing techniques (see Section 5.1), where the redundancy is explicitly exploited to enhance estimation performance.

Therefore, although the non-redundant co-array representation is attractive from a degrees of freedom perspective, the redundant formulation can yield improved estimation accuracy in practice due to its inherent averaging effect under finite-sample conditions, particularly when combined with spatial smoothing techniques.

In summary, for the pressure-only case, we consider two formulations: a non-redundant co-array representation with $M_{b,\mathrm{co}}^{(\mathrm{p})} = \mathcal{O}(M^2)$, and a redundant representation in which all entries are retained, yielding $M_{a,\mathrm{co}}^{(\mathrm{p})} = M^2$. This co-array construction procedure illustrates that, by directly working with the correlations of the UCA observations, we can increase the number of antennas from M to $\mathcal{O}(M^2)$.

3.2 Uniaxial U-Probe Co-Array Structure

For uniaxial U-probes, each sensor measures the projection of the particle velocity along a given orientation. As a result, the array response depends on both the azimuth angle φ and the elevation angle ϑ, as well as the sensor orientations $\{\delta_m\}_{m=1}^{M}$.

We begin by defining the direction-dependent response gain vector

$$\mathbf{d}(\varphi, \vartheta, \boldsymbol{\delta}) = \begin{bmatrix} \sin(\vartheta)\cos(\delta_1 - \varphi) \\ \vdots \\ \sin(\vartheta)\cos(\delta_M - \varphi) \end{bmatrix},$$

where $\boldsymbol{\delta} = [\delta_1, \delta_2, \ldots, \delta_M]^T$ collects the orientations of all uniaxial velocity sensors. Using this, the response gain vector for a single source can be expressed as

$$\mathbf{a}_{\mathrm{u}}(\varphi, \vartheta) = \operatorname{diag}\big(\mathbf{d}(\varphi, \vartheta, \boldsymbol{\delta})\big)\mathbf{a}_{\mathrm{p}}(\varphi, \vartheta), \tag{3.5}$$

where $\mathbf{a}_{\mathrm{p}}(\varphi, \vartheta)$ denotes the pressure response vector.

Extending this to K sources, we define the matrix $\mathbf{H}(\boldsymbol{\varphi}, \boldsymbol{\vartheta}) \in \mathbb{R}^{M \times K}$ whose k-th column is given by $\mathbf{d}(\varphi_k, \vartheta_k, \boldsymbol{\delta})$. The particle velocity array manifold can then be written as the Hadamard product

$$\mathbf{A}_{\mathrm{u}}(\boldsymbol{\varphi}, \boldsymbol{\vartheta}) = \mathbf{H}(\boldsymbol{\varphi}, \boldsymbol{\vartheta}) \circ \mathbf{A}_{\mathrm{p}}(\boldsymbol{\varphi}, \boldsymbol{\vartheta}). \tag{3.6}$$

With the assumption of uncorrelated sources, the covariance matrix is given by

$$\mathbf{R}_{\mathrm{u}} = \mathbf{A}_{\mathrm{u}}(\boldsymbol{\varphi}, \boldsymbol{\vartheta})\operatorname{diag}(\boldsymbol{\gamma})\mathbf{A}_{\mathrm{u}}(\boldsymbol{\varphi}, \boldsymbol{\vartheta})^{\mathsf{H}}.$$

Vectorization yields the co-array model

$$\tilde{\mathbf{r}}_{\mathrm{u}} = \left(\mathbf{A}_{\mathrm{u}}^{*}(\boldsymbol{\varphi}, \boldsymbol{\vartheta}) \odot \mathbf{A}_{\mathrm{u}}(\boldsymbol{\varphi}, \boldsymbol{\vartheta})\right)\boldsymbol{\gamma} = \mathbf{A}_{\mathrm{u,co}}(\boldsymbol{\varphi}, \boldsymbol{\vartheta})\boldsymbol{\gamma}. \tag{3.7}$$

Substituting the Hadamard structure of $\mathbf{A}_{\mathrm{u}}(\boldsymbol{\varphi}, \boldsymbol{\vartheta})$ in (3.6), we obtain

$$\begin{aligned}
\mathbf{A}_{\mathrm{u,co}}(\boldsymbol{\varphi}, \boldsymbol{\vartheta}) &= \mathbf{A}_{\mathrm{u}}^{*}(\boldsymbol{\varphi}, \boldsymbol{\vartheta}) \odot \mathbf{A}_{\mathrm{u}}(\boldsymbol{\varphi}, \boldsymbol{\vartheta}) \\
&= \big(\mathbf{H}(\boldsymbol{\varphi}, \boldsymbol{\vartheta}) \circ \mathbf{A}_{\mathrm{p}}(\boldsymbol{\varphi}, \boldsymbol{\vartheta})\big)^{*} \odot \big(\mathbf{H}(\boldsymbol{\varphi}, \boldsymbol{\vartheta}) \circ \mathbf{A}_{\mathrm{p}}(\boldsymbol{\varphi}, \boldsymbol{\vartheta})\big) \\
&= \big(\mathbf{H}^{*}(\boldsymbol{\varphi}, \boldsymbol{\vartheta}) \circ \mathbf{A}_{\mathrm{p}}^{*}(\boldsymbol{\varphi}, \boldsymbol{\vartheta})\big) \odot \big(\mathbf{H}(\boldsymbol{\varphi}, \boldsymbol{\vartheta}) \circ \mathbf{A}_{\mathrm{p}}(\boldsymbol{\varphi}, \boldsymbol{\vartheta})\big) \\
&= \big(\mathbf{H}^{*}(\boldsymbol{\varphi}, \boldsymbol{\vartheta}) \odot \mathbf{H}(\boldsymbol{\varphi}, \boldsymbol{\vartheta})\big) \circ \big(\mathbf{A}_{\mathrm{p}}^{*}(\boldsymbol{\varphi}, \boldsymbol{\vartheta}) \odot \mathbf{A}_{\mathrm{p}}(\boldsymbol{\varphi}, \boldsymbol{\vartheta})\big).
\end{aligned}$$

This expression shows that the U-probe co-array can be interpreted as an element-wise weighted version of the pressure co-array, where the weighting is determined by the directional response matrix $\mathbf{H}(\boldsymbol{\varphi}, \boldsymbol{\vartheta})$.

Note that we can write $\mathbf{A}_{\mathrm{u,co}}(\boldsymbol{\varphi}, \boldsymbol{\vartheta}) = [\mathbf{a}_{\mathrm{u,co}}(\varphi_1, \vartheta_1), \mathbf{a}_{\mathrm{u,co}}(\varphi_2, \vartheta_2), \ldots, \mathbf{a}_{\mathrm{u,co}}(\varphi_K, \vartheta_K)]$ with co-array velocity response vector given by

$$\mathbf{a}_{\mathrm{u,co}}(\varphi, \vartheta) = \mathbf{a}_{\mathrm{u}}^{*}(\varphi, \vartheta) \otimes \mathbf{a}_{\mathrm{u}}(\varphi, \vartheta) = \operatorname{vec}(\mathbf{a}_{\mathrm{u}}(\varphi, \vartheta)\mathbf{a}_{\mathrm{u}}(\varphi, \vartheta)^{\mathsf{H}}).$$

Substituting (3.5) with $\mathbf{D}(\varphi, \vartheta, \boldsymbol{\delta}) = \operatorname{diag}(\mathbf{d}(\varphi, \vartheta, \boldsymbol{\delta}))$, we obtain

$$\begin{aligned}
\mathbf{a}_{\mathrm{u,co}}(\varphi, \vartheta) &= \operatorname{vec}\big(\mathbf{D}(\varphi, \vartheta, \boldsymbol{\delta})\mathbf{a}_{\mathrm{p}}(\varphi, \vartheta)\mathbf{a}_{\mathrm{p}}(\varphi, \vartheta)^{\mathsf{H}}\mathbf{D}(\varphi, \vartheta, \boldsymbol{\delta})\big) \\
&= \left(\mathbf{D}(\varphi, \vartheta, \boldsymbol{\delta}) \otimes \mathbf{D}(\varphi, \vartheta, \boldsymbol{\delta})\right)\operatorname{vec}\big(\mathbf{a}_{\mathrm{p}}(\varphi, \vartheta)\mathbf{a}_{\mathrm{p}}(\varphi, \vartheta)^{\mathsf{H}}\big) \\
&= \left(\mathbf{D}(\varphi, \vartheta, \boldsymbol{\delta}) \otimes \mathbf{D}(\varphi, \vartheta, \boldsymbol{\delta})\right)\mathbf{a}_{\mathrm{p,co}}(\varphi, \vartheta).
\end{aligned}$$

This result shows that each U-probe co-array steering vector is obtained by applying a Kronecker-structured weighting to the corresponding pressure co-array vector. Therefore, the uniaxial U-probe co-array preserves the virtual array geometry of the pressure co-array while incorporating additional direction-dependent weighting determined by the sensor orientations.

Compared to the pressure-only case, the co-array manifold is weighted by the directional response of the particle velocity sensors, resulting in an anisotropic virtual

array. This weighting affects the angular sensitivity, generally improving resolution in the sensor's orientation direction.

Similar to the pressure-only case, if we assign to every index i of $\mathbf{a}_{\mathrm{u,co}}(\varphi,\vartheta)$ a pair (m,n) according to $i=(m-1)M+n$, then the i-th entry of $\mathbf{a}_{\mathrm{u,co}}(\varphi,\vartheta)$ can be written as

$$\begin{aligned}[\mathbf{a}_{\mathrm{u,co}}(\varphi,\vartheta)]_i &= d_m d_n a^*_{\mathrm{p},m}(\varphi,\vartheta) a_{\mathrm{p},n}(\varphi,\vartheta) \\ &= \sin(\vartheta)^2 \cos(\delta_n-\varphi)\cos(\delta_m-\varphi)[\mathbf{a}_{\mathrm{p,co}}(\varphi,\vartheta)]_i, \end{aligned} \tag{3.8}$$

where d_m is the m-th entry of $\boldsymbol{d}(\varphi,\vartheta,\boldsymbol{\delta})$.

The compact form of $[\mathbf{a}_{\mathrm{p,co}}(\varphi,\vartheta)]_i$ that reveals the co-array locations is already given in (3.3), so here we focus on interpreting the gain terms to see a similarity of particle velocity response gains. Applying standard trigonometric identities, the product of $\cos(\delta_n-\varphi)\cos(\delta_m-\varphi)$ can be written using the product-to-sum identity as

$$\cos(\delta_n-\varphi)\cos(\delta_m-\varphi)=\frac{1}{2}\Big[\cos(\delta_n+\delta_m-2\varphi)+\cos(\delta_n-\delta_m)\Big].$$

Then, applying the double-angle identity $\cos(2x)=2\cos^2(x)-1$ with $x=\frac{\delta_n+\delta_m}{2}-\varphi$ gives

$$\cos(\delta_n+\delta_m-2\varphi)=2\cos^2\Big(\frac{\delta_n+\delta_m}{2}-\varphi\Big)-1.$$

Substituting this back, the gain term expressed as

$$\sin^2(\vartheta)\cos(\delta_n-\varphi)\cos(\delta_m-\varphi)=\sin^2(\vartheta)\cos^2\Big(\frac{\delta_n+\delta_m}{2}-\varphi\Big)+\frac{\sin^2(\vartheta)}{2}\Big(\cos(\delta_n-\delta_m)-1\Big).$$

This then can be combined with the $[\mathbf{a}_{\mathrm{p,co}}(\varphi,\vartheta)]_i$ to give the final compact expression for (3.8) that the gain term resembles the one in particle velocity response. With $\delta_{mn}=\frac{\delta_n+\delta_m}{2}$ and $\Delta_{mn}=\delta_n-\delta_m$, this form can be expressed as

$$\begin{aligned}[\mathbf{a}_{\mathrm{u,co}}(\varphi,\vartheta)]_i = \Bigg[\sin^2(\vartheta)\cos^2\Big(\delta_{mn}-\varphi\Big)+\frac{\sin^2(\vartheta)}{2}\Big(\cos(\Delta_{mn})-1\Big)\Bigg]\cdot \\ \exp\left(j\kappa R\zeta_{mn}\sin(\vartheta)\cos(\psi_{mn}-\varphi)\right).\end{aligned} \tag{3.9}$$

This shows again that the co-array consists of multiple concentric circles with radii $R\zeta_{mn}$ and for every constant radius, we obtain different angular positions ψ_{mn}. In contrast to the pressure-only case, the first term forms a virtual second-order directional pattern at the midpoint angle δ_{mn} and carrying full DoA information of the source, while the second term is an azimuth-independent and elevation-scaled geometric bias that affects the overall magnitude of the co-array response. The first term itself is not a particle velocity sensor because no directional information is included. Rather than indicating motion in a specific positive or negative direction, it only represents an axis alignment in the direction of δ_{mn}. It shows how strongly the sources align with δ_{mn}. Examples of a UCA tangential, radial and random U-probe co-array (based on only the first term) are illustrated in Figures 3.2–3.4, respectively.

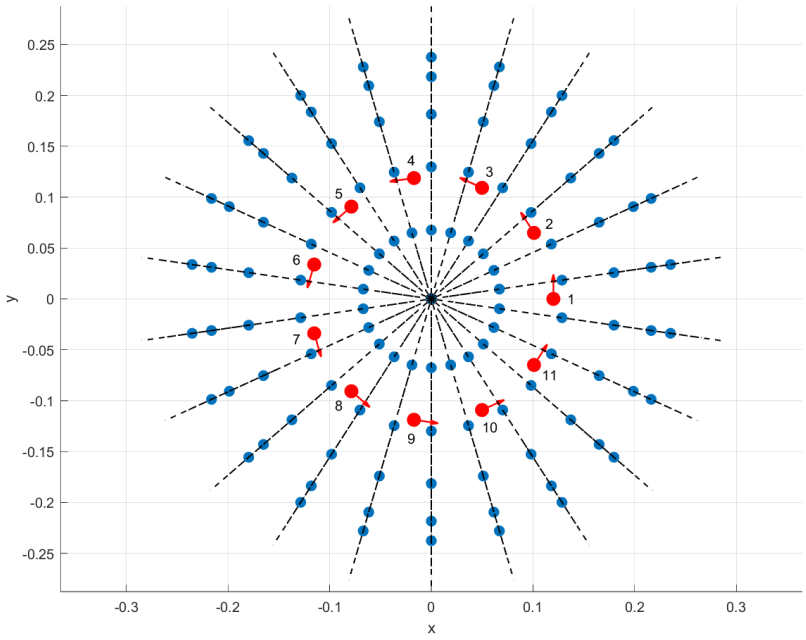


Figure 3.2: Co-array of virtual sensors (blue) with second-order directional pattern (black dashed line) derived from physical UCA sensor positions (red), $M = 11$ and $R = 2.8\lambda$ for tangential U-probe configuration.

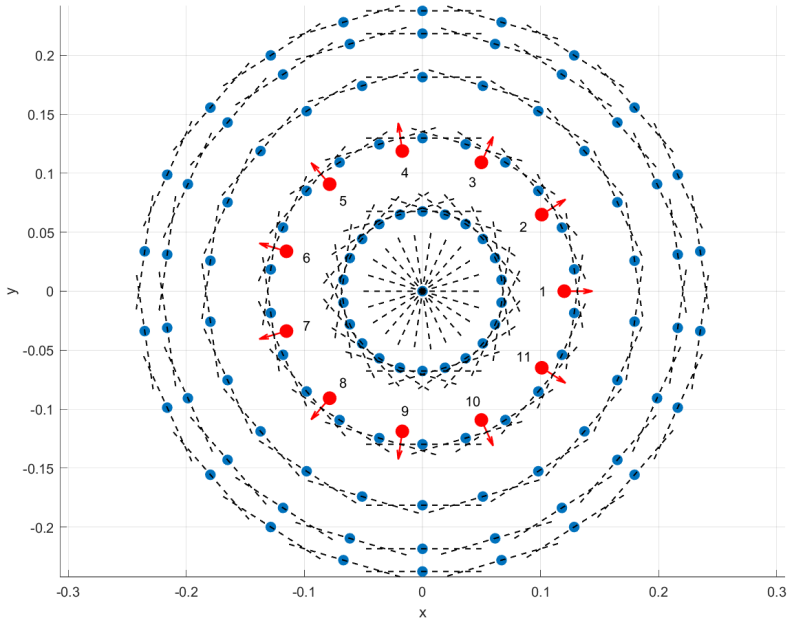


Figure 3.3: Co-array of virtual sensors (blue) with second-order directional pattern (black dashed line) derived from physical UCA sensor positions (red), $M = 11$ and $R = 2.8\lambda$ for radial U-probe configuration.

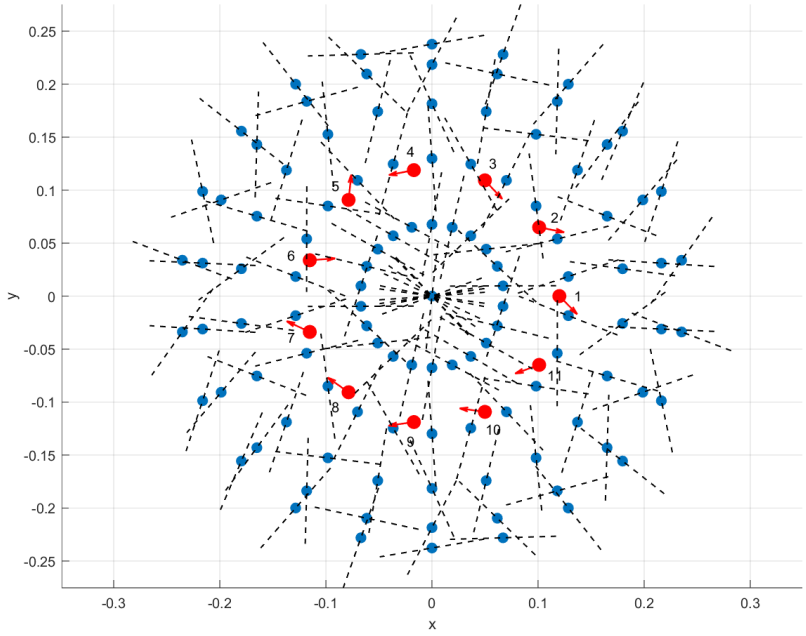


Figure 3.4: Co-array of virtual sensors (blue) with second-order directional pattern (black dashed line) derived from physical UCA sensor positions (red), $M = 11$ and $R = 2.8\lambda$ for random U-probe configuration.

In contrast to the pressure-only case, U-probes exhibit directional responses, introducing an additional dependence on the look direction φ. This directional weighting breaks the symmetry responsible for repeated entries in the pressure co-array, such that different sensor index pairs like (m, m) generally yield distinct co-array responses, even when associated with the same spatial lag.

This can be observed from the co-array response expression (3.9), where the gain term depends explicitly on both the average orientation δ_{mn} and the orientation difference Δ_{mn}. In the special case where $\delta_n = \delta_m$, we have $\Delta_{mn} = 0$, and thus the second term vanishes. Consequently, the directional response reduces to the same angular weighting, meaning that multiple (m, n) pairs yield identical co-array entries. This leads to redundancy at the origin of the co-array.

However, in the design of U-probe arrays on a UCA, sensors are intentionally assigned distinct orientations to exploit directional diversity. Configurations with $\delta_n = \delta_m$ are therefore avoided, as they introduce unnecessary redundancy and reduce the effective degrees of freedom.

Under this assumption, the co-array response vector can be considered non-redundant so that the model in (3.7) can be used directly without the need of a selection matrix $\mathbf{J}$.

This U-probe co-array construction procedure illustrates that, by directly working with the correlations of the particle velocity observations in a UCA, we can increase the number of antennas from M to $M_{\mathrm{co}}^{(\mathrm{u})} = M^2$. Both in the pressure-only and U-probe cases, the array is composed of M physical sensors, and the corresponding co-array constructions expand the virtual aperture by exploiting second-order correlations.

To further increase the co-array dimensionality and improve the available degrees of freedom without doubling the channel counts (PU-probe), we now introduce a special case of U-probe co-array structure, which jointly leverages both types of measurements.

3.2.1 Special Case: Co-Array Structure of Uniaxial U-probe with a Central Pressure Sensor

We now consider a special case of U-probe array, where M uniaxial particle velocity sensors are uniformly placed on a circular ring of radius R, while a single pressure sensor is located at the center of the array. This configuration represents a minimal hybrid setup that augments a U-probe-only UCA with a reference pressure measurement.

In this case, the array consists of $M+1$ measurement channels. We index the central pressure sensor by 0, and the particle velocity sensors by $m = 1, \ldots, M$. The corresponding steering vector can be written as

$$\mathbf{a}_{\mathrm{u}}^{(\mathrm{sp})}(\varphi, \vartheta) = \begin{bmatrix} a_{\mathrm{p},0}(\varphi, \vartheta) \\ a_{\mathrm{u},1}(\varphi, \vartheta) \\ \vdots \\ a_{\mathrm{u},M}(\varphi, \vartheta) \end{bmatrix} \in \mathbb{C}^{(M+1)\times 1}.$$

Since the pressure sensor is located at the origin, its response is independent of the DoA and given by $a_{\mathrm{p},0}(\varphi, \vartheta) = 1$. The particle velocity sensor responses are given by $a_{\mathrm{u},m}(\varphi, \vartheta) = \sin(\vartheta)\cos(\delta_m - \varphi)\exp(j\kappa R\sin(\vartheta)\cos(\phi_m - \varphi))$. Assuming uncorrelated sources, the covariance matrix is

$$\mathbf{R}_{\mathrm{u}}^{(\mathrm{sp})} = \mathbf{A}_{\mathrm{u}}^{(\mathrm{sp})}(\boldsymbol{\varphi}, \boldsymbol{\vartheta})\mathrm{diag}(\boldsymbol{\gamma})\mathbf{A}_{\mathrm{u}}^{(\mathrm{sp})}(\boldsymbol{\varphi}, \boldsymbol{\vartheta})^{\mathsf{H}},$$

and vectorization yields the co-array model

$$\tilde{\mathbf{r}}_{\mathrm{u}}^{(\mathrm{sp})} = \left(\mathbf{A}_{\mathrm{u}}^{(\mathrm{sp})*}(\boldsymbol{\varphi}, \boldsymbol{\vartheta}) \odot \mathbf{A}_{\mathrm{u}}^{(\mathrm{sp})}(\boldsymbol{\varphi}, \boldsymbol{\vartheta})\right)\boldsymbol{\gamma} = \mathbf{A}_{\mathrm{u,co}}^{(\mathrm{sp})}(\boldsymbol{\varphi}, \boldsymbol{\vartheta})\boldsymbol{\gamma},$$

with co-array dimension $(M+1)^2$.

Each entry of the corresponding co-array steering vector is given by

$$[\mathbf{a}_{\mathrm{u,co}}^{(\mathrm{sp})}(\varphi, \vartheta)]_i = \begin{cases} a_{\mathrm{p},m}^*(\varphi, \vartheta)\, a_{\mathrm{u},n}(\varphi, \vartheta), & m = 0,\ n \in \{1, \ldots, M\}, \\ a_{\mathrm{u},m}^*(\varphi, \vartheta)\, a_{\mathrm{u},n}(\varphi, \vartheta), & m, n \in \{1, \ldots, M\}, \\ a_{\mathrm{u},m}^*(\varphi, \vartheta)\, a_{\mathrm{p},n}(\varphi, \vartheta), & m \in \{1, \ldots, M\},\ n = 0, \end{cases}$$

where where we assign to every index i of $\mathbf{a}_{\mathrm{u,co}}^{(\mathrm{sp})}(\varphi, \vartheta)$ a pair (m, n) according to $i = m(M+1) + n + 1$ and $m, n \in \{0, \ldots, M\}$. We distinguish three types of contributions.

Since there is only one pressure sensor available in this array structure, the co-array (p–p) has a single pressure component located at the center obtained from the central pressure sensor

$$a_{\mathrm{p},0}^*(\varphi, \vartheta)a_{\mathrm{p},0}(\varphi, \vartheta) = 1,$$

which corresponds to a zero-lag component without directional dependence.

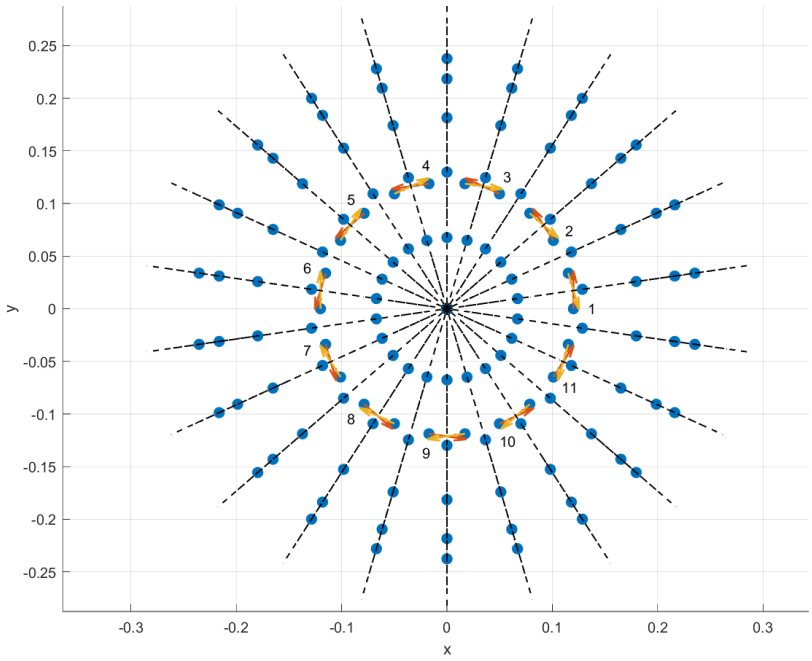


Figure 3.5: Co-array of virtual pressure sensors (blue), virtual sensors with second-order directional pattern (black dashed line) and virtual particle velocity sensors (red and yellow) derived from physical UCA with $M = 11$ and $R = 2.8\lambda$ for tangential U-probe configuration with a central pressure sensor.

For the mixed terms (p–u) & (u–p), we obtain

$$a^*_{\mathrm{p},0}(\varphi,\vartheta)a_{\mathrm{u},m}(\varphi,\vartheta) = \sin(\vartheta)\cos(\delta_m-\varphi)\,\exp(j\kappa R\sin(\vartheta)\cos(\phi_m-\varphi))\,,$$
$$a^*_{\mathrm{u},m}(\varphi,\vartheta)a_{\mathrm{p},0}(\varphi,\vartheta) = \sin(\vartheta)\cos(\delta_m-\varphi)\,\exp(-j\kappa R\sin(\vartheta)\cos(\phi_m-\varphi))\,.$$

Using the identity $\cos(\alpha) = -\cos(\alpha+\pi)$, the latter expression can be rewritten as

$$a^*_{\mathrm{u},m}(\varphi,\vartheta)a_{\mathrm{p},0}(\varphi,\vartheta) = \sin(\vartheta)\cos(\delta_m-\varphi)\,\exp(j\kappa R\sin(\vartheta)\cos(\phi_m+\pi-\varphi))\,.$$

This reveals a clear geometric interpretation that the mixed terms correspond to virtual particle velocity sensors located on the ring of radius R. Specifically, the (p–u) terms produce virtual sensors at angular positions ϕ_m, while the (u–p) terms generate sensors at the antipodal positions $\phi_m + \pi$. In both cases, the directional response is governed by the same orientation δ_m. Hence, each physical U-probe gives rise to a pair of antipodal virtual particle velocity sensors in the co-array.

The (u–u) co-array terms are given by

$$a^*_{\mathrm{u},m}(\varphi,\vartheta)a_{\mathrm{u},n}(\varphi,\vartheta) = \sin^2(\vartheta)\cos(\delta_m-\varphi)\cos(\delta_n-\varphi)\cdot \exp\big(j\kappa R\sin(\vartheta)\big(\cos(\phi_n-\varphi)-\cos(\phi_m-\varphi)\big)\big)\,,$$

which coincides with the U-probe-only co-array derived in the previous section. Consequently, these terms generate the full set of virtual sensor locations on concentric circles characterized by $(R\zeta_{mn}, \psi_{mn})$.

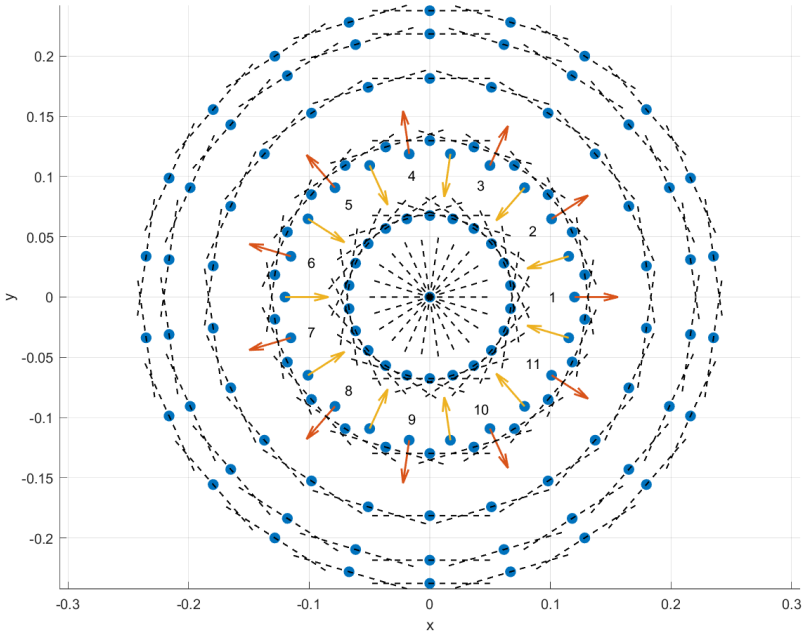


Figure 3.6: Co-array of virtual pressure sensors (blue), virtual sensors with second-order directional pattern (black dashed line) and virtual particle velocity sensors (red and yellow) derived from physical UCA with $M = 11$ and $R = 2.8\lambda$ for radial U-probe configuration with a central pressure sensor.

The resulting co-array largely preserves the virtual geometry of the U-probe-only case, where the (u–u) terms generate the full second-order co-array with M^2 elements distributed over concentric circles. In addition to this dominant structure, the inclusion of the central pressure sensor introduces $2M$ mixed pressure–particle velocity contributions that correspond to first-order directional measurements located on the physical array ring. As shown in Figures 3.5–3.7, these mixed terms appear in antipodal pairs, corresponding to angular positions ϕ_m and $\phi_m + \pi$, and inherit the orientation δ_m of the associated U-probes.

Consequently, the co-array can be interpreted as a uniaxial U-probe co-array augmented with directional measurements at radius R, without modifying the underlying concentric circular structure determined by the (u–u) correlations.

3.3 Uniaxial PU-Probe Co-Array Structure

The PU-probe array consists of co-located pressure and particle velocity measurements at each sensor position. Every particle velocity sensor is uniaxially oriented. As a result, the array response depends on both the azimuth angle φ and the elevation angle ϑ, as well as the sensor orientations $\{\delta_m\}_{m=1}^{M}$. Assuming uncorrelated sources, the covariance matrix of a uniaxial PU-probe UCA with M acoustic vector sensors is given by

$$\mathbf{R}_{\text{pu}} = \mathbb{E}\{\mathbf{x}_{\text{pu}}[l]\mathbf{x}_{\text{pu}}[l]^{\mathsf{H}}\} = \mathbf{A}_{\text{pu}}(\boldsymbol{\varphi}, \boldsymbol{\vartheta})\text{diag}(\boldsymbol{\gamma})\mathbf{A}_{\text{pu}}(\boldsymbol{\varphi}, \boldsymbol{\vartheta})^{\mathsf{H}},$$

where $\boldsymbol{\gamma} = [\gamma_1, \ldots, \gamma_K]^{\top}$ contains the source powers.

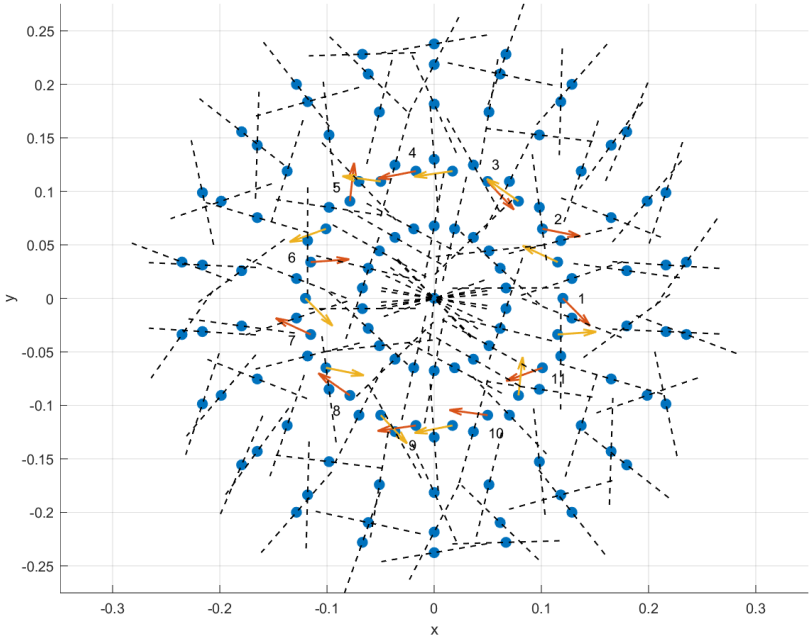


Figure 3.7: Co-array of virtual pressure sensors (blue), virtual sensors with second-order directional pattern (black dashed line) and virtual particle velocity sensors (red and yellow) derived from physical UCA with $M = 11$ and $R = 2.8\lambda$ for random U-probe configuration with a central pressure sensor.

Vectorizing the covariance matrix yields

$$\tilde{\mathbf{r}}_{\mathrm{pu}} = \mathrm{vec}(\mathbf{R}_{\mathrm{pu}}) = \left(\mathbf{A}_{\mathrm{pu}}(\boldsymbol{\varphi}, \boldsymbol{\vartheta})^* \odot \mathbf{A}_{\mathrm{pu}}(\boldsymbol{\varphi}, \boldsymbol{\vartheta})\right) \boldsymbol{\gamma} = \mathbf{A}_{\mathrm{pu,co}}(\boldsymbol{\varphi}, \boldsymbol{\vartheta})\boldsymbol{\gamma},$$

where $\mathbf{A}_{\mathrm{pu,co}}(\boldsymbol{\varphi}, \boldsymbol{\vartheta}) \in \mathbb{C}^{(2M)^2 \times K}$ denotes the PU-probe co-array manifold matrix.

Each column of $\mathbf{A}_{\mathrm{pu,co}}(\boldsymbol{\varphi}, \boldsymbol{\vartheta})$ is given by

$$\mathbf{a}_{\mathrm{pu,co}}(\varphi, \vartheta) = \mathbf{a}^*_{\mathrm{pu}}(\varphi, \vartheta) \otimes \mathbf{a}_{\mathrm{pu}}(\varphi, \vartheta).$$

Based on the interleaved structure of $\mathbf{a}_{\mathrm{pu}}(\varphi, \vartheta)$, we index the measurement channels of $\mathbf{R}_{\mathrm{pu}}$ by $r, c \in \{1, \ldots, 2M\}$, where each index stands for row and column index, respectively. In particular, each index uniquely determines a specific sensor index and a measurement type $t(\cdot) \in \{\mathrm{p}, \mathrm{u}\}$. The sensor index is given by $m(\cdot) = \lceil \cdot/2 \rceil$, while the type is defined such that odd indices correspond to pressure and even indices correspond to particle velocity measurements.

With this indexing, each entry of $\mathbf{a}_{\mathrm{pu,co}}(\varphi, \vartheta)$ can be written as

$$[\mathbf{a}_{\mathrm{pu,co}}(\varphi, \vartheta)]_i = a^*_{t(c),\, m(c)}(\varphi, \vartheta)\, a_{t(r),\, m(r)}(\varphi, \vartheta),$$

where we assign to every index i of $\mathbf{a}_{\mathrm{pu,co}}(\varphi, \vartheta)$ a pair (r, c) according to $i = 2(c-1)M + r$.

Using the pressure and particle velocity steering responses

$$\begin{aligned} a_{\mathrm{p},m}(\varphi, \vartheta) &= \exp(j\kappa R \sin(\vartheta) \cos(\phi_m - \varphi))\,, \\ a_{\mathrm{u},m}(\varphi, \vartheta) &= \sin(\vartheta) \cos(\delta_m - \varphi)\, a_{\mathrm{p},m}(\varphi, \vartheta), \end{aligned}$$

we obtain the following four cases:

$$
\begin{aligned}
&\text{(p–p)} \quad a^{*}_{\mathrm{p},m(c)} a_{\mathrm{p},m(r)} = \exp\big(j\kappa R \sin(\vartheta)\big(\cos(\phi_{m(r)}-\varphi)-\cos(\phi_{m(c)}-\varphi)\big)\big)\,,\\
&\text{(p–u)} \quad a^{*}_{\mathrm{p},m(c)} a_{\mathrm{u},m(r)} = \sin(\vartheta)\cos(\delta_{m(r)}-\varphi)\,\exp\big(j\kappa R \sin(\vartheta)\big(\cos(\phi_{m(r)}-\varphi)-\cos(\phi_{m(c)}-\varphi)\big)\big)\,,\\
&\text{(u–p)} \quad a^{*}_{\mathrm{u},m(c)} a_{\mathrm{p},m(r)} = \sin(\vartheta)\cos(\delta_{m(c)}-\varphi)\,\exp\big(j\kappa R \sin(\vartheta)\big(\cos(\phi_{m(r)}-\varphi)-\cos(\phi_{m(c)}-\varphi)\big)\big)\,,\\
&\text{(u–u)} \quad a^{*}_{\mathrm{u},m(c)} a_{\mathrm{u},m(r)} = \sin^2(\vartheta)\cos(\delta_{m(c)}-\varphi)\cos(\delta_{m(r)}-\varphi)\cdot\\
&\qquad\qquad \exp\big(j\kappa R \sin(\vartheta)\big(\cos(\phi_{m(r)}-\varphi)-\cos(\phi_{m(c)}-\varphi)\big)\big)\,.
\end{aligned}
$$

Thus, all entries of the uniaxial PU-probe co-array manifold share the same phase term as the pressure-only co-array, while the particle velocity components introduce additional direction-dependent weighting factors.

Using the same geometric parametrization as in (3.3), the entries can be compactly written as

$$
[\mathbf{a}_{\mathrm{pu,co}}(\varphi,\vartheta)]_i = \eta_i(\varphi,\vartheta)\,\exp\big(j\kappa R \zeta_{m(c)m(r)} \sin(\vartheta)\cos(\psi_{m(c)m(r)}-\varphi)\big)\,,
$$

where the modulation term $\eta_i(\varphi,\vartheta)$ is given by

$$
\eta_i(\varphi,\vartheta) = \begin{cases} 1, & t(r)=\mathrm{p},\ t(c)=\mathrm{p},\\ \sin(\vartheta)\cos(\delta_{m(r)}-\varphi), & t(r)=\mathrm{p},\ t(c)=\mathrm{u},\\ \sin(\vartheta)\cos(\delta_{m(c)}-\varphi), & t(r)=\mathrm{u},\ t(c)=\mathrm{p},\\ \sin^2(\vartheta)\cos(\delta_{m(c)}-\varphi)\cos(\delta_{m(r)}-\varphi), & t(r)=\mathrm{u},\ t(c)=\mathrm{u}. \end{cases}
$$

Following the same procedure, the PU-probe co-array entries can also be interpreted in terms of concentric circles. In particular, using the geometric parametrization introduced for the pressure-only case, the common phase term depends only on the pair $(m(c),m(r))$ through $\zeta_{m(c)m(r)}$ and $\psi_{m(c)m(r)}$, while the different measurement combinations introduce distinct amplitude modulations.

For the (p–p) case, the expression directly reduces to (3.3), i.e.,

$$
a^{*}_{\mathrm{p},m(c)} a_{\mathrm{p},m(r)} = \exp\big(j\kappa R \zeta_{m(c)m(r)} \sin(\vartheta)\cos(\psi_{m(c)m(r)}-\varphi)\big)\,.
$$

For the (u–u) case, we recover the compact form in (3.9), given by

$$
a^{*}_{\mathrm{u},m(c)} a_{\mathrm{u},m(r)} = \left[\sin^2(\vartheta)\cos^2\Big(\delta_{m(c)m(r)}-\varphi\Big) + \frac{\sin^2(\vartheta)}{2}\Big(\cos(\Delta_{m(c)m(r)})-1\Big)\right]\cdot \exp\big(j\kappa R \zeta_{m(c)m(r)} \sin(\vartheta)\cos(\psi_{m(c)m(r)}-\varphi)\big)\,.
$$

The mixed pressure–particle velocity terms can be written in a similar geometric form. Specifically, the (p–u) and (u–p) components become

$$
\begin{aligned}
a^{*}_{\mathrm{p},m(c)} a_{\mathrm{u},m(r)} &= \sin(\vartheta)\cos(\delta_{m(c)}-\varphi)\,\exp\big(j\kappa R \zeta_{m(c)m(r)} \sin(\vartheta)\cos(\psi_{m(c)m(r)}-\varphi)\big)\\
a^{*}_{\mathrm{u},m(c)} a_{\mathrm{p},m(r)} &= \sin(\vartheta)\cos(\delta_{m(r)}-\varphi)\,\exp\big(j\kappa R \zeta_{m(c)m(r)} \sin(\vartheta)\cos(\psi_{m(c)m(r)}-\varphi)\big)
\end{aligned}
$$

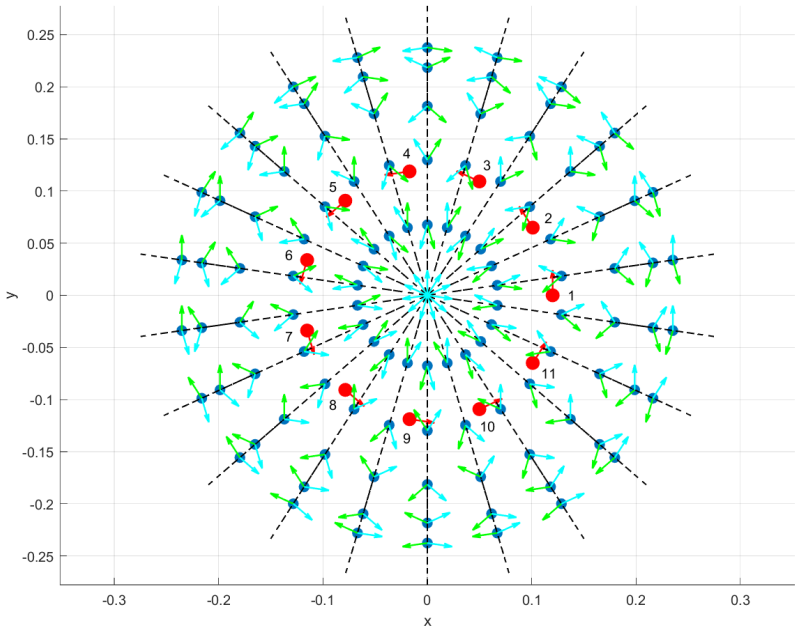


Figure 3.8: Co-array of virtual pressure sensors (blue), virtual sensors with second-order directional pattern (black dashed line) and virtual particle velocity sensors (cyan and green) derived from physical UCA sensor positions (red), $M = 11$ and $R = 2.8\lambda$ for tangential PU-probe configuration.

Hence, all four cases share the same set of virtual co-array locations defined by $(R\zeta_{m(c)m(r)}, \psi_{m(c)m(r)})$, corresponding to concentric circles as in the pressure-only case, while the particle velocity measurements introduce additional direction-dependent weighting that modulates the amplitude of each virtual sensor.

In the uniaxial PU-probe case, the co-array consists not only of the (p–p) and (u–u) contributions, but also includes the mixed pressure and particle velocity (p–u) and (u–p) terms. These mixed terms resemble the particle velocity response in the co-array and effectively introduce additional directional sensitivity. Specifically, for each virtual sensor location, they yield two particle velocity components oriented according to the corresponding physical sensor directions in the UCA.

As a result, every virtual co-array position is associated with a pressure measurement, directional particle velocity measurements, and a (u–u) contribution, where the leading term exhibits a second-order directional pattern that reflects how strongly incoming waves align with the virtual sensor orientation axis. This combination enriches the spatial selectivity of the co-array by embedding both isotropic and directional responses at each virtual location. Examples of a UCA with tangential, radial, and random PU-probe configurations are illustrated in Figures 3.8–3.10, respectively.

This uniaxial PU-probe co-array construction procedure illustrates that, by directly working with the correlations of the observations in a UCA, we can increase the number of measurements from $2M$ to $M_{\text{co}}^{(\text{pu})} = (2M)^2$.

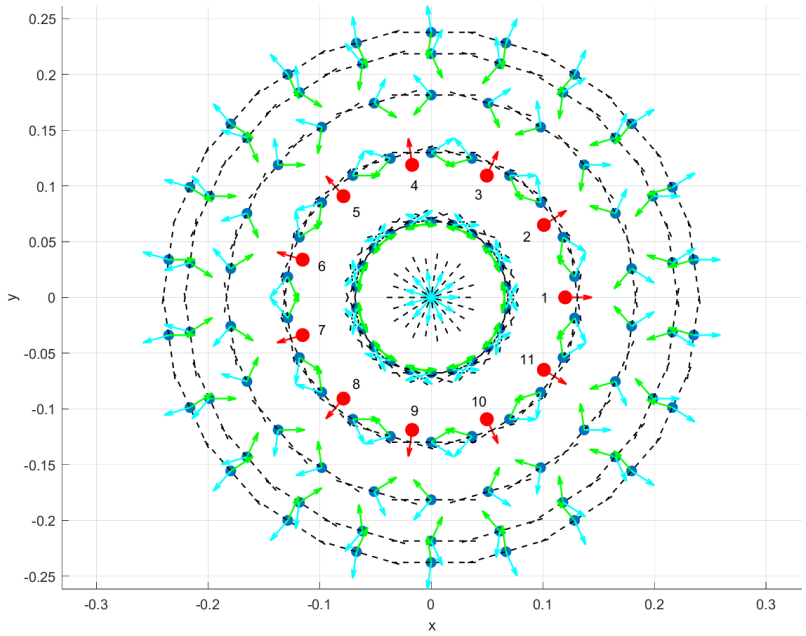


Figure 3.9: Co-array of virtual pressure sensors (blue), virtual sensors with second-order directional pattern (black dashed line) and virtual particle velocity sensors (cyan and green) derived from physical UCA sensor positions (red), $M = 11$ and $R = 2.8\lambda$ for radial PU-probe configuration.

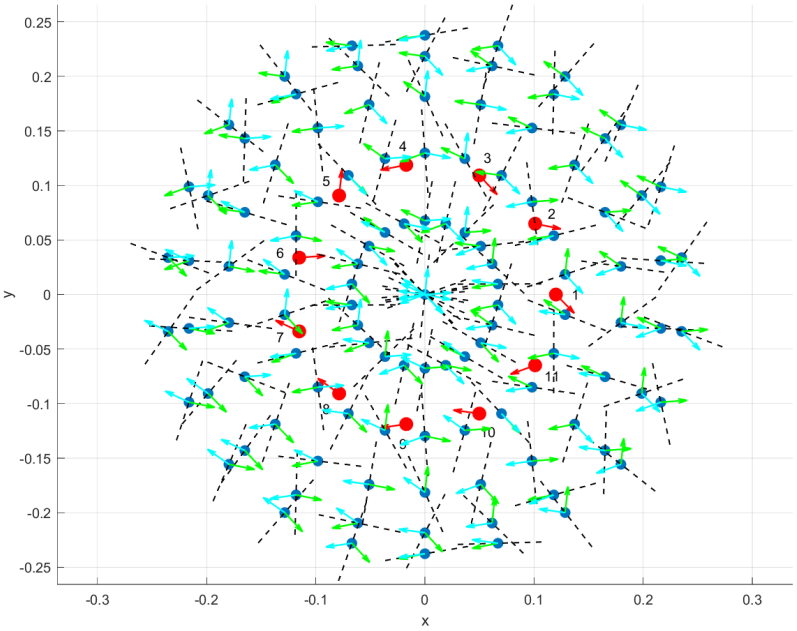


Figure 3.10: Co-array of virtual pressure sensors (blue), virtual sensors with second-order directional pattern (black dashed line) and virtual particle velocity sensors (cyan and green) derived from physical UCA sensor positions (red), $M = 11$ and $R = 2.8\lambda$ for random PU-probe configuration.

3.4 Conclusion

In this chapter, the co-array structures of pressure-only, uniaxial U-probe, and uniaxial PU-probe UCAs were derived and analyzed. By vectorizing the covariance matrix, all considered array configurations were shown to generate virtual co-arrays with increased aperture and degrees of freedom. While the pressure-only case yields a concentric circular co-array structure, the U-probe and PU-probe configurations additionally introduce direction-dependent weighting. The weighting introduced by the U-probe configuration depends on the alignment between the incoming wavefield and the virtual sensor orientation axis δ_{mn}. In the PU-probe case, the additional mixed pressure–particle velocity terms further associate each co-array location with virtual particle velocity components.

However, although the pressure-only, uniaxial U-probe, and uniaxial PU-probe co-arrays increase the effective aperture and degrees of freedom, their virtual geometries still consist of multiple concentric circles and therefore do not possess the shift-invariance Vandermonde structure required by high-resolution gridless subspace methods. To address this, we transform the co-array of the UCA to a virtual ULA. This is discussed in detail in the next chapter.

From the UCA Co-Array to a Virtual ULA

4

Despite the advantages of UCA co-array, such as enhanced aperture and uniform 360° spatial coverage, its geometry still consists of multiple concentric circles and therefore does not exhibit the shift-invariance Vandermonde structure naturally present in ULAs. As a result, high-resolution gridless subspace-based DoA estimation techniques, such as ESPRIT and Root-MUSIC, cannot be directly applied in the UCA co-array domain.

To address this challenge, the UCA co-array manifold can be transformed into an equivalent virtual ULA representation. Among the different available approaches, we focus on the Jacobi–Anger expansion, which provides a harmonic representation of the UCA co-array response.

In this chapter, we develop this transformation in detail, beginning with the pressure sensor co-array and extending the formulation to the uniaxial U-probe and uniaxial PU-probe cases.

4.1 Transformation of UCA Pressure Co-Array

There exist several approaches to transform an irregular array geometry into an equivalent virtual ULA. In this work, we adopt a harmonic-domain approach based on the Jacobi–Anger expansion. Unlike conventional techniques that directly map the physical array manifold, we operate in the co-array domain, which effectively enlarges the array aperture by providing a higher number of virtual sensors.

The Jacobi–Anger identity states that for any real-valued scalar z and angle θ, the following expansion holds:

$$\exp(jz\cos\theta) = \sum_{q=-\infty}^{\infty} j^q J_q(z) e^{jq\theta},$$

where $J_q(\cdot)$ denotes the Bessel function of the first kind of order q.

Assuming the elevation angle $\vartheta = \pi/2$, the transformation becomes independent of the elevation. This assumption is made because, otherwise, the elevation and azimuth are not separable with this identity, and we cannot obtain a clean virtual ULA structure.

4.1.1 Transformation via Non-Redundant Co-Array Representation

As discussed in Section 3.1.1, we denote the non-redundant co-array steering vector as $\mathbf{b}_{\mathrm{p}}(\varphi)$, which is given by

$$[\mathbf{b}_{\mathrm{p}}(\varphi)]_{f(i)} = \exp(j\kappa R\zeta_{mn}\cos(\psi_{mn} - \varphi))\,.$$

Here, for $i = (m-1)M + n$, the function $f(i)$ maps the sensor pair (m, n) to the corresponding row index of $\mathbf{b}_{\mathrm{p}}(\varphi)$, i.e., $[\mathbf{b}_{\mathrm{p}}(\varphi)]_{f(i)} = [\mathbf{a}_{\mathrm{p,co}}(\varphi)]_i$.

Then, the Jacobi-Anger identity can be applied to this co-array steering vector. In particular, the $f(i)$-th entry of $\mathbf{b}_{\mathrm{p}}(\varphi)$ can be expressed in the form $\exp(jz\cos\theta)$ by identifying $z = \kappa R\zeta_{mn}$ and $\theta = \psi_{mn} - \varphi$. Using the Jacobi–Anger expansion, we obtain

$$\begin{aligned}[\mathbf{b}_{\mathrm{p}}(\varphi)]_{f(i)} &= \sum_{q=-\infty}^{\infty} \left[j^q J_q(\kappa R\zeta_{mn}) e^{jq\psi_{mn}}\right] e^{-jq\varphi} \\ &= \sum_{q=-\infty}^{\infty} g^{(\mathrm{p})}_{b,f(i),q}\, e^{-jq\varphi},\end{aligned}$$

where the coefficients are defined as

$$g^{(\mathrm{p})}_{b,f(i),q} = j^q\, J_q(\kappa R\zeta_{mn})\, e^{jq\psi_{mn}}. \tag{4.1}$$

By stacking all $M^{(\mathrm{p})}_{b,\mathrm{co}}$ entries, the non-redundant co-array response vector can be written compactly as

$$\mathbf{b}_{\mathrm{p}}(\varphi) = \sum_{q=-\infty}^{\infty} \mathbf{g}^{(\mathrm{p})}_{b,q}\, e^{-jq\varphi},$$

where $\mathbf{g}^{(\mathrm{p})}_{b,q} = [g^{(\mathrm{p})}_{b,1,q}, g^{(\mathrm{p})}_{b,2,q}, \ldots, g^{(\mathrm{p})}_{b,M^{(\mathrm{p})}_{b,\mathrm{co}},q}]^\top \in \mathbb{C}^{M^{(\mathrm{p})}_{b,\mathrm{co}}}$. This formulation reveals an implicit virtual ULA structure in the harmonic domain. Although the expansion is, in principle, infinite-dimensional, it can be truncated in practice. This is justified by the rapid decay of the Bessel functions $J_q(\kappa R\zeta_{mn})$ as $|q|$ increases, rendering higher-order harmonics negligible.

By truncating the expansion to $|q| \le Q_{\mathrm{p}}$, we define the virtual ULA steering vector as

$$\mathbf{v}_{Q_{\mathrm{p}}}(\varphi) = [e^{jQ_{\mathrm{p}}\varphi}, \ldots, e^{j\varphi}, 1, e^{-j\varphi}, \ldots, e^{-jQ_{\mathrm{p}}\varphi}]^\top, \tag{4.2}$$

and obtain the approximation

$$\mathbf{b}_{\mathrm{p}}(\varphi) \approx \sum_{q=-Q_{\mathrm{p}}}^{Q_{\mathrm{p}}} \mathbf{g}^{(\mathrm{p})}_{b,q}\, e^{-jq\varphi} = \mathbf{G}^{(\mathrm{p})}_{b,Q_p}\, \mathbf{v}_{Q_{\mathrm{p}}}(\varphi),$$

where $\mathbf{G}^{(\mathrm{p})}_{b,Q_{\mathrm{p}}} = \left[\, \mathbf{g}^{(\mathrm{p})}_{b,-Q_{\mathrm{p}}}, \ldots, \mathbf{g}^{(\mathrm{p})}_{b,0}, \ldots, \mathbf{g}^{(\mathrm{p})}_{b,Q_p} \,\right] \in \mathbb{C}^{M^{(\mathrm{p})}_{b,\mathrm{co}} \times (2Q_p+1)}$. The truncation level Q_{p} determines the trade-off between approximation accuracy and numerical stability. The harmonic truncation order for the co-array in Figure 3.1 is selected as $Q_{\mathrm{p}} = 40$ based on the observed decay behavior of the coefficients defined in (4.1). This selection ensures that negligible harmonic components are discarded while preserving the essential structure of the signal. The magnitude plot of the decaying profiles are shown in Figure 4.1.

Under this truncated model, the array response matrix for multiple sources can be written as

$$\mathbf{B}_{\mathrm{p}}(\boldsymbol{\varphi}) = \mathbf{G}^{(\mathrm{p})}_{b,Q_{\mathrm{p}}} \mathbf{V}_{Q_{\mathrm{p}}}(\boldsymbol{\varphi}),$$

where $\mathbf{V}_{Q_{\mathrm{p}}}(\boldsymbol{\varphi}) = [\mathbf{v}_{Q_{\mathrm{p}}}(\varphi_1), \ldots, \mathbf{v}_{Q_{\mathrm{p}}}(\varphi_K)] \in \mathbb{C}^{(2Q_{\mathrm{p}}+1)\times K}$.

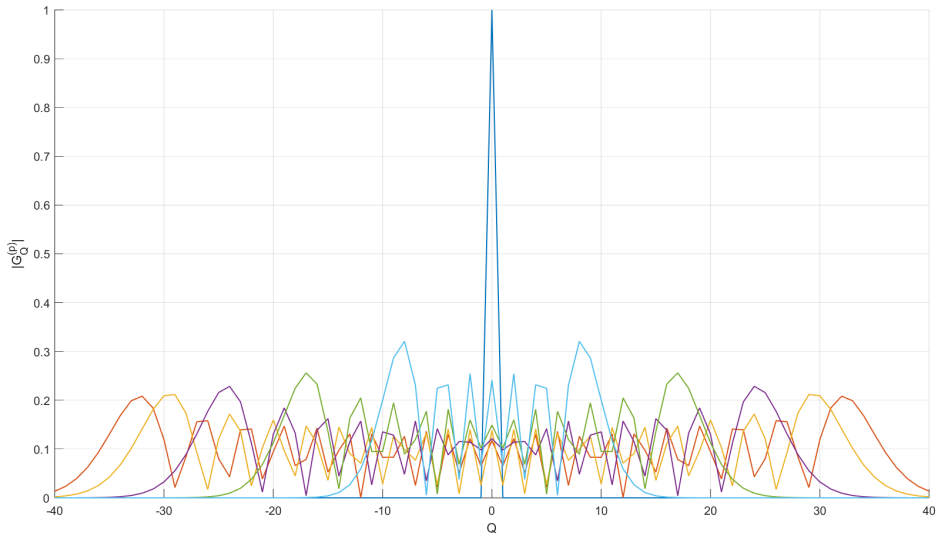


Figure 4.1: Magnitude of the $\mathbf{G}^{(\mathrm{p})}_{t,Q_\mathrm{p}}$, $t \in \{a, b\}$ coefficients as a function of harmonic order q for all unique sensor-pair differences in a UCA with $M = 11$ and $R = 2.8\lambda$. The absolute values depend only on ζ_{mn}, resulting in six distinct decay profiles.

Substituting this into the data model in (3.4) yields

$$\mathbf{r}_\mathrm{p} = \mathbf{B}_\mathrm{p}(\boldsymbol{\varphi})\boldsymbol{\gamma} = \mathbf{G}^{(\mathrm{p})}_{b,Q_p}\mathbf{V}_{Q_\mathrm{p}}(\boldsymbol{\varphi})\boldsymbol{\gamma} = \mathbf{G}^{(\mathrm{p})}_{b,Q_\mathrm{p}}\mathbf{c},$$

where the vector $\mathbf{c}_{Q_\mathrm{p}} = \mathbf{V}_{Q_\mathrm{p}}(\boldsymbol{\varphi})\boldsymbol{\gamma}$ represents the harmonic coefficients, with entries

$$c_q = \sum_{k=1}^{K} \gamma_k e^{-jq\varphi_k}. \tag{4.3}$$

While the above formulation leverages the non-redundant co-array representation to achieve a compact model with increased degrees of freedom, it discards repeated co-array entries corresponding to identical spatial lags. In the following subsection, we consider an alternative formulation in which all co-array entries are retained, leading to a redundant representation that is particularly advantageous in finite-sample scenarios where a covariance matrix is constructed after spatial smoothing.

4.1.2 Transformation via Redundant Co-Array Representation

In this subsection, we retain all entries of the co-array response vector, including redundant elements corresponding to identical sensor-pair differences. Accordingly, we denote the co-array steering vector as $\mathbf{a}_\mathrm{p}(\varphi)$, whose i-th entry is given by

$$[\mathbf{a}_\mathrm{p}(\varphi)]_i = \exp(j\kappa R\zeta_{mn}\cos(\psi_{mn} - \varphi)).$$

Following the same approach as in the non-redundant case, the Jacobi–Anger identity can be applied. By identifying $z = \kappa R\zeta_{mn}$ and $\theta = \psi_{mn} - \varphi$, the i-th entry can be

expanded as

$$[\mathbf{a}_{\mathrm{p}}(\varphi)]_i = \sum_{q=-\infty}^{\infty} \left[j^q J_q(\kappa R \zeta_{mn}) e^{jq\psi_{mn}} \right] e^{-jq\varphi} = \sum_{q=-\infty}^{\infty} g_{a,i,q}^{(\mathrm{p})}\, e^{-jq\varphi},$$

where the coefficients are defined as $g_{a,i,q}^{(\mathrm{p})} = j^q\, J_q(\kappa R \zeta_{mn})\, e^{jq\psi_{mn}}$. By stacking all $M_{a,\mathrm{co}}^{(\mathrm{p})} = M^2$ entries, the redundant co-array response vector can be written as

$$\mathbf{a}_{\mathrm{p}}(\varphi) = \sum_{q=-\infty}^{\infty} \mathbf{g}_{a,q}^{(\mathrm{p})}\, e^{-jq\varphi},$$

where $\mathbf{g}_{a,q}^{(\mathrm{p})} = [g_{a,1,q}^{(\mathrm{p})}, g_{a,2,q}^{(\mathrm{p})}, \ldots, g_{a,M_{a,\mathrm{co}}^{(\mathrm{p})},q}^{(\mathrm{p})}]^\top \in \mathbb{C}^{M_{a,\mathrm{co}}^{(\mathrm{p})}}$. As in the non-redundant case, this formulation reveals an implicit virtual ULA structure in the harmonic domain. The infinite-dimensional expansion can again be truncated by exploiting the decay of the Bessel functions. By truncating to $|q| \leq Q_{\mathrm{p}}$, we obtain

$$\mathbf{a}_{\mathrm{p}}(\varphi) \approx \sum_{q=-Q_{\mathrm{p}}}^{Q_{\mathrm{p}}} \mathbf{g}_{a,q}^{(\mathrm{p})}\, e^{-jq\varphi} = \mathbf{G}_{a,Q_p}^{(\mathrm{p})}\, \mathbf{v}_{Q_{\mathrm{p}}}(\varphi),$$

where $\mathbf{G}_{a,Q_p}^{(\mathrm{p})} = \left[\mathbf{g}_{a,-Q_{\mathrm{p}}}^{(\mathrm{p})}, \ldots, \mathbf{g}_{a,0}^{(\mathrm{p})}, \ldots, \mathbf{g}_{a,Q_{\mathrm{p}}}^{(\mathrm{p})} \right] \in \mathbb{C}^{M_{a,\mathrm{co}}^{(\mathrm{p})} \times (2Q_{\mathrm{p}}+1)}$. For multiple sources, the array response matrix becomes

$$\mathbf{A}_{\mathrm{p}}(\boldsymbol{\varphi}) = \mathbf{G}_{a,Q_p}^{(\mathrm{p})} \mathbf{V}_{Q_{\mathrm{p}}}(\boldsymbol{\varphi}).$$

Substituting into the data model yields

$$\tilde{\mathbf{r}}_{\mathrm{p}} = \mathbf{A}_{\mathrm{p}}(\boldsymbol{\varphi})\boldsymbol{\gamma} = \mathbf{G}_{a,Q_p}^{(\mathrm{p})} \mathbf{V}_{Q_{\mathrm{p}}}(\boldsymbol{\varphi})\boldsymbol{\gamma} = \mathbf{G}_{a,Q_{\mathrm{p}}}^{(\mathrm{p})} \mathbf{c}_{Q_{\mathrm{p}}}.$$

Compared to the non-redundant formulation, this representation preserves all $M_{a,\mathrm{co}}^{(\mathrm{p})} = M^2$ co-array entries.

4.2 Transformation of UCA Uniaxial U-Probe Co-Array

We now extend the harmonic-domain transformation to the uniaxial U-probe co-array. Starting from (3.9), and assuming sources lie in the horizontal plane ($\vartheta = \pi/2$), the i-th entry simplifies to

$$[\mathbf{a}_{\mathrm{u,co}}(\varphi)]_i = \left[\cos^2\Big(\delta_{mn} - \varphi\Big) + \frac{1}{2}\Big(\cos(\Delta_{mn}) - 1 \Big) \right] \exp(j\kappa R \zeta_{mn} \cos(\psi_{mn} - \varphi)).$$

To obtain a harmonic representation, we first rewrite the angular prefactor such that its dependence on φ appears explicitly in complex exponential form. Using the identity $\cos^2(x) = \frac{1+\cos(2x)}{2}$, we obtain

$$\begin{aligned}\cos^2(\delta_{mn} - \varphi) &= \frac{1}{2} + \frac{1}{2}\cos\big(2(\delta_{mn} - \varphi)\big) \\ &= \frac{1}{2} + \frac{1}{4}\left(e^{j2(\delta_{mn}-\varphi)} + e^{-j2(\delta_{mn}-\varphi)}\right).\end{aligned}$$

Substituting this into the prefactor yields

$$\begin{aligned}&\cos^2(\delta_{mn} - \varphi) + \frac{1}{2}(\cos\Delta_{mn} - 1) \\ &= \frac{1}{2}\cos\Delta_{mn} + \frac{1}{4}e^{j2\delta_{mn}}e^{-j2\varphi} + \frac{1}{4}e^{-j2\delta_{mn}}e^{j2\varphi}.\end{aligned}$$

This expression is now explicitly written as a sum of harmonics in φ with orders $q = 0, \pm 2$.

Next, we apply the Jacobi–Anger expansion to the exponential term:

$$\exp(j\kappa R\zeta_{mn}\cos(\psi_{mn} - \varphi)) = \sum_{q=-\infty}^{\infty} j^q J_q(\kappa R\zeta_{mn})e^{jq\psi_{mn}}e^{-jq\varphi}.$$

Combining the prefactor expansion with the above expression results in a convolution in the harmonic domain. Specifically, the i-th entry becomes

$$[\mathbf{a}_{\mathrm{u,co}}(\varphi)]_i = \sum_{q=-\infty}^{\infty} g_{i,q}^{(u)}\, e^{-jq\varphi},$$

where the coefficients $g_{i,q}^{(\mathrm{u})}$ are independent of φ and given by

$$\begin{aligned}g_{i,q}^{(\mathrm{u})} &= \frac{1}{2}\cos(\Delta_{mn})\, j^q J_q(kR\zeta_{mn})e^{jq\psi_{mn}} \\ &\quad + \frac{1}{4}e^{j2\delta_{mn}}\, j^{q-2}J_{q-2}(kR\zeta_{mn})e^{j(q-2)\psi_{mn}} \\ &\quad + \frac{1}{4}e^{-j2\delta_{mn}}\, j^{q+2}J_{q+2}(kR\zeta_{mn})e^{j(q+2)\psi_{mn}}. \qquad (4.4)\end{aligned}$$

Stacking all $M_{\mathrm{co}}^{(\mathrm{u})}$ entries, the uniaxial U-probe co-array response vector admits the harmonic representation

$$\mathbf{a}_{\mathrm{u,co}}(\varphi) = \sum_{q=-\infty}^{\infty} \mathbf{g}_q^{(\mathrm{u})}\, e^{-jq\varphi},$$

where $\mathbf{g}_q^{(\mathrm{u})} = [g_{1,q}^{(\mathrm{u})}, \ldots, g_{M_{\mathrm{co}}^{(\mathrm{u})},q}^{(\mathrm{u})}]^T \in \mathbb{C}^{M_{\mathrm{co}}^{(\mathrm{u})}}$.

As in the pressure case, this representation reveals an implicit virtual ULA structure in the harmonic domain. By truncating the expansion to $|q| \le Q_{\mathrm{u}}$, we obtain the approximation

$$\mathbf{a}_{\mathrm{u,co}}(\varphi) \approx \sum_{q=-Q_{\mathrm{u}}}^{Q_{\mathrm{u}}} \mathbf{g}_q^{(\mathrm{u})}\, e^{-jq\varphi} = \mathbf{G}_{Q_{\mathrm{u}}}^{(\mathrm{u})}\mathbf{v}_{Q_{\mathrm{u}}}(\varphi), \qquad (4.5)$$

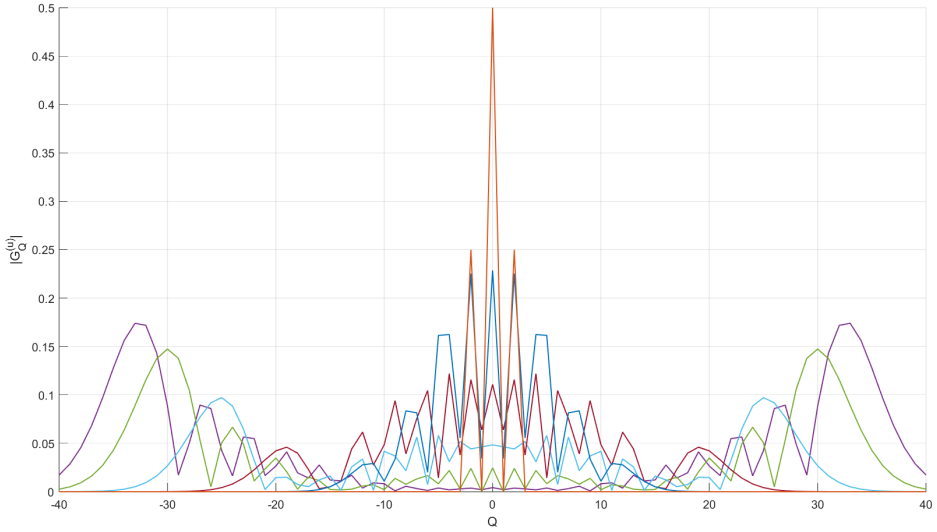


Figure 4.2: Magnitude of the $\mathbf{G}_{Q_\mathrm{u}}^{(\mathrm{u})}$ coefficients as a function of harmonic order q for all unique tangential sensor-pair differences in a UCA with $M = 11$ and $R = 2.8\lambda$. The absolute values depend only on ζ_{mn}, resulting in six distinct decay profiles.

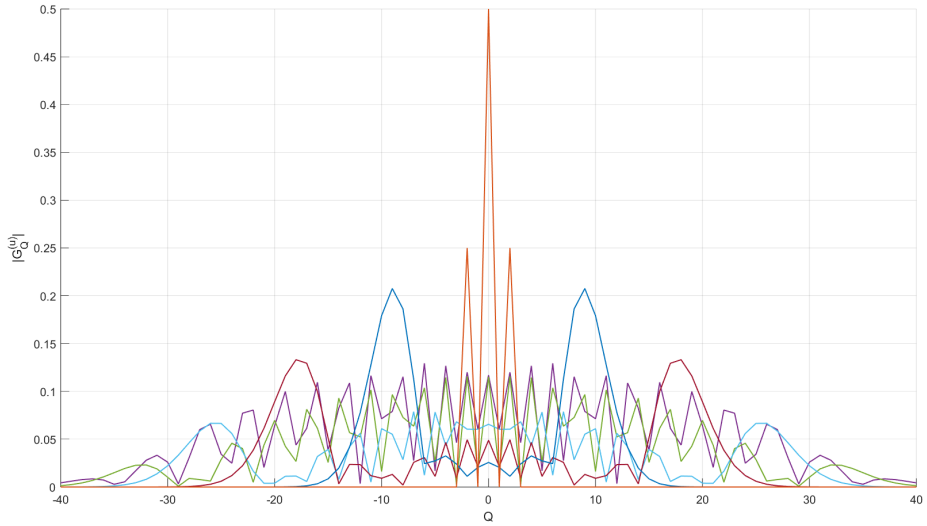


Figure 4.3: Magnitude of the $\mathbf{G}_{Q_\mathrm{u}}^{(\mathrm{u})}$ coefficients as a function of harmonic order q for all unique radial sensor-pair differences in a UCA with $M = 11$ and $R = 2.8\lambda$. The absolute values depend only on ζ_{mn}, resulting in six distinct decay profiles.

where $\mathbf{G}_{Q_\mathrm{u}}^{(u)} = [\mathbf{g}_{-Q_\mathrm{u}}^{(\mathrm{u})}, \ldots, \mathbf{g}_{Q_\mathrm{u}}^{(\mathrm{u})}] \in \mathbb{C}^{M_{\mathrm{co}}^{(\mathrm{u})} \times (2Q_\mathrm{u}+1)}$ and $\mathbf{v}_{Q_\mathrm{u}}(\varphi)$ is the virtual ULA steering vector where the structure is defined in (4.2). For the pressure case, the magnitude of the $\mathbf{G}_{t,Q_\mathrm{p}}^{(\mathrm{p})}$, $t \in \{a, b\}$ depends solely on ζ_{mn}. In contrast, for the U-probe case, the magnitude $\mathbf{G}_{Q_\mathrm{u}}^{(\mathrm{u})}$ depends on both $\cos(\Delta_{mn})$ and ζ_{mn}. For tangential and radial sensor orientations, there exist six distinct values of $\cos(\Delta_{mn})$, each corresponding to a unique ζ_{mn} for $M = 11$. As a result, the magnitude exhibits again six distinct decaying profiles,



Figure 4.4: Magnitude of the $\mathbf{G}_{Q_\mathrm{u}}^{(\mathrm{u})}$ coefficients as a function of harmonic order q for all unique random sensor-pair differences in a UCA with $M = 11$ and $R = 2.8\lambda$.

which can be seen in Figures 4.2 and 4.3. However, for randomly oriented sensors, this property no longer holds. In this case, the number of unique orientation differences Δ_{mn} is not equal to the number of unique sensor positions ζ_{mn} which is equal to six as before for $M = 11$. The magnitude plot of the decaying profiles for random sensor orientation is shown in Figure 4.4.

The formulation (4.5) shows that, despite the additional angular weighting introduced by U-probe measurements, the co-array can still be mapped to a virtual ULA. The main difference compared to the pressure case lies in the harmonic coupling across neighboring orders due to the ± 2 angular components in the prefactor.

Then the array response matrix for multiple sources can be written as

$$\mathbf{A}_{\mathrm{u,co}}(\boldsymbol{\varphi}) = \mathbf{G}_{Q_\mathrm{u}}^{(\mathrm{u})} \mathbf{V}_{Q_\mathrm{u}}(\boldsymbol{\varphi}),$$

where $\mathbf{V}_{Q_\mathrm{u}}(\boldsymbol{\varphi}) = [\mathbf{v}_{Q_\mathrm{u}}(\varphi_1), \ldots, \mathbf{v}_{Q_\mathrm{u}}(\varphi_K)] \in \mathbb{C}^{(2Q_\mathrm{u}+1)\times K}$.

Substituting this into the data model in (3.7) yields

$$\tilde{\mathbf{r}}_\mathrm{u} = \mathbf{A}_{\mathrm{u,co}}(\boldsymbol{\varphi})\boldsymbol{\gamma} = \mathbf{G}_{Q_\mathrm{u}}^{(\mathrm{u})} \mathbf{V}_{Q_\mathrm{u}}(\boldsymbol{\varphi})\boldsymbol{\gamma} = \mathbf{G}_{Q_\mathrm{u}}^{(\mathrm{u})} \mathbf{c}_{Q_\mathrm{u}},$$

where the vector $\mathbf{c}_{Q_\mathrm{u}}$ represents the harmonic coefficients with entries (4.3).

The harmonic truncation order Q_u for all of the particle velocity co-arrays in Figures 3.2–3.4 is selected as $Q_\mathrm{u} = 40$ based on the observed decay behavior of the coefficients defined in (4.4). This selection again ensures that minor harmonic elements are filtered out without affecting the core structure of the signal.

4.2.1 Special Case: Transformation of UCA Uniaxial U-probe with a Central Pressure Sensor

We now consider the harmonic-domain representation for the special case introduced previously, where M uniaxial U-probes are placed on a circular ring and a single pressure

sensor is located at the center of the array. In this configuration, the co-array consists of $(M+1)^2$ entries, which can be grouped into three contributions namely a single (p–p) term, $2M$ mixed (p–u) & (u–p) terms, and M^2 (u–u) terms.

We assume $\vartheta = \pi/2$. The pressure response at the center is to $a_{\mathrm{p},0}(\varphi) = 1$. The co-array entries cannot be expressed using a single unified spatial mapping of pressure-only case, since the exponential terms differ between the mixed contributions. Instead, each entry is written as

$$[\mathbf{a}^{(\mathrm{sp})}_{\mathrm{u,co}}(\varphi)]_i = \eta^{(\mathrm{sp})}_i(\varphi)\, \exp\big(j\kappa R\zeta^{(\mathrm{sp})}_{mn} \cos(\psi^{(\mathrm{sp})}_{mn} - \varphi)\big)\,,$$

where both the modulation term $\eta^{(\mathrm{sp})}_i(\varphi)$ and the geometry parameters $(\zeta^{(\mathrm{sp})}_{mn}, \psi^{(\mathrm{sp})}_{mn})$ depend on the correlation type, with $i = m(M+1)+n+1$ and $m, n \in \{0, \ldots, M\}$. For $m, n \in \{1, \ldots, M\}$, $\zeta^{(\mathrm{sp})}_{mn} = \zeta_{mn}$ and $\psi^{(\mathrm{sp})}_{mn} = \psi_{mn}$ from (3.3). The detailed explanation for either one of (m, n) or both being 0 is given below.

The (p–p) contribution corresponds to the trivial case

$$\eta^{(\mathrm{sp})}_0 = 1, \qquad \zeta^{(\mathrm{sp})}_{00} = 0,$$

which yields a constant term without angular dependence. Combining this with the Jacobi–Anger expansion yields

$$[\mathbf{a}^{(\mathrm{sp})}_{\mathrm{u,co}}(\varphi)]_0 = \sum_{q=-\infty}^{\infty} g^{(\mathrm{sp})}_{0,q}\, e^{-jq\varphi}$$

where $g^{(\mathrm{sp})}_{0,q} = 1$ if $q = 0,\ 0$ if $q \neq 0$.

For the mixed pressure–particle velocity terms, where $m \in \{1, \ldots, M\}$, we obtain

$$\begin{aligned}
\eta^{(\mathrm{sp})}_{m+1}(\varphi) &= \cos(\delta_m - \varphi), & \zeta^{(\mathrm{sp})}_{0m} &= 1, & \psi^{(\mathrm{sp})}_{0m} &= \phi_m, \\
\eta^{(\mathrm{sp})}_{m(M+1)+1}(\varphi) &= \cos(\delta_m - \varphi), & \zeta^{(\mathrm{sp})}_{m0} &= 1, & \psi^{(\mathrm{sp})}_{m0} &= \phi_m + \pi.
\end{aligned}$$

Hence, the mixed terms correspond to virtual U-probes located on the ring of radius R at angular positions ϕ_m and $\phi_m + \pi$, both oriented along δ_m.

Using the exponential representation

$$\cos(\delta_m - \varphi) = \frac{1}{2} e^{j\delta_m} e^{-j\varphi} + \frac{1}{2} e^{-j\delta_m} e^{j\varphi},$$

the mixed terms introduce harmonics of order $q = \pm 1$. Combining this with the Jacobi–Anger expansion yields

$$[\mathbf{a}^{(\mathrm{sp})}_{\mathrm{u,co}}(\varphi)]_{m+1} = \sum_{q=-\infty}^{\infty} g^{(\mathrm{sp})}_{m+1,q}\, e^{-jq\varphi},$$

where $m \in \{1, \ldots, M\}$ with coefficients

$$\begin{aligned}
g^{(\mathrm{sp})}_{m+1,q} = {} & \frac{1}{2} e^{j\delta_m} j^{q-1} J_{q-1}(\kappa R) e^{j(q-1)\phi_m} \\
& + \frac{1}{2} e^{-j\delta_m} j^{q+1} J_{q+1}(\kappa R) e^{j(q+1)\phi_m}.
\end{aligned}$$

Similarly, for the (u–p) case, with $m \in \{1, \ldots, M\}$, we obtain

$$g^{(\mathrm{sp})}_{m(M+1)+1,q} = \frac{1}{2} e^{j\delta_m} j^{q-1} J_{q-1}(\kappa R) e^{j(q-1)(\phi_m+\pi)} + \frac{1}{2} e^{-j\delta_m} j^{q+1} J_{q+1}(\kappa R) e^{j(q+1)(\phi_m+\pi)}.$$

The (u–u) terms coincide with the general U-probe co-array and therefore introduce second-order harmonic components with shifts $q \pm 2$, as given in (4.4). Consequently, the overall harmonic structure of this special case follows directly from the U-probe formulation, while explicitly accounting for the antipodal geometry introduced by the mixed terms.

Stacking all contributions, the co-array admits the harmonic representation

$$\mathbf{a}^{(\mathrm{sp})}_{\mathrm{u,co}}(\varphi) = \sum_{q=-\infty}^{\infty} \mathbf{g}^{(\mathrm{sp})}_q \, e^{-jq\varphi},$$

where $\mathbf{g}^{(\mathrm{sp})}_q = [g^{(\mathrm{sp})}_{0,q}, g^{(\mathrm{sp})}_{1,q}, g^{(\mathrm{sp})}_{2,q} \ldots, g^{(\mathrm{sp})}_{(M+1)^2,q}]^T \in \mathbb{C}^{(M+1)^2}$ collects the coefficients from all three components.

By truncating the expansion to $|q| \leq Q_{\mathrm{u}}$, we obtain

$$\mathbf{a}^{(\mathrm{sp})}_{\mathrm{u,co}}(\varphi) \approx \mathbf{G}^{(\mathrm{sp})}_{Q_{\mathrm{u}}} \mathbf{v}_{Q_{\mathrm{u}}}(\varphi),$$

where $\mathbf{G}^{(\mathrm{sp})}_{Q_{\mathrm{u}}} = \left[\mathbf{g}^{(\mathrm{sp})}_{-Q_{\mathrm{u}}}, \ldots, \mathbf{g}^{(\mathrm{sp})}_{Q_{\mathrm{u}}}\right] \in \mathbb{C}^{(M+1)^2 \times (2Q_{\mathrm{u}}+1)}$ and $\mathbf{v}_{Q_{\mathrm{u}}}(\varphi)$ is the virtual ULA steering vector. This formulation shows that the special configuration retains the same virtual ULA interpretation as the general U-probe case. The dominant structure is governed by the (u–u) terms, which define the concentric circular geometry and second-order harmonic coupling. The mixed pressure–velocity contributions introduce additional first-order coupling and generate antipodal directional components at radius R, thereby enriching the harmonic content without altering the underlying virtual aperture.

For this special U-probe configuration, the magnitude of $\mathbf{G}^{(\mathrm{sp})}_{Q_{\mathrm{u}}}$ is governed by three distinct contributions. The (p–p) term yields a constant component without angular dependence, which in the harmonic domain corresponds to a single nonzero coefficient at $q = 0$. Thus, it forms a single decaying profile in the magnitude plot.

For the (u–u) terms, the behavior remains identical to the general U-probe case. The magnitude depends on both $\cos(\Delta_{mn})$ and ζ_{mn}. For structured sensor orientations such as tangential and radial configurations, this results in six distinct values of $\cos(\Delta_{mn})$, each associated with a unique ζ_{mn} for $M = 11$. Consequently, the (u–u) contribution exhibits six distinct decaying profiles for these configurations.

For the mixed (p–u) and (u–p) terms, the coefficients are given as linear combinations of shifted Bessel terms of order $q \pm 1$ with phase factors depending on δ_m. When taking the absolute value, these phase terms vanish, and the magnitude depends only on $\zeta^{(\mathrm{sp})}_{mn} = 1$, which is identical for all mixed contributions. However, due to the harmonic shifts $(q \pm 1)$, these terms produce a distinct decay behavior compared to both the (p–p) and (u–u) cases. Moreover, the antipodal placement of the virtual sensors

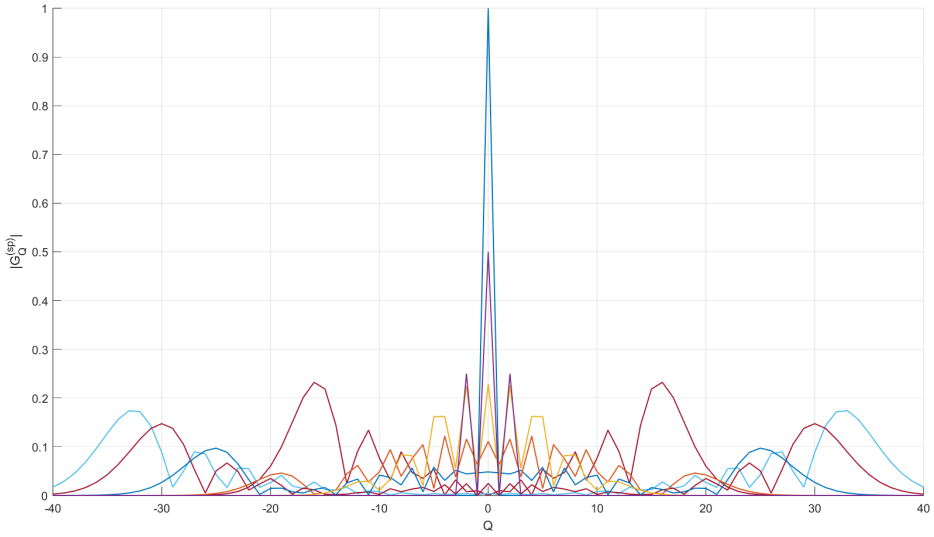


Figure 4.5: Magnitude of the $\mathbf{G}_{Q_{\mathrm{u}}}^{(\mathrm{sp})}$ coefficients as a function of harmonic order q for all unique tangential sensor-pair differences in a UCA with $M = 11$ and $R = 2.8\lambda$, $Q_u^{(\mathrm{sp})} = 40$. The absolute values depend on ζ_{mn} and orders $q \pm 1$ and $q \pm 2$, resulting in eight distinct decay profiles.

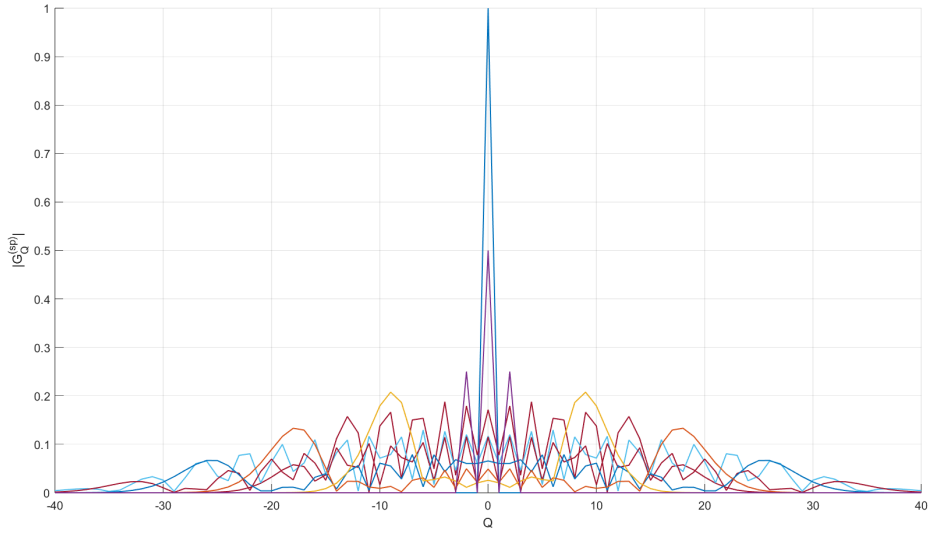


Figure 4.6: Magnitude of the $\mathbf{G}_{Q_{\mathrm{u}}}^{(\mathrm{sp})}$ coefficients as a function of harmonic order q for all unique radial sensor-pair differences in a UCA with $M = 11$ and $R = 2.8\lambda$, $Q_u^{(\mathrm{sp})} = 40$. The absolute values depend on ζ_{mn} and orders $q \pm 1$ and $q \pm 2$, resulting in eight distinct decay profiles.

does not affect the magnitude, and thus all mixed terms collapse into a single additional decaying profile.

Combining all contributions, for tangential and radial sensor orientations, the total number of distinct profiles is therefore eight, specifically six originating from the (u–u) terms, one from the mixed (p–u)/(u–p) terms, and one corresponding to the (p–p)

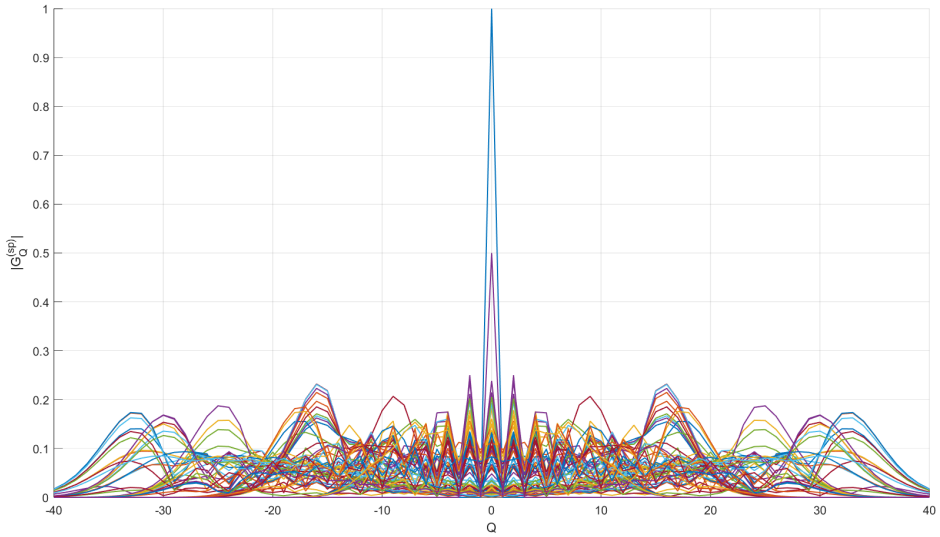


Figure 4.7: Magnitude of the $\mathbf{G}_{Q_{\mathrm{u}}}^{(\mathrm{sp})}$ coefficients as a function of harmonic order q for all unique random sensor-pair differences in a UCA with $M = 11$ and $R = 2.8\lambda$, $Q_u^{(\mathrm{sp})} = 40$.

component at $q = 0$. This behavior is illustrated in Figures 4.5 and 4.6.

For randomly oriented sensors, the dependence on $\cos(\Delta_{mn})$ in the (u–u) terms no longer leads to a fixed set of repeated values. As a result, the number of distinct decay profiles increases, and the clear grouping observed for structured orientations disappears, as shown in Figure 4.7.

4.3 Transformation of UCA Uniaxial PU-Probe Co-Array

We now extend the harmonic-domain transformation to the uniaxial PU-probe co-array. Starting from the unified expression

$$[\mathbf{a}_{\mathrm{pu,co}}(\varphi)]_i = \eta_i(\varphi)\, \exp\big(j\kappa R\zeta_{m(c)m(r)} \cos(\psi_{m(c)m(r)} - \varphi)\big)\,,$$

where we have assumed $\vartheta = \pi/2$ and given $i = 2(c-1)M + r$, the transformation reduces to handling the modulation term

$$\eta_i(\varphi) = \begin{cases} 1, & t(r) = \mathrm{p},\ t(c) = \mathrm{p}, \\ \cos(\delta_{m(c)} - \varphi), & t(r) = \mathrm{p},\ t(c) = \mathrm{u}, \\ \cos(\delta_{m(r)} - \varphi), & t(r) = \mathrm{u},\ t(c) = \mathrm{p}, \\ \cos^2\Big(\delta_{m(c)m(r)} - \varphi\Big) + 0.5\Big(\cos(\Delta_{m(c)m(r)}) - 1\Big), & t(r) = \mathrm{u},\ t(c) = \mathrm{u}. \end{cases}$$

A detailed explanation of these relationships can be found in Section 3.3. As shown in that section, all four measurement combinations share the same exponential term as the pressure-only case. Therefore, the Jacobi–Anger expansion applies identically:

$$\exp\big(j\kappa R\zeta_{m(c)m(r)} \cos(\psi_{m(c)m(r)} - \varphi)\big) = \sum_{q=-\infty}^{\infty} j^q J_q(\kappa R\zeta_{m(c)m(r)}) e^{jq\psi_{m(c)m(r)}} e^{-jq\varphi}.$$

Hence, the harmonic structure of the combined PU co-array is entirely determined by the angular dependence of $\eta_i(\varphi)$. Combining all cases, each entry of the uniaxial PU-probe co-array admits the harmonic expansion

$$[\mathbf{a}_{\mathrm{pu,co}}(\varphi)]_i = \sum_{q=-\infty}^{\infty} g_{i,q}^{(\mathrm{pu})}\, e^{-jq\varphi},$$

where the coefficients $g_{i,q}^{(\mathrm{pu})}$ are given by

$$g_{i,q}^{(\mathrm{pu})} = \begin{cases} g_{i,q}^{(\mathrm{p})}, & t(r)=\mathrm{p},\ t(c)=\mathrm{p}, \\ \frac{1}{2}e^{j\delta_{m(c)}} g_{i,q-1}^{(\mathrm{p})} + \frac{1}{2}e^{-j\delta_{m(c)}} g_{i,q+1}^{(\mathrm{p})}, & t(r)=\mathrm{p},\ t(c)=\mathrm{u}, \\ \frac{1}{2}e^{j\delta_{m(r)}} g_{i,q-1}^{(\mathrm{p})} + \frac{1}{2}e^{-j\delta_{m(r)}} g_{i,q+1}^{(\mathrm{p})}, & t(r)=\mathrm{u},\ t(c)=\mathrm{p}, \\ \frac{1}{2}\cos(\Delta_{m(c)m(r)})\, g_{i,q}^{(\mathrm{p})} + \frac{1}{4}e^{j2\delta_{m(c)m(r)}} g_{i,q-2}^{(\mathrm{p})} + & \\ \qquad \frac{1}{4}e^{-j2\delta_{m(c)m(r)}} g_{i,q+2}^{(\mathrm{p})}, & t(r)=\mathrm{u},\ t(c)=\mathrm{u}, \end{cases}$$

with coefficients $g_{i,q}^{(\mathrm{p})} = j^q J_q(\kappa R \zeta_{m(c)m(r)}) e^{jq\psi_{m(c)m(r)}}$. Stacking all $M_{\mathrm{co}}^{(\mathrm{pu})}$ entries, we obtain

$$\mathbf{a}_{\mathrm{pu,co}}(\varphi) = \sum_{q=-\infty}^{\infty} \mathbf{g}_q^{(\mathrm{pu})}\, e^{-jq\varphi},$$

where $\mathbf{g}_q^{(\mathrm{pu})} = [g_{1,q}^{(\mathrm{pu})}, g_{2,q}^{(\mathrm{pu})} \ldots, g_{(2M)^2,q}^{(\mathrm{pu})}]^T \in \mathbb{C}^{M_{\mathrm{co}}^{(\mathrm{pu})}}$. As in the pressure case, this representation reveals an implicit virtual ULA structure in the harmonic domain. By truncating the expansion to $|q| \le Q_{\mathrm{pu}}$, we obtain the approximation

$$\mathbf{a}_{\mathrm{pu,co}}(\varphi) \approx \sum_{q=-Q_{\mathrm{pu}}}^{Q_{\mathrm{pu}}} \mathbf{g}_q^{(\mathrm{pu})}\, e^{-jq\varphi} = \mathbf{G}_{Q_{\mathrm{pu}}}^{(\mathrm{pu})} \mathbf{v}_{Q_{\mathrm{pu}}}(\varphi), \tag{4.6}$$

where $\mathbf{G}_{Q_{\mathrm{pu}}}^{(\mathrm{pu})} = \left[\, \mathbf{g}_{-Q_{\mathrm{pu}}}^{(\mathrm{pu})}, \ldots, \mathbf{g}_{Q_{\mathrm{pu}}}^{(\mathrm{pu})} \,\right] \in \mathbb{C}^{M_{\mathrm{co}}^{(\mathrm{pu})} \times (2Q_{\mathrm{pu}}+1)}$ and $\mathbf{v}_{Q_{\mathrm{pu}}}(\varphi)$ is the virtual ULA steering vector where its structure is given in (4.2). For the mixed pressure–particle velocity cases, namely (p–u) and (u–p), the coefficients are given as linear combinations of shifted pressure terms $g_{i,q\pm1}^{(\mathrm{p})}$ with phase factors involving δ_{mn}. When taking the absolute value, these phase factors do not affect the magnitude, and the resulting expression depends only on ζ_{mn}. For tangential and radial PU-probe orientations, this implies that the magnitude is determined exclusively by the six unique values of ζ_{mn}. However, due to the involvement of shifted orders $(q \pm 1)$, the resulting decay behavior differs from both the (p–p) and (u–u) cases. Therefore, combining all contributions, for tangential and radial PU-probe orientations, the total number of distinct decaying profiles is 18 which is illustrated in Figures 4.8 and 4.9. However, for randomly oriented PU-probes, similar to the special case, the dependence on $\cos(\Delta_{m(c)m(r)})$ in the (u–u) terms no longer results in a fixed set of repeated values. Consequently, the regular

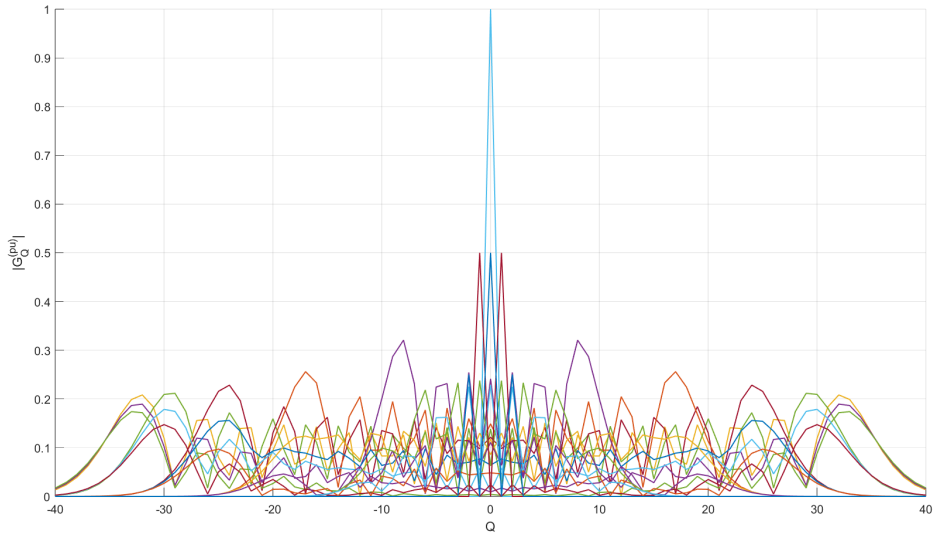


Figure 4.8: Magnitude of the $\mathbf{G}_{Q_{\mathrm{pu}}}^{(\mathrm{pu})}$ coefficients as a function of harmonic order q for all unique tangential sensor-pair differences in a UCA with $M = 11$ and $R = 2.8\lambda$, $Q_{\mathrm{pu}} = 40$. The absolute values depend on ζ_{mn} and orders $q \pm 1$ and $q \pm 2$, resulting in 18 distinct decay profiles.

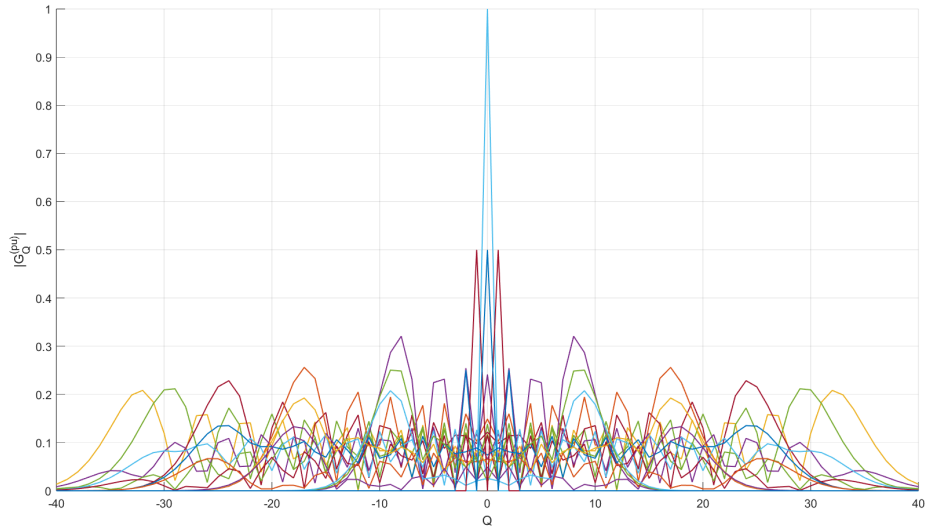


Figure 4.9: Magnitude of the $\mathbf{G}_{Q_{\mathrm{pu}}}^{(\mathrm{pu})}$ coefficients as a function of harmonic order q for all unique radial sensor-pair differences in a UCA with $M = 11$ and $R = 2.8\lambda$, $Q_{\mathrm{pu}} = 40$. The absolute values depend on ζ_{mn} and orders $q \pm 1$ and $q \pm 2$, resulting in 18 distinct decay profiles.

grouping observed for tangential and radial probe orientations is lost. This leads to a larger number of distinct decay profiles, as illustrated in Figure 4.10.

The formulation (4.6) shows that, despite the additional angular modulation introduced by the particle velocity components, the PU-probe co-array can still be mapped to a virtual ULA. Compared to the pressure-only case, where each harmonic order q is

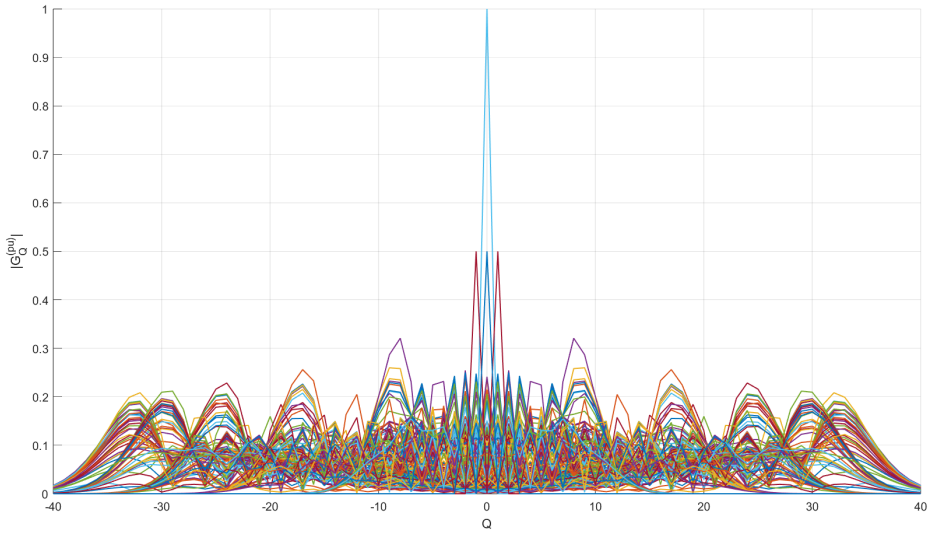


Figure 4.10: Magnitude of the $\mathbf{G}_{Q_{\mathrm{pu}}}^{(\mathrm{pu})}$ coefficients as a function of harmonic order q for all unique random sensor-pair differences in a UCA with $M = 11$ and $R = 2.8\lambda$, $Q_{\mathrm{pu}} = 40$.

independent, the uniaxial PU-probe co-array introduces coupling between neighboring harmonic orders due to the presence of (p–u), (u–p) and (u–u) terms. In contrast to the uniaxial U-probe case, where the harmonic coupling is limited to shifts of ± 2, the PU-probe structure additionally includes ± 1 shifts arising from the mixed pressure–particle velocity components. As a result, the harmonic coefficients in the PU-probe case depend on $g_{i,q}^{(\mathrm{p})}$ as well as its neighboring orders $q \pm 1$ and $q \pm 2$, leading to a richer but more structured coupling across harmonics.

Then, the array response matrix for multiple sources can be written as

$$\mathbf{A}_{\mathrm{pu,co}}(\boldsymbol{\varphi}) = \mathbf{G}_{Q_{\mathrm{pu}}}^{(\mathrm{pu})} \mathbf{V}_{Q_{\mathrm{pu}}}(\boldsymbol{\varphi}),$$

where $\mathbf{V}_{Q_{\mathrm{pu}}}(\boldsymbol{\varphi}) = [\mathbf{v}_{Q_{\mathrm{pu}}}(\varphi_1), \ldots, \mathbf{v}_{Q_{\mathrm{pu}}}(\varphi_K)] \in \mathbb{C}^{(2Q_{\mathrm{pu}}+1)\times K}$. Substituting this into the data model yields

$$\tilde{\mathbf{r}}_{\mathrm{pu}} = \mathbf{A}_{\mathrm{pu,co}}(\boldsymbol{\varphi})\boldsymbol{\gamma} = \mathbf{G}_{Q_{\mathrm{pu}}}^{(\mathrm{pu})} \mathbf{V}_{Q_{\mathrm{pu}}}(\boldsymbol{\varphi})\boldsymbol{\gamma} = \mathbf{G}_{Q_{\mathrm{pu}}}^{(\mathrm{pu})} \mathbf{c}_{Q_{\mathrm{pu}}},$$

with $\mathbf{c}_{Q_{\mathrm{pu}}}$ representing the harmonic coefficients.

4.4 Conclusion

In this chapter, the UCA co-array manifold was transformed into an equivalent virtual ULA representation using the Jacobi–Anger expansion. By expressing the co-array responses in the harmonic domain, the underlying Vandermonde structure required for gridless high-resolution DoA estimation methods was recovered.

The formulation was developed for pressure sensor, uniaxial U-probe, and uniaxial PU-probe co-arrays. While pressure-only arrays lead to independent harmonic components, particle velocity measurements introduce structured coupling between neighboring harmonic orders through shifts of $q \pm 1$ and $q \pm 2$. Despite these additional

interactions, all considered configurations admit a truncated virtual ULA representation.

Building upon the derived virtual ULA representation, the next chapter investigates techniques for overcoming the single-snapshot limitation of the transformed model in the correlation domain and present several processing strategies that enable the effective application of high-resolution gridless DoA estimation techniques, such as ESPRIT and Root-MUSIC, within the proposed virtual ULA framework.

5 Exploiting the ULA Structure

Now that we have derived a mapping $\mathbf{G}^{(\mathrm{p})}_{t,Q_\mathrm{p}}$ $t \in \{a, b\}$, $\mathbf{G}^{(\mathrm{u})}_{Q_\mathrm{u}}$ and $\mathbf{G}^{(\mathrm{pu})}_{Q_\mathrm{pu}}$ for pressure sensor, uniaxial U-probe and uniaxial PU-probe cases between the UCA co-array consisting of $M^{(\mathrm{p})}_{t,\mathrm{co}}$ $t \in \{a, b\}$, $M^{(\mathrm{u})}_{\mathrm{co}}$ and $M^{(\mathrm{pu})}_{\mathrm{co}}$ virtual sensors and an equivalent virtual ULA with $2Q_\mathrm{p}+1$, $2Q_\mathrm{u}+1$ and $2Q_\mathrm{pu}+1$ elements, we are in a position to exploit the well-established structural properties of ULAs. This transformation is particularly beneficial, as it allows us to leverage a wide range of high-resolution DoA estimation techniques that are inherently designed for linear array geometries.

However, an important challenge arises in our setting. Specifically, we operate in the correlation domain under the assumption of a wide-sense stationary process. As a consequence, the available data reduces to a single sample covariance matrix, which can be interpreted as a single snapshot in the transformed domain. This stands in contrast to the standard assumptions underlying high-resolution gridless subspace-based methods, such as ESPRIT and Root-MUSIC, which typically rely on multiple independent snapshots to ensure accurate subspace separation.

The lack of multiple snapshots limits the direct applicability of these methods, as it affects both the estimation accuracy and the ability to reliably distinguish between signal and noise subspaces. Therefore, additional processing strategies are required to overcome this limitation. In the following, we discuss several approaches to address the single-snapshot issue, enabling the effective application of high-resolution techniques within the proposed ULA framework.

5.1 Inverse Modeling and Spatial Smoothing (IMSS)

To overcome the single snapshot limitation, we can adopt an inverse modeling step followed by spatial smoothing in the harmonic domain. The key idea is to reconstruct the harmonic coefficient vector from the observed correlation measurements and subsequently exploit its shift-invariance structure to generate multiple snapshots.

Let $\mathbf{r}$ denote the vectorized correlation measurements and $\mathbf{G}$ the corresponding mapping matrix for a given truncation level Q. Since the harmonic coefficients are not directly observable, they are estimated via a least-squares inversion:

$$\hat{\mathbf{c}} = [\hat{c}_{-Q}, \ldots, \hat{c}_Q]^\top = \mathbf{G}^\dagger \mathbf{r}.$$

This inversion is well-posed when $\mathbf{G}$ is tall, i.e., when the number of co-array elements satisfies $M_\mathrm{co} \geq 2Q+1$. The truncation level Q is dictated by the array geometry and cannot be chosen arbitrarily.

The recovered coefficients $\{\hat{c}_q\}$ follow a sum-of-exponentials model in the harmonic index q, exhibiting a shift-invariance property analogous to that of steering vectors in a

ULA. However, since only a single realization is available, the corresponding covariance matrix is rank-deficient.

To restore rank, spatial smoothing is applied by forming a Hankel matrix:

$$\hat{\mathbf{C}} = \begin{bmatrix} \hat{c}_{-Q} & \hat{c}_{-Q+1} & \cdots & \hat{c}_{Q-P+1} \\ \hat{c}_{-Q+1} & \hat{c}_{-Q+2} & \cdots & \hat{c}_{Q-P+2} \\ \vdots & \vdots & \ddots & \vdots \\ \hat{c}_{-Q+P-1} & \hat{c}_{-Q+P} & \cdots & \hat{c}_{Q} \end{bmatrix},$$

where P denotes the subarray length. Each column corresponds to an overlapping harmonic subarray, effectively generating multiple snapshots.

The spatially smoothed covariance matrix is then computed as

$$\mathbf{R}_{\text{ss}} = \frac{1}{2Q - P + 2} \hat{\mathbf{C}} \hat{\mathbf{C}}^{\mathsf{H}}.$$

This matrix has rank K provided that $P \geq K$ and $2Q - P + 2 \geq K$, enabling the application of gridless subspace-based methods.

The above IMSS procedure applies uniformly across the considered sensing configurations, differing only in the specific form of the measurement vector and mapping matrix. In the pressure-only case, either a non-redundant or redundant co-array representation is used, leading to mapping matrices $\mathbf{G}^{(\text{p})}_{b,Q_{\text{p}}}$ or $\mathbf{G}^{(\text{p})}_{a,Q_{\text{p}}}$, respectively. For the uniaxial U-probe and uniaxial PU-probe configurations, the mappings $\mathbf{G}^{(\text{u})}_{Q_{\text{u}}}$ and $\mathbf{G}^{(\text{pu})}_{Q_{\text{pu}}}$ incorporate particle velocity or combined pressure–velocity measurements.

In all cases, the harmonic coefficients are first estimated via least-squares inversion, followed by Hankel-based spatial smoothing to construct a full-rank covariance matrix.

5.2 Atomic Norm Minimization (ANM)

An alternative strategy to recover the harmonic coefficient vector $\mathbf{c}$ avoids explicit least-squares inversion and instead exploits its inherent spectral sparsity. Under the harmonic-domain model, $\mathbf{c}$ consists of a superposition of K complex exponentials, corresponding to the impinging wavefronts. This structure implies that $\mathbf{c}$ admits a sparse representation over a continuous dictionary parameterized by the angle variable.

More precisely, $\mathbf{c}$ is sparse with respect to the atomic set

$$\mathcal{A} = \{\mathbf{v}_Q(\theta) : \theta \in [0, 2\pi)\},$$

where $\mathbf{v}_Q(\theta)$ denotes the steering vector of a virtual ULA of length $2Q + 1$. This formulation naturally leads to a gridless sparse recovery problem.

To promote sparsity in this continuous domain, we employ the atomic norm as a convex regularizer. The atomic norm of $\mathbf{c}$ with respect to $\mathcal{A}$ is defined as

$$\|\mathbf{c}\|_{\mathcal{A}} = \inf\{t > 0 : \mathbf{c} \in t \cdot \text{conv}(\mathcal{A})\},$$

where $\text{conv}(\mathcal{A})$ denotes the convex hull of the atom set. This norm serves as the tightest convex relaxation for sparsity over the continuous dictionary.

Based on this formulation, the recovery of $\mathbf{c}$ is cast as the following regularized optimization problem:

$$\min_{\mathbf{c}} \ \epsilon\|\mathbf{r} - \mathbf{G}\mathbf{c}\|_2^2 + \|\mathbf{c}\|_{\mathcal{A}}, \tag{5.1}$$

where $\epsilon > 0$ controls the tradeoff between the atomic norm and data fitting error. Compared to the least-squares approach, this formulation is more robust in scenarios with limited observations, as it explicitly enforces the underlying spectral structure.

For the virtual ULA structure considered here, the problem (5.1) admits an equivalent semidefinite programming (SDP) formulation. Specifically, the atomic norm can be expressed via a positive semidefinite Toeplitz matrix, leading to

$$\begin{aligned} \min_{\mathbf{c},\mathbf{u},t} \quad & \epsilon\|\mathbf{r} - \mathbf{G}\mathbf{c}\|_2^2 + \mathrm{tr}(\mathbf{T}(\mathbf{u})) + t \\ \text{s.t.} \quad & \begin{bmatrix} t & \mathbf{c}^H \\ \mathbf{c} & \mathbf{T}(\mathbf{u}) \end{bmatrix} \succeq \mathbf{0}, \end{aligned}$$

where $\mathbf{T}(\mathbf{u})$ is a Hermitian Toeplitz matrix whose first column is given by $\mathbf{u}$. The Toeplitz structure reflects the shift-invariance property of the underlying harmonic model and implicitly encodes the covariance structure of $\mathbf{c}$.

This SDP can be efficiently solved using standard convex optimization solvers such as SeDuMi or SDPT3. For the simulations, we instead employ MOSEK, as it typically offers improved computational performance and faster convergence for large-scale semidefinite programs. Importantly, the formulation does not require discretization of the angular domain, thereby avoiding grid mismatch issues commonly encountered in sparse reconstruction methods.

Once the optimization problem is solved, both the coefficient vector $\mathbf{c}$ and the matrix $\mathbf{T}(\mathbf{u})$ are obtained. The latter can be interpreted as a structured covariance matrix associated with $\mathbf{c}$, and thus directly enables the application of gridless subspace-based DoA estimation techniques without the need for explicit spatial smoothing.

The ANM framework is consistently applicable to all sensing configurations, with variations appearing only in the structure of the measurement vector and its corresponding mapping matrix. In the pressure-only scenario, either a non-redundant or redundant co-array formulation is adopted, resulting in the mappings $\mathbf{G}^{(\mathrm{p})}_{b,Q_\mathrm{p}}$ or $\mathbf{G}^{(\mathrm{p})}_{a,Q_\mathrm{p}}$, respectively. For the uniaxial U-probe and uniaxial PU-probe setups, the mappings $\mathbf{G}^{(\mathrm{u})}_{Q_\mathrm{u}}$ and $\mathbf{G}^{(\mathrm{pu})}_{Q_\mathrm{pu}}$ extend the framework by incorporating particle velocity measurements and combined pressure–velocity observations.

In all cases, the recovery is formulated as a semidefinite program with an atomic norm regularizer, yielding both the coefficient vector and a Hermitian Toeplitz matrix. This matrix directly serves as a structured covariance estimate, enabling gridless subspace-based DoA estimation without requiring spatial smoothing.

5.3 Gridless Subspace Methods

Given either the spatially smoothed covariance matrix $\mathbf{R}_{\mathrm{ss}}$ or the Hermitian Toeplitz covariance matrix $\mathbf{T}(\mathbf{u})$ obtained via ANM, we can proceed with high-resolution gridless subspace-based DoA estimation. Both matrices exhibit the shift-invariance structure

of a virtual ULA and can therefore be directly exploited by classical subspace methods such as ESPRIT and Root-MUSIC.

As a first step, we perform an eigenvalue decomposition of the chosen matrix to obtain an orthonormal basis for the signal and noise subspaces. Specifically, we write

$$\mathbf{R} = \mathbf{U}_s \mathbf{\Lambda}_s \mathbf{U}_s^H + \mathbf{U}_n \mathbf{\Lambda}_n \mathbf{U}_n^H,$$

where $\mathbf{R}$ denotes either $\mathbf{R}_{\text{ss}}$ or $\mathbf{T}(\mathbf{u})$, $\mathbf{U}_s$ contains the K dominant eigenvectors spanning the signal subspace, and $\mathbf{U}_n$ spans the orthogonal noise subspace.

We note that the dimensions of $\mathbf{R}_{\text{ss}}$ and $\mathbf{T}(\mathbf{u})$ generally differ: $\mathbf{R}_{\text{ss}} \in \mathbb{C}^{P \times P}$ depends on the chosen subarray length P, whereas $\mathbf{T}(\mathbf{u}) \in \mathbb{C}^{(2Q+1)\times(2Q+1)}$ directly reflects the full virtual ULA aperture.

5.3.1 ESPRIT

ESPRIT exploits the shift-invariance property of the signal subspace induced by the underlying exponential structure [42]. To this end, we define two selection matrices that extract overlapping subarrays:

$$\mathbf{J}_1 = [\,\mathbf{I}_L \;\; \mathbf{0}\,], \qquad \mathbf{J}_2 = [\,\mathbf{0} \;\; \mathbf{I}_L\,],$$

where L is chosen according to the dimension of $\mathbf{U}_s$.

The rotational invariance property implies that there exists a nonsingular matrix relating the shifted subspaces, which leads to the ESPRIT operator

$$\mathbf{\Psi} = (\mathbf{J}_1 \mathbf{U}_s)^{\dagger} (\mathbf{J}_2 \mathbf{U}_s).$$

The eigenvalues of $\mathbf{\Psi}$ are of the form $e^{-j\varphi_k}$, $k = 1, \ldots, K$, from which the DoAs can be directly extracted via their phases. Notably, ESPRIT avoids spectral search and provides closed-form DoA estimates.

5.3.2 Root-MUSIC

Root-MUSIC, in contrast, operates on the noise subspace and exploits its orthogonality to the array steering vectors. Let $\mathbf{U}_n$ denote the noise subspace, and define the associated projection matrix

$$\mathbf{P}_n = \mathbf{U}_n \mathbf{U}_n^H.$$

Due to the underlying ULA structure, the steering vectors admit a polynomial representation, which allows the DoA estimation problem to be reformulated as a root-finding task [43]. Specifically, we construct a polynomial whose coefficients are obtained by summing the elements of $\mathbf{P}_n$ along its diagonals. Denoting by p_ℓ the sum along the ℓ-th diagonal, the polynomial is given by

$$p(z) = \sum_{\ell} p_\ell z^{-\ell}.$$

The roots of $p(z)$ occur in reciprocal conjugate pairs, and the K roots closest to the unit circle correspond to the signal components. The DoA estimates are then obtained from the arguments of these roots.

In summary, both ESPRIT and Root-MUSIC exploit the shift-invariance structure of the virtual ULA representation, either through the signal subspace or the noise subspace. When combined with the covariance matrices obtained via IMSS or ANM, these methods enable accurate gridless DoA estimation even in the single-snapshot setting.

5.4 Conclusion

To address the single-snapshot limitation inherent to the correlation-domain formulation, two complementary approaches were introduced. The IMSS framework reconstructs the harmonic coefficients through inverse modeling and restores covariance matrix rank via spatial smoothing, while the ANM framework directly exploits the spectral sparsity of the harmonic-domain representation and produces a structured Hermitian Toeplitz covariance matrix. These approaches enable the construction of covariance matrices that preserve the shift-invariance structure of the equivalent virtual ULA. Using these covariance representations, gridless high-resolution subspace methods such as ESPRIT and Root-MUSIC become directly applicable within the proposed framework for pressure, uniaxial U-probe, and uniaxial PU-probe configurations.

In the next chapter, the performance of the proposed framework is evaluated through numerical simulations and comparative analysis under a range of operating conditions, including varying SNR levels and both overdetermined and underdetermined source configurations.

Simulation Results and Comparative Analysis

6

In the previous chapter, we investigated the single-snapshot limitation inherent to the correlation-domain formulation and introduced the IMSS and ANM frameworks to construct structured covariance representations in the virtual ULA domain. These covariance matrices enabled the application of gridless high-resolution subspace methods, such as ESPRIT and Root-MUSIC, for DoA estimation. In this chapter, the performance of the proposed framework is evaluated through a series of numerical simulations under both overdetermined and underdetermined scenarios.

We consider a UCA consisting of $M = 11$ sensors uniformly distributed along a circle. For the PU-probe configuration, two co-located sensing components are available at each spatial location, resulting in a total of 22 measurement channels. The array radius is set to $R = 2.8\lambda$, which for a carrier frequency of $f_c = 8$ kHz and a speed of sound $c = 343$ m/s corresponds to a physical radius of approximately 12 cm. The impinging sources are modeled as uncorrelated wide-sense stationary random processes with powers γ_k drawn uniformly from $[1, 3]$, and are assumed to lie in the plane of the array with fixed elevation $\theta = \pi/2$. The number of temporal snapshots is set to $L = 200$. To reflect realistic conditions, spatially and temporally white complex Gaussian noise is added to the measurements, and the signal-to-noise ratio (SNR) is defined as the ratio between the total source power and the noise power. This simulation setup is kept fixed throughout the chapter, while the number of sources K is varied.

We begin by establishing a baseline in a overdetermined setting ($K < M$) using the classical MUSIC algorithm. Although the primary focus of this work is on gridless high-resolution subspace methods, classical approaches remain valuable for benchmarking purposes in scenarios where they are applicable. In particular, this comparison highlights the consistency of the proposed framework with conventional techniques and provides a reference point before moving to underdetermined cases ($K > M$), where classical methods fail due to inherent dimensionality limitations. Within this context, MUSIC is applied both directly to the physical array covariance matrix and within the proposed framework after mapping the UCA co-array measurements to a virtual ULA and employing IMSS and ANM to construct covariance matrices suitable for subspace-based methods. In addition, the corresponding MUSIC spectra are analyzed to illustrate the impact of different covariance representations on peak sharpness, thereby providing qualitative insight into the effective aperture expansion achieved by each method.

Following this baseline comparison, we turn to underdetermined scenarios and first present single-realization results. These experiments provide a detailed visualization of the estimation performance for fixed source and noise realizations at a representative SNR of 10 dB. Performance is assessed through both visual comparison of estimated and true directions and quantitative evaluation using the root mean square error (RMSE).

To complement these illustrative results, a comprehensive statistical evaluation is

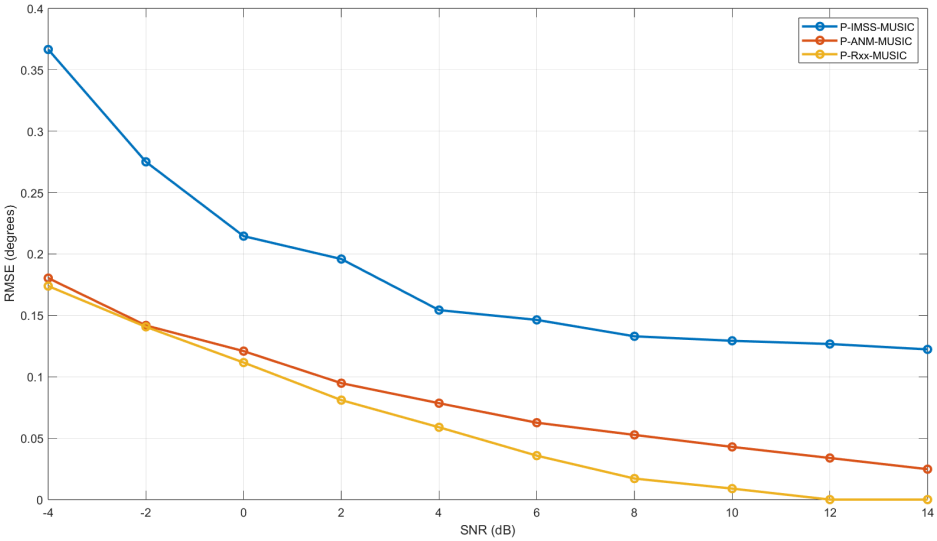


Figure 6.1: RMSE comparison for the pressure case ($K = 3$), showing DoA estimation performance of MUSIC when applied after IMSS and ANM employed to the reconstructed virtual ULA with $Q_{\mathrm{p}} = 40$, and directly using the covariance matrix $\mathbf{R}_{xx}$ in a UCA .

conducted using Monte Carlo simulations. The RMSE is averaged over multiple independent realizations to provide a more reliable measure of performance. RMSE of the estimated DoAs, defined as

$$\mathrm{RMSE} = \sqrt{\frac{1}{K N_{\mathrm{MC}}} \sum_{n=1}^{N_{\mathrm{MC}}} \sum_{k=1}^{K} (\hat{\varphi}_k^{(n)} - \varphi_k)^2},$$

where φ_k denotes the true DoA of the kth source, $\hat{\varphi}_k^{(n)}$ is its estimate in the nth Monte Carlo trial, and $N_{\mathrm{MC}} = 500$ is the number of Monte Carlo simulations. In each trial, new source and noise realizations are generated while the source directions remain fixed. The analysis is conducted over a range of SNR values from -4 dB to 14 dB, enabling a systematic assessment of robustness under varying noise conditions.

6.1 Comparison for $K < M$ through MUSIC

We first establish a baseline in an overdetermined setting ($K < M$) using the classical MUSIC algorithm. MUSIC is utilized both on the actual UCA by means of the sample covariance matrix, and within the proposed approach after transforming the co-array measurements into a virtual ULA and employing IMSS and ANM. This enables a direct comparison of the different covariance representations and their impact on DoA estimation performance. In addition, the MUSIC pseudospectrum is analyzed to provide qualitative insight into the achieved peak sharpness.

In the simulations, the number of sources is chosen as $K = 3$ for the pressure-only and U-probe configurations. For the PU-probe case, results are presented for both $K = 3$ and $K = 6$, reflecting the increased number of available measurement channels.

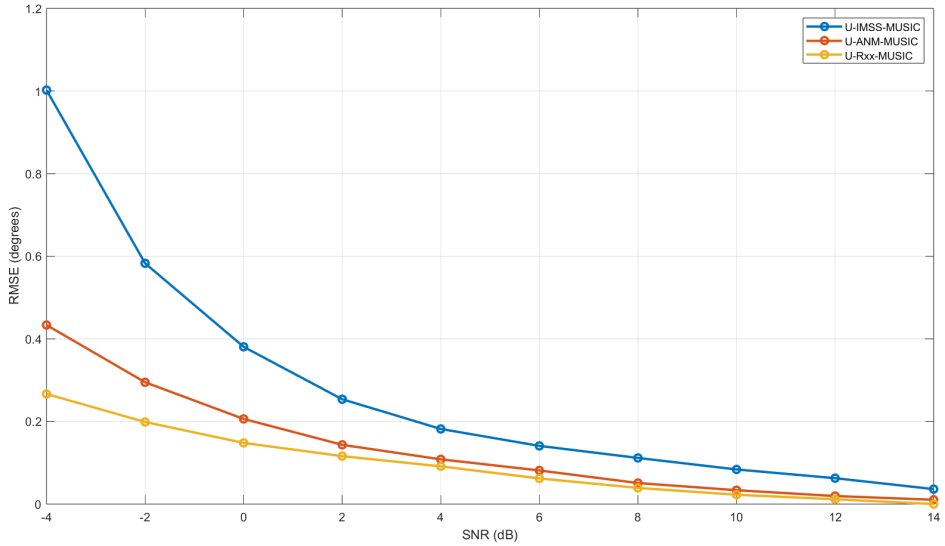


Figure 6.2: RMSE comparison for the U-probe case ($K = 3$), showing DoA estimation performance of MUSIC when applied after IMSS and ANM employed to the reconstructed virtual ULA with $Q_{\mathrm{u}} = 40$, and directly using the covariance matrix $\mathbf{R}_{xx}$ in a UCA.

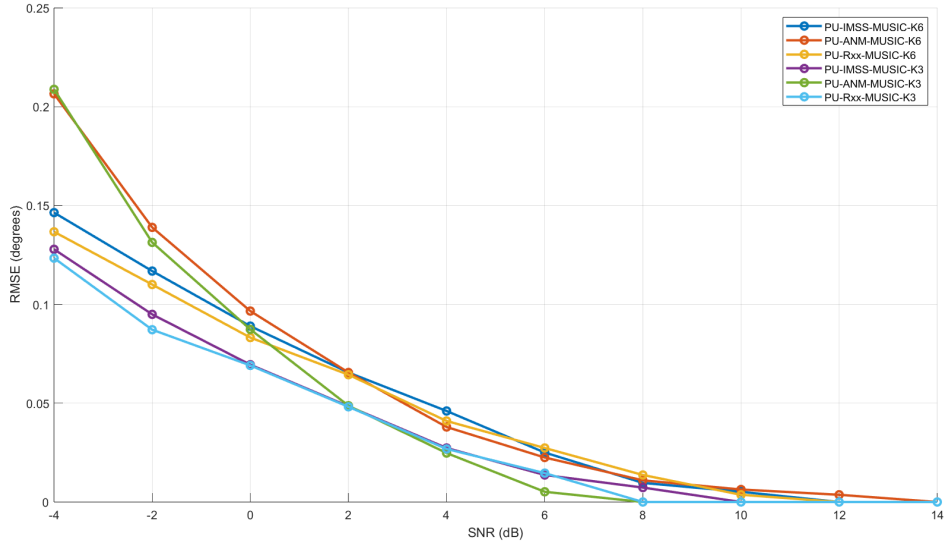


Figure 6.3: RMSE comparison for the PU-probe case ($K = 3$ & $K = 6$), showing DoA estimation performance of MUSIC when applied after IMSS and ANM employed to the reconstructed virtual ULA with $Q_{\mathrm{pu}} = 40$, and directly using the covariance matrix $\mathbf{R}_{xx}$ in a UCA.

For the pressure-only case, non-redundant co-array representation is used for IMSS and ANM. In Figure 6.1, MUSIC applied directly to the covariance matrix $\mathbf{R}_{xx}$ consistently achieves the lowest RMSE across all SNR values, approaching near-zero error at high SNR. In contrast, IMSS-MUSIC exhibits the highest error with an approximately constant gap of around 0.15°, indicating a persistent approximation error introduced

during the virtual ULA construction. The ANM-MUSIC ($\epsilon = 1$) significantly reduces this gap and remains close to the $\mathbf{R}_{xx}$-MUSIC benchmark, particularly at low SNR. However, as SNR increases, the performance difference gradually becomes more pronounced since $\mathbf{R}_{xx}$-MUSIC converges to zero error, whereas ANM-MUSIC retains a small residual error, with a maximum deviation of about 0.04°. This confirms that co-array-based approaches, while effective, cannot fully eliminate approximation errors in the pressure-only configuration.

A similar trend is observed for the U-probe case in Figure 6.2, where sensors are randomly oriented. IMSS-MUSIC again yields the highest RMSE, followed by ANM-MUSIC ($\epsilon = 10$), while $\mathbf{R}_{xx}$-MUSIC maintains the best performance over the entire SNR range. Nevertheless, compared to the pressure-only scenario, ANM-MUSIC remains much closer to the $\mathbf{R}_{xx}$-MUSIC curve, especially SNR higher than 8 dB. Despite this improvement, both IMSS-MUSIC and ANM-MUSIC still exhibit non-zero errors at high SNR due to inherent modeling approximations.

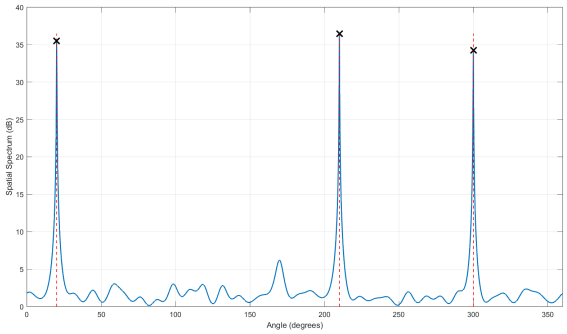
In the PU-probe case shown in Figure 6.3, the behavior differs due to the increased number of measurement channels. At low SNR (below 2 dB), ANM-MUSIC ($\epsilon = 1$) produces the highest RMSE for both $K = 3$ and $K = 6$, followed by IMSS-MUSIC, whereas $\mathbf{R}_{xx}$-MUSIC remains the most robust. In the intermediate SNR range (2–8 dB), ANM-MUSIC slightly outperforms $\mathbf{R}_{xx}$-MUSIC and achieves the lowest RMSE. At higher SNR levels, all methods eventually converge to zero error, albeit at different rates: for $K = 3$, ANM-MUSIC and $\mathbf{R}_{xx}$-MUSIC reach zero RMSE at 8 dB, followed by IMSS-MUSIC at 10 dB; for $K = 6$, IMSS-MUSIC and $\mathbf{R}_{xx}$-MUSIC achieve zero error at 12 dB, while ANM-MUSIC converges at 14 dB. These results indicate that, although co-array-based methods introduce approximation errors in simpler configurations, this combined sensing setup enables all approaches to achieve perfect estimation, especially SNR higher than 8 dB.

6.1.1 MUSIC Spectrum Comparison

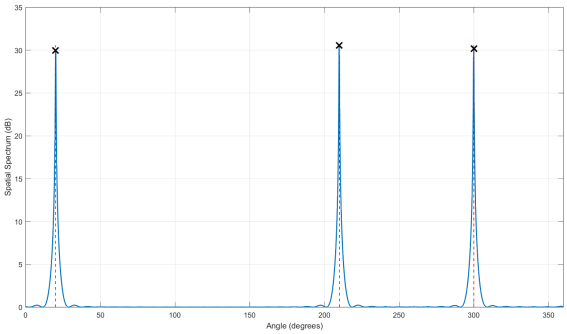
To further illustrate the differences between the considered approaches, the MUSIC spectra for the pressure-only configuration are compared in Figure 6.4–6.5. The spectra are obtained using four different inputs: the covariance matrix $\mathbf{R}_{xx}$ obtained from the measurements, the IMSS-based $\mathbf{R}_{\text{ss}}$, the ANM-based covariance-like matrix $\mathbf{T}(\mathbf{u}^{(\text{p})})$, and the spatial smoothing applied to harmonic coefficient vector $\hat{\mathbf{c}}_{Q_\text{p}}$ obtained via ANM.

As observed from the figures, all approaches are able to correctly identify the source directions; however, the sharpness of the peaks varies significantly. The narrowest peaks are obtained when MUSIC is applied to the ANM-based covariance matrix $\mathbf{T}(\mathbf{u}^{(\text{p})})$, followed by the spectrum obtained using ANM-based $\hat{\mathbf{c}}_{Q_\text{p}}$, then IMSS, and finally the $\mathbf{R}_{xx}$-based spectrum, which exhibits the widest peaks.

This behavior can be explained by the effective size of the covariance-like matrices used in each method. In particular, $\mathbf{T}(\mathbf{u}^{(\text{p})}) \in \mathbb{C}^{(2Q_\text{p}+1)\times(2Q_\text{p}+1)}$ provides the largest virtual aperture, resulting in the sharpest peaks. The ANM-based approach using $\hat{\mathbf{c}}_{Q_\text{p}}$ also benefits from an increased virtual dimension, though to a lesser extent. In comparison, IMSS offers a moderate aperture expansion, while the original covariance matrix $\mathbf{R}_{xx}$ is limited by the physical array size.

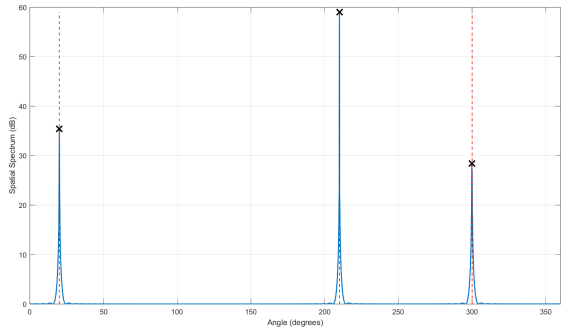


(a) MUSIC spectrum on $\mathbf{R}_{xx}$.

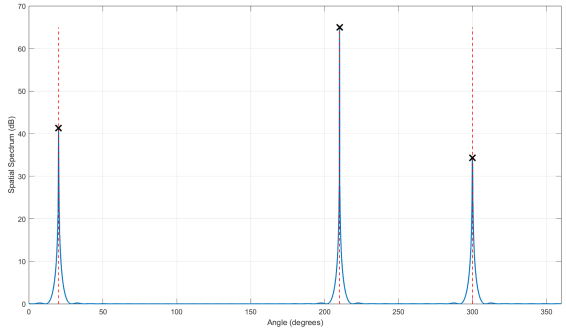


(b) MUSIC spectrum after IMSS-based $\mathbf{R}_{\text{ss}}$.

Figure 6.4: Comparison of MUSIC spectra using the covariance matrix $\mathbf{R}_{xx}$ (left) and the IMSS-based $\mathbf{R}_{\text{ss}}$ (right) for $K = 3$, $Q_{\text{p}} = 40$, SNR $= 10$ dB.



(a) MUSIC spectrum using the ANM-based covariance like matrix $\mathbf{T}(\mathbf{u}^{(\text{p})})$.



(b) MUSIC spectrum using the ANM-based $\hat{\mathbf{c}}_{Q_{\text{p}}}$.

Figure 6.5: Comparison of MUSIC spectra using ANM-based $\mathbf{T}(\mathbf{u}^{(p)})$ (left) and $\hat{\mathbf{c}}_{Q_{\text{p}}}$ (right) for $K = 3$, $Q_{\text{p}} = 40$, SNR $= 10$ dB.

For this reason, in the ANM-based framework, the covariance-like matrix $\mathbf{T}(\mathbf{u}^{(\text{p})})$ is preferred, as it inherently provides a structured Toeplitz form with an enlarged virtual aperture. Consequently, no additional spatial smoothing is required, unlike in IMSS-based approaches.

It is important to note that MUSIC is employed here primarily for visualization and comparison purposes. In particular, it is applied in scenarios where the number of sources is smaller than the number of sensors, allowing the pseudospectrum to provide an intuitive illustration of peak sharpness.

However, the main results of this work rely on gridless subspace methods, specifically ESPRIT and Root-MUSIC. These methods are preferred over conventional MUSIC because they do not require a search over a predefined angular grid. As a result, they avoid grid mismatch errors and are better suited for accurately estimating off-grid source directions, while also offering reduced computational complexity.

6.2 Single Realization Results

In this section, we evaluate the performance of the proposed gridless subspace-based DoA estimation methods when applied to a virtual ULA constructed from a UCA co-array for a single realization. In particular, we consider $K = 16$ and $K = 25$ narrowband far-field sources impinging on the array from distinct directions. This leads to an underdetermined setting for the pressure-only and U-probe-only configurations, while the PU-probe case remains overdetermined for $K = 16$ (i.e., $K < 22$). Performance is evaluated for a single realization of source locations and noise, providing insight into the behavior of the proposed methods under practical finite-sample conditions. For this realization for both $K = 16$ and $K = 25$, SNR is set to 10 dB. For the ANM-based approaches, the regularization parameter is set to $\epsilon = 1$ for the pressure-only configuration, and $\epsilon = 10$ for both the U-probe and PU-probe cases. To quantify the estimation performance, the RMSE between the true and estimated DoAs is employed. For all cases, same source and noise realizations are used and the source directions remain fixed.

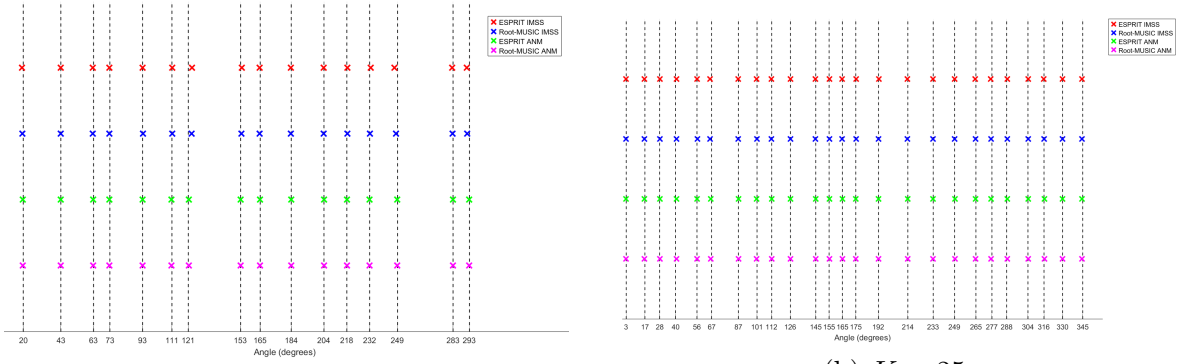
6.2.1 Pressure Sensor Setup

In the pressure-only configuration, we consider two processing strategies for constructing the virtual ULA from the co-array UCA measurements. In the first approach, a selection matrix is applied to retain only the non-redundant co-array elements ($M_{b,\mathrm{co}}^{(\mathrm{p})}$), effectively discarding repeated lags. In the second approach, all available co-array measurements ($M_{a,\mathrm{co}}^{(\mathrm{p})}$), including redundant entries, are preserved and directly exploited.

The estimated DoAs obtained using ESPRIT and Root-MUSIC for both IMSS and ANM approaches are illustrated in Figures 6.6 and 6.7. The alignment between the true DoAs (dashed lines) and the estimated angles (crosses) provides a visual indication of estimation accuracy. For $K = 16$, both approaches yield reasonable reconstruction performance, with ANM exhibiting tighter clustering around the true angles compared to IMSS. This observation is consistent with the RMSE values reported in Table 6.1, where ANM significantly outperforms IMSS.

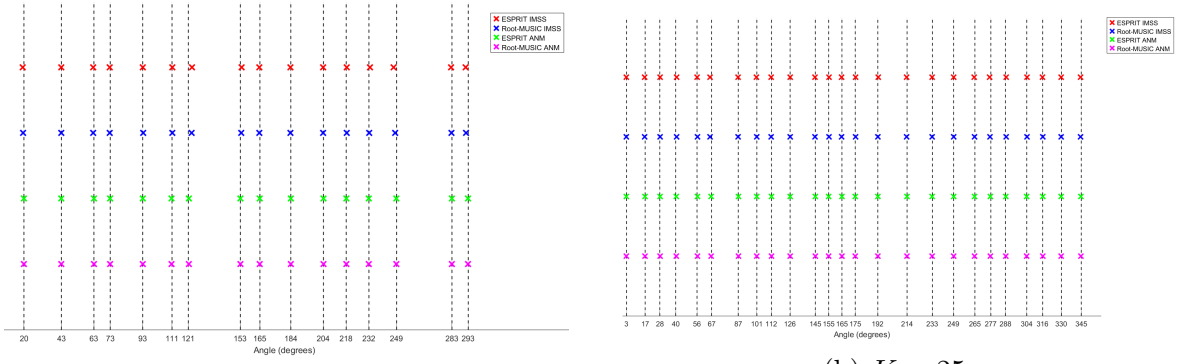
	ESPRIT		**Root-MUSIC**	
Method	$K = 16$	$K = 25$	$K = 16$	$K = 25$
Non-Redundant ($M_{b,\mathrm{co}}^{(\mathrm{p})}$) IMSS	0.9°	0.44°	0.7°	0.41°
Non-Redundant ($M_{b,\mathrm{co}}^{(\mathrm{p})}$) ANM	0.18°	0.33°	0.18°	0.33°
Redundant ($M_{a,\mathrm{co}}^{(\mathrm{p})}$) IMSS	0.9°	0.44°	0.7°	0.41°
Redundant ($M_{a,\mathrm{co}}^{(\mathrm{p})}$) ANM	0.12°	0.2°	0.12°	0.2°

Table 6.1: RMSE performance comparison for pressure co-array constructions with ESPRIT and Root-MUSIC for IMSS and ANM for $K = 16$ and $K = 25$.



(a) $K = 16$. (b) $K = 25$.

Figure 6.6: Comparison of true DoAs (dashed lines) and estimates obtained (crosses) via non-redundant pressure co-array using ESPRIT and Root-MUSIC methods for both IMSS and ANM approaches for $K = 16$ and 25, $Q_{\mathrm{p}} = 40$, SNR $= 10$ dB.



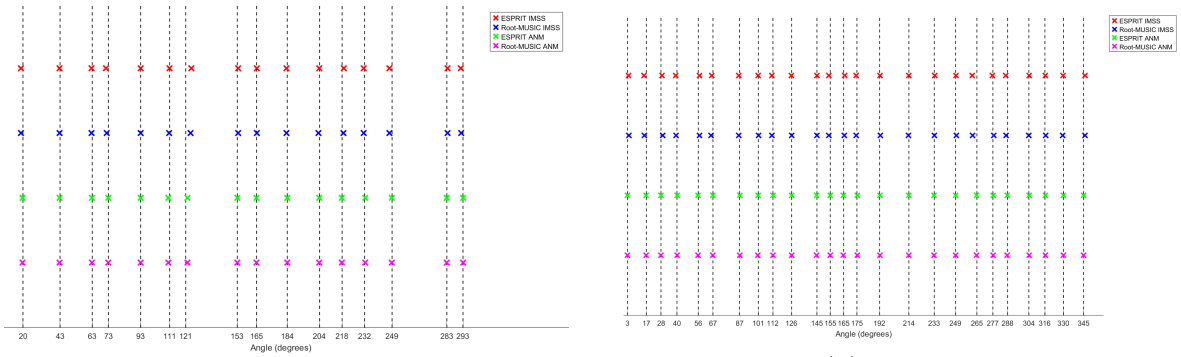
(a) $K = 16$. (b) $K = 25$.

Figure 6.7: Comparison of true DoAs (dashed lines) and estimates obtained (crosses) via redundant pressure co-array using ESPRIT and Root-MUSIC methods for both IMSS and ANM approaches for $K = 16$ and 25, $Q_{\mathrm{p}} = 40$, SNR $= 10$ dB.

6.2.2 U-Probe Setup

In the U-probe configuration, each sensor measures a single component of the acoustic particle velocity. We consider three different orientation strategies for these sensors namely tangential, radial, and random. For illustration, the estimated DoAs for tangential configurations is shown in Figure 6.8. The RMSE values reported in Table 6.2 summarize the estimation accuracy for all configurations and methods. These results reflect the variations in performance induced by different sensor orientations and highlight the impact of directional sensitivity in particle velocity measurements.

From Table 6.2 it can be observed that ANM consistently outperforms IMSS across all configurations and both ESPRIT and Root-MUSIC methods, yielding lower RMSE values for this realization. Among the IMSS-based approaches, the tangential configuration results in the highest estimation error. In contrast, the random orientation with ANM achieves the lowest RMSE for all considered cases.



(a) $K = 16$.

(b) $K = 25$.

Figure 6.8: Comparison of true DoAs (dashed lines) and estimates obtained (crosses) on tangential U-probe configuration using ESPRIT and Root-MUSIC methods for both IMSS and ANM approaches for $K = 16$ and 25, $Q_{\mathrm{u}} = 40$, SNR = 10 dB.

	ESPRIT		**Root-MUSIC**	
Method	$K = 16$	$K = 25$	$K = 16$	$K = 25$
Tangential IMSS	1.16°	1.02°	1.1°	1.03°
Tangential ANM	0.36°	0.19°	0.35°	0.17°
Radial IMSS	0.84°	0.7°	0.73°	0.39°
Radial ANM	0.4°	0.42°	0.4°	0.4°
Random IMSS	0.26°	0.36°	0.24°	0.21°
Random ANM	0.18°	0.21°	0.18°	0.21°

Table 6.2: RMSE performance comparison for U-probe configurations using ESPRIT and Root-MUSIC with IMSS and ANM for $K = 16$ and $K = 25$.

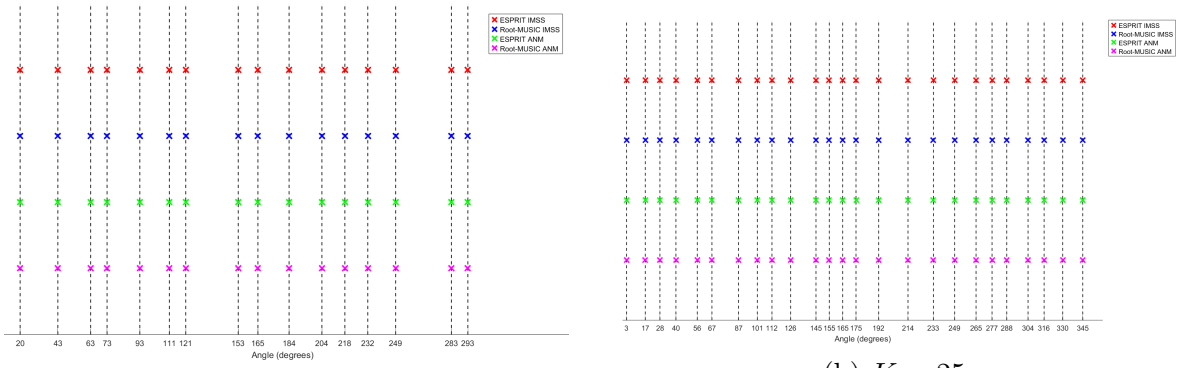
6.2.3 PU-Probe Setup

This joint sensing setup increases the available spatial information and is also incorporated into the virtual ULA construction. As the U-probe case, same orientation strategies are considered for the velocity component. The corresponding DoA estimation results for tangential configuration is shown in Figure 6.9. The estimated angles can be observed to closely follow the true DoAs across both $K = 16$ and $K = 25$ scenarios. The RMSE values summarized in Table 6.3 provide a quantitative measure of the estimation accuracy for all configurations and methods.

In the PU-probe case, doubling the channels ($2M$) significantly improves estimation accuracy, leading all methods across all sensor orientations and for both 16 and 25 sources to achieve the lowest RMSE under high SNR compared to previous setups.

6.3 RMSE Performance versus SNR

In previous section, the analysis was based on a single realization of source locations and noise. While such results provide useful insight, they do not fully capture the statistical performance of the proposed methods. To obtain a more comprehensive assessment, this section extends the evaluation by considering multiple Monte Carlo simulations.



(a) $K = 16$.

(b) $K = 25$.

Figure 6.9: Comparison of true DoAs (dashed lines) and estimates obtained (crosses) on tangential PU-probe configuration using ESPRIT and Root-MUSIC methods for both IMSS and ANM approaches for $K = 16$ and 25, $Q_{\text{pu}} = 40$, SNR $= 10$ dB.

	ESPRIT		**Root-MUSIC**	
Method	$K = 16$	$K = 25$	$K = 16$	$K = 25$
Tangential IMSS	0.04°	0.08°	0.04°	0.07°
Tangential ANM	0.03°	0.08°	0.03°	0.07°
Radial IMSS	0.06°	0.09°	0.05°	0.06°
Radial ANM	0.06°	0.07°	0.05°	0.07°
Random IMSS	0.06°	0.06°	0.05°	0.06°
Random ANM	0.07°	0.05°	0.06°	0.05°

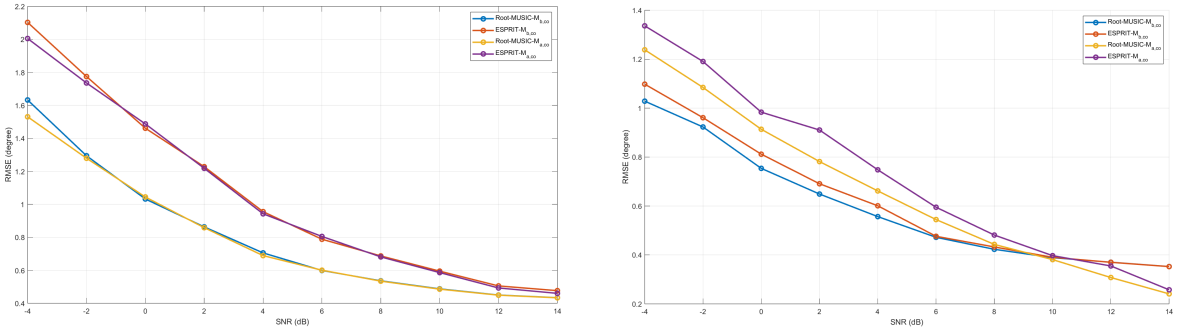
Table 6.3: RMSE performance comparison for PU-probe configurations using ESPRIT and Root-MUSIC with IMSS and ANM for $K = 16$ and $K = 25$.

The results are averaged over $N_{\text{MC}} = 500$ independent realizations, providing a reliable assessment of estimation accuracy under varying noise conditions. We consider $K = 33$. The statistical performance of the proposed framework is evaluated in terms of the RMSE as a function of the SNR. The evaluation is carried out for three sensing configurations namely pressure-only, U-probe, and the PU-probe case.

6.3.1 Pressure Co-Array Configuration

For the pressure-only case, two co-array configurations namely a non-redundant co-array and a redundant co-array are considered. The RMSE performance of ESPRIT and Root-MUSIC is evaluated after applying IMSS and ANM, respectively and shown in Figure 6.10.

For the IMSS-based approach, the redundant pressure co-array yields a slightly lower RMSE than the non-redundant configuration in the low SNR regime, specifically at -4 dB and -2 dB. As the SNR increases beyond this region, the performance of both co-array configurations becomes nearly identical, with overlapping RMSE trends across the remaining SNR range. In contrast, for the ANM-based approach, the non-redundant co-array achieves lower RMSE than the redundant configuration over the low to moderate SNR range. However, this behavior changes at higher SNR values such



(a) IMSS. (b) ANM.

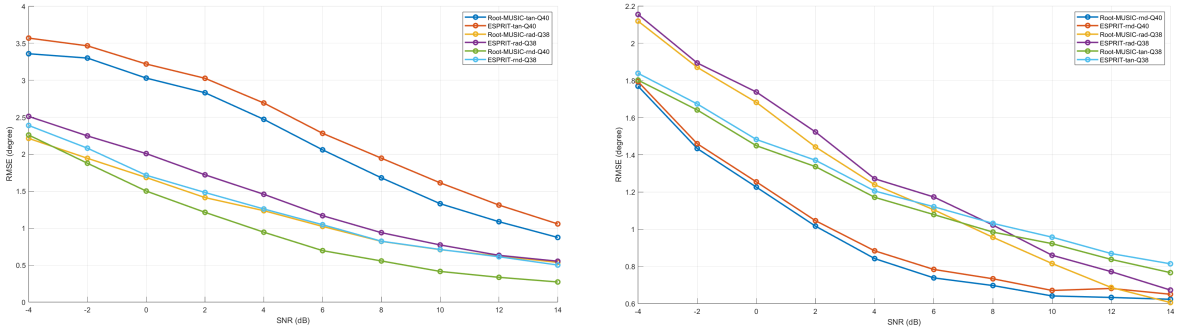
Figure 6.10: Comparison of non-redundant and redundant pressure co-array via RMSE versus SNR using ESPRIT and Root-MUSIC methods for both IMSS and ANM approaches for $K = 33$, $Q_{\mathrm{p}} = 40$, $\epsilon = 1$.

that from approximately 10 dB onwards, the redundant co-array begins to outperform the non-redundant one, resulting in lower RMSE.

These observations indicate that, for IMSS, redundancy in the co-array provides a benefit primarily in low SNR conditions, whereas for ANM, the redundant co-array becomes advantageous in the high SNR regime.

6.3.2 U-Probe Configuration

For the U-probe case, three different sensor orientations of tangential, radial, and random are considered. These configurations influence the structure of the virtual array and, consequently, the estimation performance.



(a) IMSS. (b) ANM.

Figure 6.11: Comparison of U-probe orientations via RMSE versus SNR using ESPRIT and Root-MUSIC methods for both IMSS and ANM approaches for $K = 33$, $\epsilon = 1$.

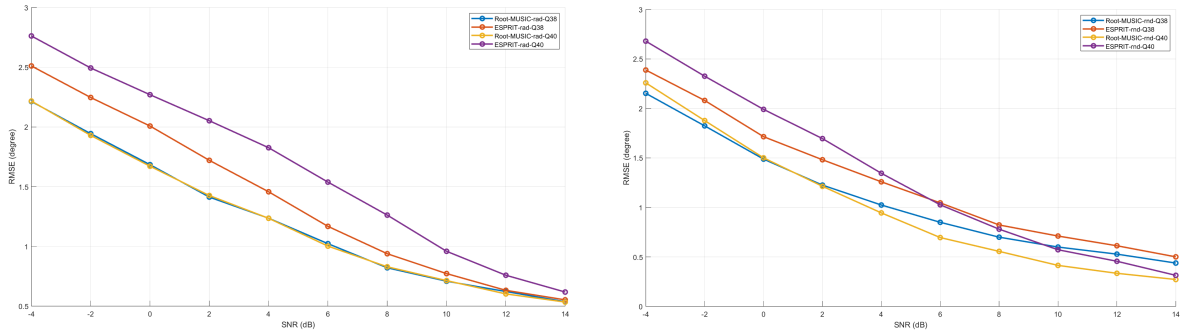
Figure 6.11 compares the RMSE performance as a function of SNR for both IMSS and ANM approaches using ESPRIT and Root-MUSIC. Overall, Root-MUSIC consistently achieves lower RMSE than its ESPRIT counterpart across all configurations and SNR values.

Focusing first on the IMSS results, the optimal truncation parameter is found to be $Q_{\mathrm{u}} = 40$ for the tangential configuration, whereas $Q_{\mathrm{u}} = 38$ yields the smallest errors for

radial orientation. Despite $Q_{\mathrm{u}} = 40$ providing the best performance for the tangential case, this configuration consistently exhibits the highest RMSE over the entire SNR range. In the low SNR regime, the tangential configuration shows approximately 1° to 1.5° higher error compared to the radial and random cases. As the SNR increases, this gap gradually diminishes.

Across the full SNR range, the lowest RMSE is achieved by Root-MUSIC with random orientation ($Q_{\mathrm{u}} = 40$). The second-best performance is obtained by Root-MUSIC with radial orientation up to approximately 8 dB. Beyond this point, ESPRIT with random orientation ($Q_{\mathrm{u}} = 38$) surpasses it, with the random configuration ultimately yielding the lowest RMSE at higher SNR values.

The observed behavior for IMSS can be explained by the structure of the matrix inversion involved. Specifically, the matrix $\mathbf{G}_{Q_{\mathrm{u}}}^{(\mathrm{u})}$ must satisfy $M_{\mathrm{co}}^{(\mathrm{u})} > 2Q_u + 1$, i.e., it should be tall. For smaller Q_{u}, the matrix becomes taller, which improves the conditioning of the inversion and leads to more accurate estimates. This explains why smaller Q_{u} generally results in lower RMSE. However, this trend does not hold for the tangential configuration. As shown in Figure 4.2, the magnitude of the coefficients of $\mathbf{G}_{Q_{\mathrm{u}}}^{(\mathrm{u})}$ as a function of the harmonic order q remains relatively large compared to the radial case. Therefore, $Q_{\mathrm{u}} = 38$ does not provide sufficient truncation for the tangential configuration. In contrast, for the radial configuration, the magnitude of the coefficients decays earlier, making $Q_{\mathrm{u}} = 38$ an adequate truncation point.

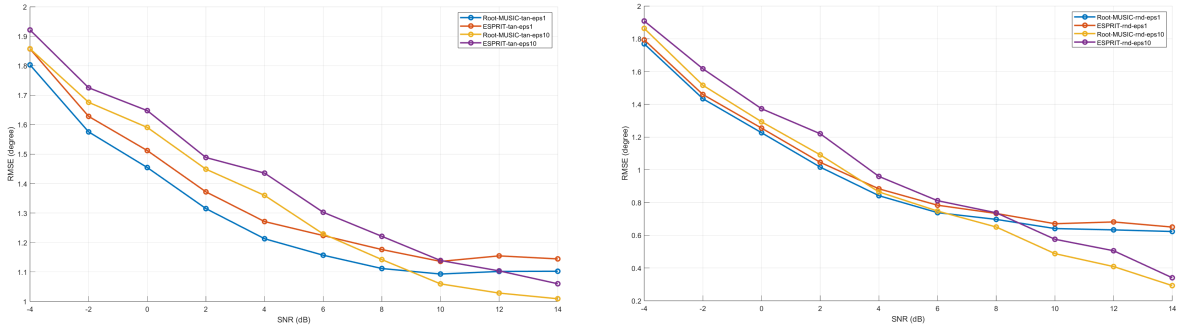


(a) Radial U-probe orientation.

(b) Random U-probe orientation.

Figure 6.12: Comparison of $Q_{\mathrm{u}} = 38$ and $Q_{\mathrm{u}} = 40$ via RMSE versus SNR using ESPRIT and Root-MUSIC methods for IMSS approach for $K = 33$.

For the random orientation, the selection of Q_{u} is less straightforward. A comparison between $Q_{\mathrm{u}} = 38$ and $Q_{\mathrm{u}} = 40$ for IMSS applied both on radial and random configurations is provided in Figure 6.12. For the radial case, Root-MUSIC achieves nearly identical performance for both values of Q_{u}, whereas ESPRIT benefits significantly from $Q_{\mathrm{u}} = 38$, yielding noticeably lower RMSE. In the random configuration, Root-MUSIC with $Q_{\mathrm{u}} = 38$ provides slightly lower RMSE for SNR below 0 dB. However, for SNR values above 0 dB, $Q_{\mathrm{u}} = 40$ yields the best performance. A similar trend is observed for ESPRIT such that $Q_{\mathrm{u}} = 38$ performs better up to approximately 6 dB, after which $Q_{\mathrm{u}} = 40$ becomes superior. These observations suggest that for random orientations, smaller Q_{u} values are advantageous in the low SNR regime due to improved inversion accuracy, as the matrix $\mathbf{G}_{Q_{\mathrm{u}}}^{(\mathrm{u})}$ becomes taller.



(a) Tangential U-probe orientation.

(b) Random U-probe orientation.

Figure 6.13: Comparison of $\epsilon = 1$ and $\epsilon = 10$ via RMSE versus SNR using ESPRIT and Root-MUSIC methods for ANM approach for $K = 33$, $Q_{\mathrm{u}} = 40$.

For the ANM approach, Root-MUSIC with random sensor orientation and $Q_{\mathrm{u}} = 40$ yields the lowest RMSE across the entire SNR range. For the tangential and radial configurations, $Q_{\mathrm{u}} = 38$ provides slightly lower RMSE compared to $Q_{\mathrm{u}} = 40$. For this reason, the curves shown in Figure 6.11 with $Q_{\mathrm{u}} = 38$ for tangential and radial, and $Q_{\mathrm{u}} = 40$ for the random orientation.

Comparing the configurations, the tangential orientation achieves lower estimation errors than the radial configuration up to approximately 8 dB. Beyond this point, the radial configuration outperforms the tangential one and continues to improve at a faster rate in the high SNR regime. At around 14 dB, the radial configuration yields the smallest RMSE, although the difference between radial and random orientations becomes marginal at high SNR values.

It is important to note that all curves in Figure 6.11 correspond to $\epsilon = 1$. The choice of ϵ has a significant impact on the estimation performance. A comparison between $\epsilon = 1$ and $\epsilon = 10$ for tangential and random configurations is presented in Figure 6.13.

For the tangential configuration, $\epsilon = 1$ yields lower RMSE for both Root-MUSIC and ESPRIT up to approximately 10 dB. However, for SNR above 10 dB, $\epsilon = 10$ provides more accurate estimates. In fact, for $\epsilon = 1$, the RMSE slightly increases at very high SNR values compared to its value around 10 dB for both gridless methods. A similar trend is observed for the random orientation. For low SNR values, $\epsilon = 1$ achieves lower RMSE than $\epsilon = 10$. However, for Root-MUSIC, $\epsilon = 10$ outperforms $\epsilon = 1$ beyond approximately 6 dB, while for ESPRIT this transition occurs around 8 dB.

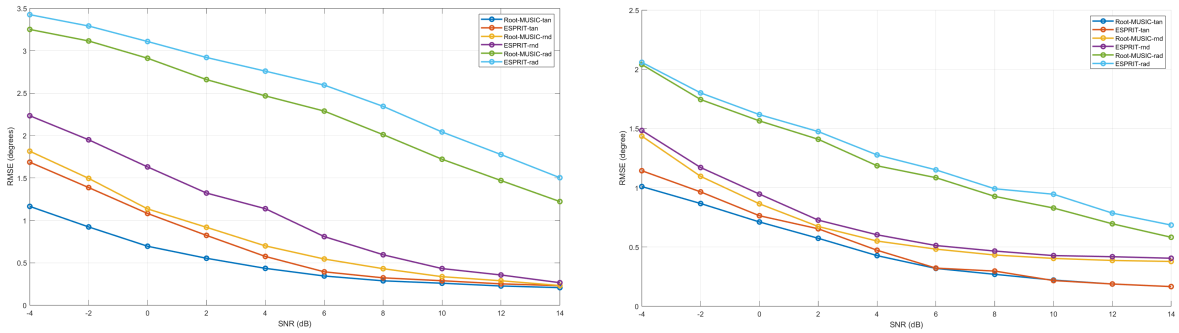
This behavior can be explained by the role of the regularization parameter ϵ. At high SNR, the term $\|\tilde{\mathbf{r}}_{\mathrm{u}} - \mathbf{G}_{Q_{\mathrm{u}}}^{(\mathrm{u})} \mathbf{c}_{Q_{\mathrm{u}}}\|_2^2$ becomes less affected by noise, and a larger ϵ helps improve estimation accuracy. In contrast, at low SNR, a large ϵ amplifies the noise contribution, which degrades the estimation performance.

6.3.3 Special Case: U-Probe with a Central Pressure Sensor

The first observation from Figure 6.14 confirms that the previously identified trend where Root-MUSIC achieves lower RMSE than ESPRIT persists under this specific

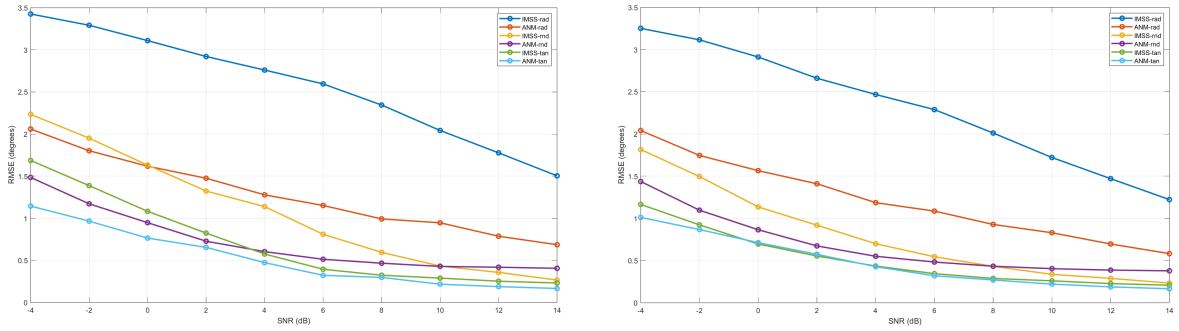
setup. Moreover, the discrepancy in performance between Root-MUSIC and ESPRIT is significantly more pronounced when using IMSS compared to ANM.

Considering both IMSS and ANM approaches, the probe orientation has a clear impact on estimation accuracy. The radial configuration consistently exhibits the highest RMSE across the entire SNR range, whereas the tangential configuration yields the lowest error. It is important to note that, for all U-probe orientations, the parameters Q_{u} and ϵ are kept constant at 40 and 1, respectively, ensuring a fair comparison across configurations for this setup.



(a) IMSS. (b) ANM.

Figure 6.14: Comparison of U-probe orientations with a central pressure sensor via RMSE versus SNR using ESPRIT and Root-MUSIC methods for both IMSS and ANM approaches for $K = 33$, $Q_{\mathrm{u}} = 40$, $\epsilon = 1$.



(a) ESPRIT. (b) Root-MUSIC.

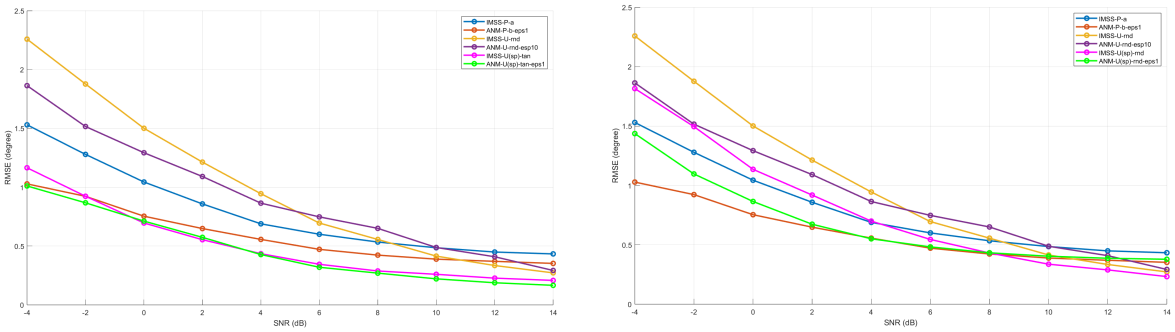
Figure 6.15: Comparison of ESPRIT and Root-MUSIC methods applied on U-probe orientations with a central pressure sensor via RMSE versus SNR for both IMSS and ANM approaches for $K = 33$, $Q_{\mathrm{u}} = 40$, $\epsilon = 1$.

Further insights can be drawn from Figure 6.15, where the RMSE performance of ESPRIT and Root-MUSIC are directly compared. In general, ANM demonstrates superior performance over IMSS by achieving lower RMSE values. This improvement is most evident in the radial configuration, where the gap between IMSS and ANM is the largest for both ESPRIT and Root-MUSIC.

In contrast, the random orientation shows a smaller performance gap between IMSS and ANM. Notably, for ESPRIT, the IMSS-based random configuration begins to out-

perform its ANM counterpart beyond approximately 10 dB SNR. A similar crossover behavior is observed for Root-MUSIC, occurring slightly earlier at around 8 dB.

For the tangential configuration, ESPRIT exhibits the smallest difference between IMSS and ANM. In the case of Root-MUSIC, this gap effectively disappears, with both IMSS and ANM curves closely overlapping across the entire SNR range, indicating nearly identical performance.



(a) Tangential U(sp) configuration.

(b) Random U(sp) configuration.

Figure 6.16: RMSE versus SNR comparison using Root-MUSIC for both IMSS and ANM approaches for pressure-only (P), U-probe (U), and special U-probe (U(sp)) configurations with $K = 33$, $M = 11$, $L = 200$, $Q = 40$ and $R = 2.8\lambda$.

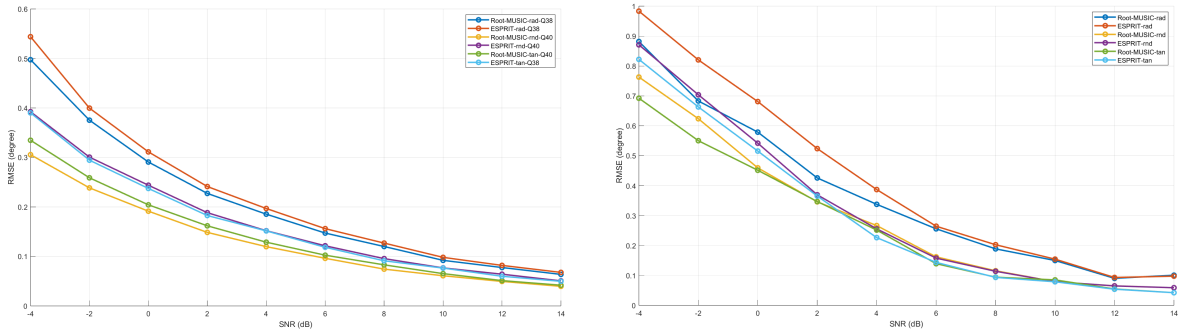
The performance of the proposed U-probe configuration with a central pressure sensor is compared with the previously discussed pressure-only and U-probe-only cases. Figure 6.16 illustrates the RMSE curves corresponding to the best-performing setups for each configuration. It is observed that, across all cases, the minimum RMSE is consistently achieved using the Root-MUSIC algorithm. Therefore, the comparison presented here focuses on Root-MUSIC applied to pressure-only, U-probe-only, and the special U-probe configurations.

Figure 6.16(a) presents the comparison for the tangential special U-probe configuration, while Figure 6.16(b) corresponds to the random orientation of the special U-probe. For the tangential configuration, ANM achieves the lowest RMSE, closely followed by IMSS, particularly for SNR values above approximately -2 dB. Both methods outperform the best-performing pressure-only and U-probe-only configurations across nearly the entire SNR range. In the case of the random special U-probe configuration, the ANM-based approach initially exhibits inferior performance compared to the pressure-only non-redundant co-array with ANM up to around 2 dB. Beyond this point, however, both approaches demonstrate similar performance, with closely aligned RMSE curves. On the other hand, the IMSS-based random special U-probe configuration shows a notable improvement at higher SNR levels, outperforming all other configurations beyond approximately 8 dB.

Overall, these results indicate that the tangential special U-probe configuration provides the most favorable performance among the considered orientations. It consistently achieves lower RMSE than both the pressure-only and U-probe-only setups, while requiring only a marginal increase in system complexity. Specifically, a single channel is added, resulting in a total of $M + 1$ channels.

6.3.4 PU-Probe Configuration

Finally, the PU-probe configuration is considered, where pressure sensors are augmented with U-probe measurements. As in the previous case, three particle velocity sensor orientations namely tangential, radial, and random are evaluated.



(a) IMSS. (b) ANM, $Q_{\text{pu}} = 40$.

Figure 6.17: Comparison of PU-probe orientations via RMSE versus SNR using ESPRIT and Root-MUSIC methods for both IMSS and ANM approaches for $K = 33$, $\epsilon = 1$.

For the PU-probe configuration, the RMSE performance exhibits a different behavior compared to the individual pressure-only or U-probe cases.

For the IMSS approach, it can be seen from Figure 6.17 that the random configuration with $Q_{\text{pu}} = 40$ yields the lowest RMSE across the entire SNR range, followed closely by the tangential configuration with $Q_{\text{pu}} = 40$. The radial configuration results in the highest RMSE for both Root-MUSIC and ESPRIT; however, the differences between all configurations are remarkably small. At the lowest SNR of -4 dB, the gap between the highest and lowest RMSE is approximately $0.25°$, and this difference further decreases with increasing SNR, reaching about $0.03°$ at 14 dB.

This behavior indicates that the PU-probe configuration with IMSS achieves significantly lower estimation errors compared to configurations using only pressure or only particle velocity measurements. The main reason is that the number of channels is effectively doubled, leading to a much taller matrix $\mathbf{G}^{(\text{pu})}_{Q_{\text{pu}}}$ compared to $\mathbf{G}^{(\text{p})}_{t,Q_{\text{p}}}$ $t \in \{a, b\}$ and $\mathbf{G}^{(\text{u})}_{Q_{\text{u}}}$. As a result, the matrix inversion involved in IMSS becomes better conditioned, which improves estimation accuracy across all configurations.

For the ANM approach, the performance trends differ slightly. Up to approximately 3 dB, Root-MUSIC with tangential orientation provides the lowest RMSE, followed by Root-MUSIC with random orientation. Beyond 3 dB, ESPRIT and Root-MUSIC with tangential orientation become closely aligned and jointly yield the lowest RMSE. The radial configuration consistently produces the highest RMSE across all SNR values.

Interestingly, for all configurations in the PU-probe case, IMSS achieves lower RMSE than ANM, which is the opposite of the trend observed in the previous configurations. Given that IMSS is also computationally less demanding than ANM, this result highlights a favorable trade-off that improved estimation accuracy at the expense of increased number of channels.

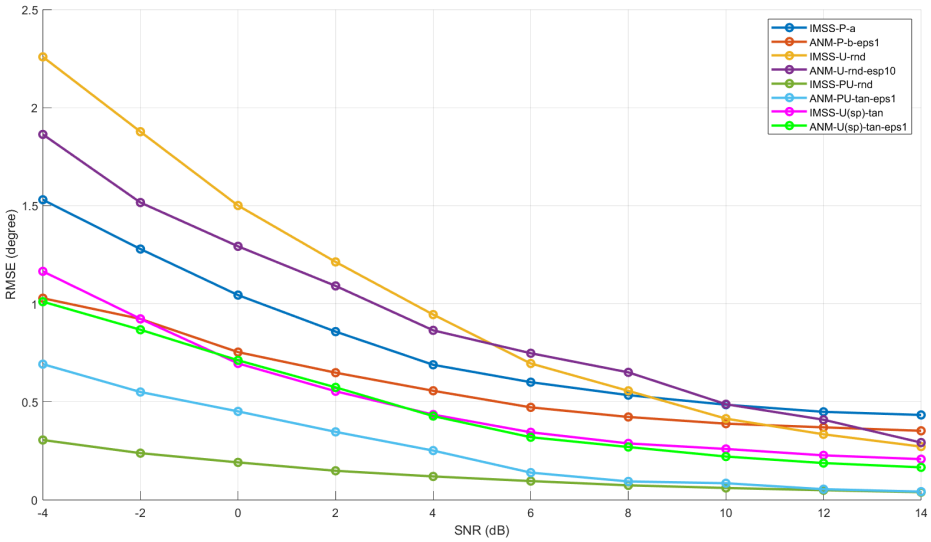


Figure 6.18: RMSE versus SNR comparison using Root-MUSIC for both IMSS and ANM approaches for pressure-only (P), U-probe (U), special U-probe (U(sp)), and PU-probe (PU) configurations with $K = 33$, $Q = 40$.

Figure 6.18 summarizes the best-performing configurations across pressure-only (P), U-probe-only (U), special U-probe (U(sp)), and PU-probe (PU) setups for both IMSS and ANM. As expected, the PU-probe configuration achieves the lowest RMSE over the entire SNR range, with IMSS slightly outperforming ANM, particularly in the low SNR regime. Beyond approximately 6 dB, both methods exhibit nearly identical performance, indicating that IMSS is more robust to noise, mainly due to the significantly larger size of $\mathbf{G}_{Q_{\text{pu}}}^{(\text{pu})}$.

Among the remaining configurations, the special U-probe case with a central pressure sensor performs better. In particular, this special setup with ANM yields the third lowest RMSE, followed by U(sp) with IMSS, specifically after -2 dB. In contrast, all U-probe-only configurations exhibit the highest errors up to about 8 dB, confirming that particle velocity measurements alone is less reliable in noisy conditions.

However, as the SNR increases, the benefit of particle velocity measurements becomes evident. Beyond 10 dB, U-probe configurations using both IMSS and ANM with random orientation begin to outperform pressure-only cases, and by approximately 14 dB, they consistently achieve lower RMSE than pressure non-redundant co-array with ANM. This highlights their advantage in high SNR regimes.

Despite its superior performance, the PU-probe configuration comes with increased hardware and storage requirements, as it doubles the number of channels from M to $2M$. Moreover, each particle velocity measurement is inherently correlated with its corresponding pressure data, which raises questions about redundancy and efficiency. This motivates the usage of a more efficient hybrid setup like U(sp), where M particle velocity sensors are arranged in a UCA with a single pressure sensor at the center. This setup aims to balance performance and system complexity by leveraging the benefits of particle velocity measurements while minimizing redundancy and channel count.

6.4 Conclusion

In this chapter, the proposed co-array-based framework for DoA estimation on a UCA was evaluated under both overdetermined and underdetermined scenarios applying IMSS and ANM on the constructed virtual ULA. The results demonstrated that the proposed framework enables the effective application of gridless subspace methods such as ESPRIT and Root-MUSIC, while extending the virtual aperture beyond the limitations of the physical array.

In the overdetermined regime, the comparison with classical MUSIC confirmed the consistency of the proposed framework with conventional covariance-based processing. Although approximation errors were observed for co-array-based approaches in pressure-only and U-probe configurations, ANM generally provided more accurate covariance representations than IMSS. The MUSIC spectrum analysis further showed that the ANM-based covariance-like matrix achieves sharper spectral peaks due to its larger virtual aperture.

For underdetermined scenarios, both single-realization and Monte Carlo simulations demonstrated the capability of the proposed methods to resolve a large number of sources using a limited number of physical sensors. Overall, ANM consistently outperformed IMSS in the pressure-only and U-probe configurations, while Root-MUSIC generally achieved lower RMSE than ESPRIT. The influence of co-array redundancy, sensor orientation, truncation parameter selection, and regularization was also investigated, highlighting the trade-offs between estimation accuracy under different noise conditions.

Among all considered configurations, the PU-probe setup achieved the best overall performance due to the increased number of measurement channels and the resulting improvement in virtual array conditioning. In this case, IMSS slightly outperformed ANM while also maintaining lower computational complexity. Furthermore, the special U-probe configuration with a central pressure sensor was shown to provide an attractive compromise between performance and system complexity, achieving substantial improvements over pressure-only and U-probe-only setups with only a marginal increase in channel count.

Overall, the presented results validate the effectiveness of the proposed virtual co-array framework for high-resolution gridless DoA estimation and demonstrate its flexibility across different sensing configurations and operating conditions.

7 Conclusion

This thesis investigated the problem of DoA estimation in underdetermined scenarios using a UCA composed of AVSs. The primary objective was to overcome the inherent limitation of conventional array processing techniques, where the number of resolvable sources is bounded by the number of physical sensors.

The main contribution of this work lies in combining the co-array concept with UCA-based AVS measurements to enable underdetermined DoA estimation. By exploiting second-order statistics, an augmented co-array structure was constructed, effectively increasing the degrees of freedom beyond the number of physical array elements. This co-array was shown to exhibit a concentric multi-circular structure, whose individual virtual elements could be interpreted according to the underlying sensor component correlations from which they originated. Specifically, pressure–pressure correlations were associated with scalar co-array contributions, whereas particle velocity–particle velocity correlations introduced direction-dependent vectorial weighting determined by the sensor orientation. In the PU-probe configuration, mixed pressure–particle velocity correlations were additionally interpreted as virtual elements carrying directional particle velocity information. The obtained co-array was then transformed into a virtual ULA using the Jacobi–Anger expansion. This transformation enabled the use of high-resolution gridless subspace-based methods such as ESPRIT and Root-MUSIC.

A key challenge addressed in this framework is the single-snapshot limitation arising from correlation-domain processing of stationary signals. To overcome this, two approaches were employed, namely IMSS and ANM. These methods enabled reliable subspace estimation despite the lack of multiple snapshots.

The framework was initially developed for a pressure-only UCA and subsequently extended to incorporate particle velocity measurements through U-probe and PU-probe configurations. This progressive development allowed a systematic evaluation of how additional sensing modalities influence the achievable performance and degrees of freedom.

Simulation results demonstrated that the proposed approach successfully enables DoA estimation in highly underdetermined scenarios, where the number of sources significantly exceeds the number of sensors. In the pressure-only case, ANM consistently outperformed IMSS, particularly in challenging conditions, by better exploiting the co-array structure. For U-probe configurations, sensor orientation was shown to play a crucial role, with random orientations generally yielding the best performance. The inclusion of both pressure and particle velocity measurements in the PU-probe configuration resulted in a substantial improvement in estimation accuracy, achieving the lowest RMSE across all tested scenarios.

Furthermore, the results highlighted important trade-offs between performance and system complexity. While the PU-probe configuration provides the highest accuracy due to increased channel count, it also incurs higher hardware and computational costs.

In contrast, intermediate configurations, such as hybrid setups, offer a balance between performance gains and implementation efficiency.

Overall, the results confirm that the integration of co-array processing with AVS-based UCA measurements provides a powerful and flexible framework for high-resolution DoA estimation in underdetermined settings.

7.1 Future Work

Several directions can be pursued to further extend the framework developed in this thesis. A natural extension is the analysis of the directivity terms of the virtual sensors occurring in concentric multi-circular arrays. In particular, the directivity as well as the sensitivity diagrams can be explored in greater detail, which may provide additional insight into the characteristics of the virtual array structure of U-probes.

Another natural extension is the generalization to full two-dimensional DoA estimation, where both azimuth and elevation angles are considered. This would require adapting the current formulation, which assumes sources confined to the horizontal plane, to a fully 3D propagation model. In this context, the co-array construction and the subsequent transformation to a virtual array would need to be revisited, potentially leading to more complex array manifolds and processing strategies.

Another important direction is the extension to wideband signal scenarios. The current framework assumes narrowband sources, which simplifies the array response model. For wideband signals, frequency-dependent effects must be taken into account. This could be addressed through techniques such as subband decomposition or coherent/incoherent wideband processing, enabling the proposed methods to operate in more realistic acoustic environments.

Finally, the use of spherical array geometries represents a promising avenue for future research. In particular, spherical microphone or AVS arrays combined with spherical harmonic representations could provide a more natural framework for 3D DoA estimation. Incorporating spherical harmonics into the co-array and gridless estimation framework may enable more efficient handling of elevation information and improved spatial representation.

Overall, these extensions would broaden the applicability of the proposed framework and further enhance its capability in practical and complex acoustic scenarios.

Bibliography

[1] H. L. Van Trees. *Optimum Array Processing*. Wiley, 2002.

[2] Y. Wang et al. "Progress in Beamforming Acoustic Imaging Based on Phased Microphone Arrays: Algorithms and Applications". In: *Measurement* 242 (2025).

[3] R. Corey, D. Skarha, and A. Singer. "Cooperative Audio Source Separation and Enhancement Using Distributed Microphone Arrays and Wearable Devices". In: Dec. 2019, pp. 296–300.

[4] S. Chevtchenko et al. "Drone-Based Sound Source Localization: A Systematic Literature Review". In: *IEEE Access* (2025).

[5] Y. Bai et al. "Acoustic-Based Sensing and Applications: A Survey". In: *Computer Networks* 181 (2020).

[6] K. T. Wong and M. D. Zoltowski. "Extended-Aperture Underwater Acoustic Multisource Azimuth/Elevation Direction Finding Using Uniformly but Sparsely Spaced Vector Hydrophones". In: *IEEE Journal of Oceanic Engineering* 22.4 (1997), pp. 659–672.

[7] B. Hochwald and A. Nehorai. "Identifiability in array processing models with vector-sensor applications". In: *IEEE Transactions on Signal Processing* 44.1 (1996), pp. 83–95.

[8] P. Ioannides and C.A. Balanis. "Uniform circular and rectangular arrays for adaptive beamforming applications". In: *IEEE Antennas and Wireless Propagation Letters* 4 (2005), pp. 351–354.

[9] G. Sun et al. "Beam pattern design of circular antenna array via efficient biogeography-based optimization". In: *International Journal of Electronics and Communications (AEU)* 79 (2017), pp. 275–285.

[10] U. Baysal and R.L. Moses. "On the geometry of isotropic arrays". In: *IEEE Transactions on Signal Processing* 51.6 (2003), pp. 1469–1478.

[11] B. Friedlander and A.J. Weiss. "Direction finding using spatial smoothing with interpolated arrays". In: *IEEE Transactions on Aerospace and Electronic Systems* 28.2 (1992), pp. 574–587.

[12] C. P. Mathews and M. D. Zoltowski. "Eigenstructure techniques for 2-D angle estimation with uniform circular arrays". In: *IEEE Transactions on Signal Processing* 42.9 (1994), pp. 2395–2407.

[13] P. Hyberg, M. Jansson, and B. Ottersten. "Array interpolation and bias reduction". In: *IEEE Transactions on Signal Processing* 52.10 (2004), pp. 2711–2720.

[14] P. Hyberg, M. Jansson, and B. Ottersten. "Array interpolation and DOA MSE reduction". In: *IEEE Transactions on Signal Processing* 53.12 (2005), pp. 4464–4471.

[15] F. Belloni and V. Koivunen. "Beamspace Transform for UCA: Error Analysis and Bias Reduction". In: *IEEE Transactions on Signal Processing* 54.8 (2006), pp. 3078–3089.

[16] F. Belloni, A. Richter, and V. Koivunen. "DoA Estimation Via Manifold Separation for Arbitrary Array Structures". In: *IEEE Transactions on Signal Processing* 55.10 (2007), pp. 4800–4810.

[17] R. Goossens, H. Rogier, and S. Werbrouck. “UCA Root-MUSIC with Sparse Uniform Circular Arrays”. In: *IEEE Transactions on Signal Processing* 56.8 (2008), pp. 4095–4099.

[18] D. Zhao et al. “Low Complexity Sparse Beamspace DOA Estimation via Single Measurement Vectors for Uniform Circular Array”. In: *EURASIP Journal on Advances in Signal Processing* (2021).

[19] P. Pal and P. P. Vaidyanathan. “Nested Arrays: A Novel Approach to Array Processing with Enhanced Degrees of Freedom”. In: *IEEE Trans. Signal Process.* 58.8 (2010), pp. 4167–4181.

[20] P. Pal and P. P. Vaidyanathan. “Coprime Sampling and the MUSIC Algorithm”. In: *2011 Digital Signal Processing and Signal Processing Education Meeting (DSP/SPE)*. Sedona, AZ, USA, 2011, pp. 289–294.

[21] D. Liu and P. P. Vaidyanathan. “Coprime Arrays and Their Applications in Direction-of-Arrival Estimation”. In: *IEEE Signal Processing Magazine* (2016).

[22] Z. Zheng et al. “Augmented Covariance Matrix Reconstruction for DOA Estimation Using Difference Coarray”. In: *IEEE Transactions on Signal Processing* 69 (2021), pp. 5345–5358.

[23] W.-K. Ma, T.-H. Hsieh, and C.-Y. Chi. “DOA Estimation of Quasi-Stationary Signals with Less Sensors than Sources and Unknown Spatial Noise Covariance: A Khatri–Rao Subspace Approach”. In: *IEEE Transactions on Signal Processing* 58.4 (2010), pp. 2168–2180.

[24] C. Zhou et al. “Direction-of-Arrival Estimation for Coprime Array via Virtual Array Interpolation”. In: *IEEE Transactions on Signal Processing* 66.22 (Nov. 2018), pp. 5956–5971.

[25] C.-L. Liu and P. P. Vaidyanathan. “Remarks on the Spatial Smoothing Step in Coarray MUSIC”. In: *IEEE Signal Processing Letters* 22.9 (2015), pp. 1438–1442.

[26] G. Wang et al. “Improved 2D Coprime Array Structure with the Difference and Sum Coarray Concept”. In: *Electronics* 9.2 (2020).

[27] M. J. Ren et al. “Generalized and Symmetric Coprime Planar Array for Direction-of-Arrival Estimation”. In: *IET Radar, Sonar & Navigation* (2022).

[28] Q. Wu et al. “Two-Dimensional Direction-of-Arrival Estimation for Co-Prime Planar Arrays: A Partial Spectral Search Approach”. In: *IEEE Sensors Journal* 16.14 (2016), pp. 5660–5670.

[29] S. K. Yadav and N. V. George. “Underdetermined Direction-of-Arrival Estimation Using Sparse Circular Arrays on a Rotating Platform”. In: *IEEE Signal Processing Letters* 28 (2021), pp. 862–866.

[30] H. Wu et al. “2-D Wideband DOA Estimation with Circular Arrays Based on the Difference Co-Array Concept”. In: *IEEE International Symposium on Circuits and Systems (ISCAS)*. 2024.

[31] M.-Y. Cao et al. “Underdetermined DOA Estimation of Quasi-Stationary Signals via Khatri–Rao Structure for Uniform Circular Array”. In: *Signal Processing* 106 (2015), pp. 41–48.

[32] Z. Xie et al. “Concentric Circular Nested Array Design Method for Acoustic Imaging Based on Differential Coarray Model”. In: *IEEE Sensors Journal* 25.10 (May 2025), pp. 18106–18114.

[33] S. K. Yadav and N. V. George. "Underdetermined DOA Estimation Using Arbitrary Planar Arrays via Coarray Manifold Separation". In: *IEEE Transactions on Vehicular Technology* 71.11 (2022), pp. 11959–11971.
[34] J. P. Kitchens. "Acoustic Vector-Sensor Array Processing". PhD thesis. Cambridge, MA: Massachusetts Institute of Technology, 2010.
[35] H.-E. de Bree. "An Overview of Microflown Technologies". In: *Acta Acustica united with Acustica* 89.1 (2003), pp. 163–172.
[36] H.-E. de Bree. *The Microflown E-book*. Available online. 2009. URL: https://www.microflown.com (visited on 03/15/2026).
[37] Microflown Technologies. *U-Regular: 1D Acoustic Particle Velocity Sensor*. Available online. 2026. URL: https://www.microflown.com/products/acoustic-particle-velocity-sensors/u-regular (visited on 03/15/2026).
[38] F. Jacobsen and P. M. Juhl. *Fundamentals of General Linear Acoustics*. John Wiley & Sons, 2013.
[39] Microflown Technologies. *PU-Regular: Sound Intensity Probe*. Available online. 2026. URL: https://www.microflown.com/products/standard-probes/pu-regular (visited on 03/15/2026).
[40] A. Nehorai and E. Paldi. "Acoustic Vector-Sensor Array Processing". In: *IEEE Transactions on Signal Processing* 42.9 (1994), pp. 2481–2491.
[41] K. N. Ramamohan, D. Fernandez Comesaña, and G. Leus. "Uniaxial Acoustic Vector Sensors for Direction-of-Arrival Estimation". In: *Journal of Sound and Vibration* 437 (2018), pp. 276–291.
[42] R. Roy and T. Kailath. "ESPRIT—Estimation of Signal Parameters via Rotational Invariance Techniques". In: *IEEE Trans. ASSP* (1989).
[43] B. D. Rao and K. V. S. Hari. "Performance analysis of Root-Music". In: *IEEE Transactions on Acoustics, Speech, and Signal Processing* 37.12 (1989), pp. 1939–1949.